Statistical Laws of

Protein Motion in Neuronal Dendritic Trees

Dissertation

zur Erlangung des Doktorgrades

der Naturwissenschaften

vorgelegt beim Fachbereich Physik

der Johann Wolfgang Goethe-Universität

in Frankfurt am Main

von

Fabio Sartori

aus Parma (Italy)

Frankfurt am Main, June 2021

vom Fachbereich Physik der

Johann Wolfgang Goethe-Universität Frankfurt

als Dissertation angenommen.

Dekan: Prof. Dr. Harald Appelshäuser

Gutachter: Dr. Tatjana Tchumatchenko

              Prof. Dr. Jochen Triesch

Datum der Disputation: 20.09.2021

Deutsche Zusammenfassung

Das Ziel dieser Arbeit ist es, die Verteilung von Proteinen und anderen dendritischen Bestandteilen im Dendritenbaum zu verstehen. Zunächst werde ich einen Überblick über den Aufbau der Arbeit bieten und dann die wichtigsten Ergebnisse schildern. Erstens beschreibe ich verschiedene Transportmechanismen und ermittle für jeden von ihnen die Proteindichte, siehe Abschnitt 2. Zweitens, in dem dritten Abschnitt, werde ich die Lösungen der in Abschnitt 2 abgeleitete Diffusionsgleichung verwenden, um die minimale Anzahl von Proteinen abzuleiten, die das Neuron produzieren muss, um mindestens ein Protein in jedem Mikrometer des Dendriten bereitzustellen. Diese Proteinmenge wurde als "Proteinbedarf" bezeichnet.

In Abschnitt 3, habe ich gezeigt, dass der "Proteinbedarf" für einen Dendritenbaum mit einem einzelnen Ast ein Minimum erreicht für einen bestimmten Wert von R_1/R_2. Der R_1 Wert, der den Proteinbedarf minimiert, wurde als "optimaler Radius" definiert. In Abschnitt 4, habe ich eine explizite Relation gefunden, um die optimalen Radien zu finden. In Abschnitt 5, habe ich die Morphologie von drei Klassen von Dendriten analysiert: kultivierte hippocampale Neuronen, pyramidale Neuronen aus dem präfrontalen Cortex und stomatogastrische Neuronen des Krebses. Für jede Dendritenart habe ich die Radienstatistiken in der Umgebung der dendritischen Verzweigungen untersucht. Dann habe ich die Informationen über die Radien benutzt, um den Anteil der Proteine zu quantifizieren, die sich vom Soma wegbewegen. Ich habe dies mit einem Parameter quantifiziert, den ich "Wahrscheinlichkeitsverhältnis" benannt habe. In Abschnitt 6, habe ich die Vorhersage des Wahrscheinlichkeitsverhältnisses von kultivierten Neuronen mit dem Fluoreszenzverhältnis verglichen, das durch die Analyse des Fluoreszenzsignals von zwei Arten von Proteinen erhalten wurde: GFP und GFP::Nlg. GFP, grün fluoreszierendes Protein, ist ein lösliches Protein, das im Zytoplasma diffundiert. GFP::Nlg, Neuroligin, assoziiert mit GFP, ist ein membran-assoziiertes Protein, das auf der Zellenoberfläche diffundiert.

In Abschnitt 7, habe ich die Informationen über die Radien und die Länge des Dendriten eines pyramidalen Neurons benutzt, um die in Abschnitt 4 erhaltene Optimalitätsregel auf reale

Morphologien anzuwenden. Ich benutzte diese Relation, um die Verteilung der Diffusionslänge zu erhalten, für die die Verzweigungen optimiert sind, und ich verglich diese Verteilung mit der von existierenden Proteinen. In Abschnitt 8, habe ich die in Abschnitt 2 erhaltene Verzweigungsregel sowie die Optimalitätsregel aus Abschnitt 4 angewendet, um die Verteilung der Proteine im Gleichgewicht für drei Neuronenklassen zu berechnen. Die Simulationen wurden unter Annahme der in Abschnitt 7 diskutierten Diffusionskoeffizienten und Halbwertszeiten durchgeführt.

In Abschnitt 2, habe ich mehrere dendritische Transportmodelle untersucht und für jedes eine analytische Lösung und die Verteilung der Proteine im Gleichgewicht angegeben. Das einfachste dieser Modelle beinhaltet rein diffuser Transport, bei dem alle Proteine im Soma synthetisiert werden, siehe Kap 2.1. Anschließend habe ich aktiver Transport miteingeführt; ein von Nervenzellen benutztes Mechanismus, um schnell Proteine und andere dendritische Komponenten im Dendritenbaum zu transportieren. Dies erfolgt, indem das Neuron molekulare Motore einsetzt, Enzyme, die chemische Energie in mechanische Arbeit umwandeln, um die molekularen Ladungen entlang der Mikrotubuli zu ziehen. Unter Verwendung der Arbeit von Bressloff [1] habe ich aktiver Molekültransport entweder als einen erhöhten Diffusionskoeffizienten modelliert oder als einen zusätzlichen Term in der Diffusionsgleichung: $v\frac{\partial \rho}{\partial x}$.

Danach habe ich das Verhalten eines Proteins an einer dendritischen Verzweigung modelliert: Ich stellte die Hypothese auf, dass die Wahrscheinlichkeit, sich in eine der beiden Richtungen zu bewegen, vom verfügbaren Raum in dieser Richtung abhängt, entsprechend:

$$f_i = \frac{R_i^{\gamma}}{R_0^{\gamma} + R_1^{\gamma} + R_2^{\gamma}}, \tag{1}$$

wobei γ die Anzahl der Dimensionen darstellt, die das Protein bei seiner Diffusion minus eins erkundet; $\gamma = 1$ für die Proteindiffusion auf der Oberfläche des Neurons, $\gamma = 2$ für die Proteindiffusion im Zytoplasma des Neurons; R_0 ist der Radius des Mutterdendriten, und R_1, R_2 sind die Radien der beiden Tochterdendriten.

In Abschnitt 3, habe ich die Proteinanforderung als die minimale Anzahl von Proteinen

definiert, die das Neuron in den Dendriten einbringen muss, damit sich mindestens ein Protein pro Mikrometer des Dendriten befindet. Ich habe gezeigt, dass Proteinbedarf minimiert wird, wenn ein Protein nur diffundieren kann und mit einer konstanten Rate in den Dendritenbaum übersetzt wird. Ein anderes Modell mit einem geringen Proteinbedarf entsteht, wenn die mRNAs aktiv in Dendriten transportiert werden und das Protein nur diffundiert. Der Vorteil eines geringeren Proteinbedarfs ist jedoch damit verbunden, dass auch die mRNAs im dendritischen Baum transportiert werden.

Für einen festen Wert der Länge der Tochterdendriten werden L_1 und L_2 sowie der Proteinbedarf durch ein bestimmtes Verhältnis der Tochterradien minimiert, entsprechend mit

$$\frac{\cosh{(L_1/\lambda)}}{\cosh{(L_2/\lambda)}} = \frac{R_1^{\gamma}}{R_2^{\gamma}}, \tag{2}$$

wobei λ die Diffusionslänge des Proteins ist, wie in Abschnitt 4 diskutiert und analysiert.

Wenn die Radien der Mutter- und der Tochterdrite bekannt sind, kann man mit Hilfe von Gleichung 1 den Anteil der Proteine berechnen, die sich in jede Richtung bewegen. Wenn die Gesamtoberfläche nach dem Verzweigungspunkt größer ist als die Gesamtoberfläche vor dem Verzweigungspunkt, diffundiert mehr Oberflächenprotein in die Tochterdriten. Ähnlich passiert es, wenn das Gesamtvolumen nach dem Verzweigungspunkt höher ist als das Gesamtvolumen vor dem Verzweigungspunkt, denn dann diffundieren lösliche Proteine eher vom Soma weg. Ich habe diese Eigenschaft mit einem Parameter quantifiziert, den ich als "Wahrscheinlichkeitsverhältnis" benannt und folgendermaßen definiert habe:

$$Q_P^{\gamma} = \frac{R_1^{\gamma} + R_2^{\gamma}}{R_0^{\gamma}}. \tag{3}$$

Da die Tochterradien für den Proteinbedarf in verzweigten Dendriten sehr wichtig sind, habe ich in Abschnitt 5 drei Datensätze von Neuronen analysiert, um ihre Radienstatistiken zu untersuchen und zu verstehen, wie sich das Protein durchschnittlich an ihren Verzweigungen ver-

haltet. Der erste Datensatz, den ich betrachtete, bestand aus 67 Verzweigungen in kultivierten Hippocampus-Neuronen. Bilder dieser Neuronen wurden von einer unserer Mitarbeiter, Anne-Sophie Hafner, erfasst. Der zweite Datensatz enthielt 68 Verzweigungen von pyramidalen Neuronen aus dem präfrontalen Kortex; Bilder dieser Neuronen wurden von unserem Kooperationspartner Ali Karimi erfasst. Der dritte Datensatz ist ein publizierter Datensatz, der 252 Verzweigungen von Neuronen aus den stomatogastrischen Ganglien des Krebses enthält, [2].

In Abschnitt 6, habe ich das Fluoreszenzsignal von zwei fluoreszierenden Proteinen analysiert: GFP und GFP::Nlg vor und nach dem Verzweigungspunkt im Dendrit. GFP, grün fluoreszierendes Protein, ist ein lösliches Protein, das im Zytoplasma diffundiert. GFP::Nlg, Neuroligin, assoziiert mit GFP, ist ein membran-assoziiertes Protein, das auf der Zellenoberfläche diffundiert.

Die Fluoreszenz der Proteine in der transfizierten kultivierten Nervenzelle wurde in einem kleinen Intervall um eine Verzweigung herum gemessen und integriert, wodurch ich das Verhältnis der Fluoreszenz nach und vor der Verzweigung berechnen konnte:

$$Q_F = \frac{F_1 + F_2}{F_0}. \tag{4}$$

Dann habe ich das Wahrscheinlichkeitsverhältnis von kultivierten Neuronen verglichen: 1.45 (IQR: 1.27 − 1.65) und 1.12 (IQR: 0.87 − 1.37) für Oberflächen- bzw. zytoplasmatisches Protein, mit dem Fluoreszenzverhältnis von kultivierten Neuronen: 1.32 (IQR: 1.08 − 1.71) und 1.16 (IQR: 0, 88 − 1.41) für Oberflächen- bzw. zytoplasmatisches Protein.

In Abschnitt 7, habe ich die Diffusionslänge von 26 existierenden Proteinen mit den Diffusionslängen verglichen, die ich durch der Umkehrung von Gleichung 2 erhalten habe. Diese Diffusionslängen stellen die Diffusionslänge dar, für die der Verzweigungspunkt optimiert ist. In Abb. 23 habe ich gezeigt, dass die Verteilung der Diffusionslänge dieser existierenden Proteine einen höheren Median hat als die optimierten Diffusionslängen besitzen. In Abb. 23-E ist zu sehen, dass Proteine mit einer größeren Diffusionslänge als optimal, geringere Kosten in Form von zusätzlich benötigten Proteinen verursachen als Proteine mit einer kleineren Diffusionslänge.

In Abschnitt 8, habe ich die Diffusion von Oberflächen- und Zytoplasmaproteinen in drei Arten von dendritischen Morphologien simuliert: Pyramidal-, Purkinje- und Granularzellen. Die Morphologien wurden der Online-Datenbank "Neuromorpho" entnommen, [3]. Für jede Zellenart habe ich zwei verschiedene Diffusionslängenwerte erhalten: $\lambda = 109\mu m$ und $\lambda = 473\mu m$. Der erste ist der Median der Diffusionslänge, die aus Gl. 2 für Oberflächenproteine erhalten wurde, und der zweite ist die Diffusionslänge einer Untereinheit der GABA-Rezeptoren. Für jede Morphologie habe ich auch zwei Extremalregeln für die Radien in Betracht gezogen: als Null-Hypothese habe ich angenommen, dass jeder Zweig symmetrisch ist und die Radien der beiden Tochterdendriten sind: $R_1 = R_2 = 0,74R_0$. Zuletzt verglich ich den Proteinbedarf für diese symmetrischen Zweige mit dem, den ich erhielt, indem ich annahm, dass jeder Zweig den optimalen Radius besitzt. Um die optimalen Radien im gesamten dendritischen Ast zu erhalten, habe ich die Verallgemeinerung von Gl. 2 verwendet, die in Abschnitt 4.2 beschrieben wird.

Schließlich habe ich den aus den verschiedenen Modellen erhaltenen Proteinbedarf mit einer Schätzung der Gesamtzahl der Proteine in den Dendriten verglichen: $N = 6\,10^9$. Dies zeigt, dass bei der Optimierung von Radien der aktiver Transport ein zuverlässiges Mechanismus ist, um Proteine in distale Dendriten zu transportieren.

	pyramidales 95%	Anteil an der Gesamtmenge dendritischer Proteine
$\lambda = 108$ Zytoplasma, Symm	$2.9\,10^{10}$	480%
$\lambda = 473$ Zytoplasma, Symm	$1.2\,10^{9}$	20%
$\lambda = 108$ Oberfläche, Symm	$4.8\,10^{8}$	8%
$\lambda = 473$ Oberfläche, Symm	$3.6\,10^{6}$	0.06%
$\lambda = 108$ Zytoplasma, Opt	$1.7\,10^{6}$	0.03%
$\lambda = 473$ Zytoplasma, Opt	$6.2\,10^{4}$	0.001%
$\lambda = 108$ Oberfläche, Opt	$1.2\,10^{6}$	0.02%
$\lambda = 473$ Oberfläche, Opt	$3.4\,10^{4}$	0.006%

Table 1: **Übersicht des Proteinbedarfs,** Proteinbedarf zur Versorgung von 95% der pyramidalen dendritischen Bäume und Anteil an der Gesamtmenge dendritischer Proteine.

Acknowledgements

I want to express my gratitude to my supervisor, Tatjana, who supported me for all these years, providing us a dynamical environment where to explore and chase our ideas and intuitions. I am very grateful for the freedom she gave me in allowing me to change my starting subject to pursue one that was better fitted for me.

I want to thank all the members of my TAC, Erin Schuman, Jochen Triesch, and Hermann Cuntz, who helped me in many steps of this incredible Journey; Hermann for being a fantastic PI, during my short rotation in his lab, Jochen for his support and insight, and Erin for her knowledge and advice, and patience, in a field that was new to me before: biology.

I want to express my warmest thanks to Andreas for helping me grow both on the scientific level due to his knowledge and expertise on the topic of this dissertation and on a personal level. The other (not anymore) postdoc without which this project wouldn't have gone anywhere and probably not even started is Anne-Sophie. Probably the most patient and methodical of all the people who helped me.

Then I would like to mention all the people that manage to make these years enjoyable. Laura, who shared with me an unforgettable trip to Frankfurt, and Pierre, with whom I shared many dinners and nights playing board games. In this weird last year, where meeting in person was not advisable, the presence in real, virtual life of so many friends every Thursday has been the best way to keep track of the time without letting it blurring away. Thank you Theo, Alex, Lisandro, Ben, Niklas, Sigrid.

And thanks to those friends who I only met in Covid-times, Miho and Michelle. And to all the other amazing people who supported and who put up with me. Furthermore, I would like to thank Leo, who was so kind to translate for me the "Deutsche Zusammenfassung" section.

Ed infine un grazie di cuore ai miei genitori. Senza il loro supporto in questi anni, ed i mille sacrifici, non sarei mai riuscito a fare nessuno dei passi che mi hanno portato qui.

Finally, to steal a phrase from a book: "So long, and thanks for all the fish."

List of Publications

The work I have done during this Ph.D. resulted in the following publications:

- [4] Agliari E, Cassi D, Cattivelli L, **Sartori F**. Physical Review E. 2016 May 5; 93(5): 052111.

- [5] Weigand M, **Sartori F**, Cuntz H. Universal transition from unstructured to structured neural maps. Proceedings of the National Academy of Sciences. 2017 May 16; 114(20): E4057-64.

- [6] Fonkeu Y, Kraynyukova N, Hafner AS, Kochen L, **Sartori F**, Schuman EM, Tchumatchenko T. How mRNA localization and protein synthesis sites influence dendritic protein distribution and dynamics. Neuron. 2019 Sep 25; 103(6): 1109-22.

- [7] **Sartori F**, Hafner AS, Karimi A, Nold A, Fonkeu Y, Schuman EM, Tchumatchenko T. Statistical Laws of Protein Motion in Neuronal Dendritic Trees. Cell reports. 2020 Nov 17; 33(7): 108391.

Abstract

Neurons are cells with a highly complex morphology; their dendritic arbor spans up to thousands of micrometers. This extended arbor poses a challenge for the logistics of neuronal processes: mRNA, proteins, and organelles have to be transported to dendrites, hundreds of micrometers away from the soma. This thesis aims to calculate the minimum number of proteins needed to populate the dendritic trees for different scenarios.

In chapter 2, I analyzed the ability of different mechanisms to populate the dendritic arbor. I started from the solution of the diffusion equation in Sec. 2.1, then I included the contribution of active transport in Sec. 2.2 and showed how it could have either the effect of increasing the effective diffusion coefficient or of introducing a bias in the diffusion process. In Sec. 2.3 I studied the spatial distribution of locally synthesized protein, accordingly with actively and passively transported mRNA. In Sec. 2.5, I derived the boundary condition for branches showing a qualitatively different behavior of surface and cytoplasmic proteins induced by the medium's dimensionality in which they diffuse.

In chapter 3, I introduced the concept of *protein requirement*, defined as the minimum number of proteins that the neuron needs to produce to provide at least one protein to each micrometer of the dendritic arbor. In Sec. 3.1, I derived the protein requirement for diffusive proteins for somatic translation and constant translation in the dendritic arbor. In Sec. 3.2, I analyzed numerically the protein requirement in the case of actively transported protein synthesized in the soma, and, in Sec. 3.3, in the case of actively transported proteins synthesized in the dendritic arbor. In Sec. 3.4, I analyzed the protein requirement of protein synthesized in the dendrite accordingly with the distribution of mRNA described in Sec. 3.3 and 3.2. In Sec. 3.5, I derived the protein requirement for a single branch and purely diffusive proteins.

In chapter 4, I analyzed the relation between the radii of the three afferent dendrites in a branch, their length, and the diffusion length of a protein. In Sec. 4.1 I derived the optimal ratio between the radii of the daughter dendrites that minimizes the protein requirement. In Sec. 4.3

I introduced the $3/2-$ Rall Rule and in Sec. 4.5 its generalization. Finally, I used those rules to estimate the fraction of proteins diffusing away from and toward the soma.

In chapter 5, I analyzed the radii distribution for three categories of neurons: cultured hippocampal neurons in Sec. 5.1, stomatogastric ganglia neuron in Sec. 5.2, and 3DEM reconstructed prefrontal pyramidal neurons in Sec. 5.3. For each of these three classes, I analyzed the distribution of radii, Rall exponents, and the probability ratio. For most of them, I found that the probability of a protein diffusing away from the soma is higher for surface proteins than for cytoplasmic ones. I quantified this with a parameter called *surface bias*.

In Chapter 6, I analyzed the fluorescent ratio imaged by our collaborators Anne-Sophie Hafner, for a surface protein, GFP::Nlg, and a soluble one, GFP, in cultured hippocampal neurons, and I compared the fluorescent ratio with the probability ratio obtained in 5.1, finding that they are in good agreement.

In chapter 7, I compared the real dendritic morphologies imaged by one of our collaborators Ali Karimi with the optimal branching rule obtained in Sec. 4.1 and I calculated the cost for not having optimal branching radii.

Finally, in Chapter 8, I used the knowledge of the branching statistics gathered in 5.3 to simulate the protein profile on three different classes of neurons: pyramidal neurons, granule neuron, and Purkinje neurons. I compared the protein profile for surface and cytoplasmic neurons for each morphology for two different values of the diffusion length: $\lambda = 109\mu m$ and $\lambda = 473\mu m$, both for optimized radii and symmetrical radii. I showed how the radii optimization reduces the protein requirement of a factor 10^4 for pyramidal neurons.

Contents

1   Introduction

Neurons are electrical cells that communicate with each other through a complex network of axons and dendrites. Axons and dendrite are complex, branched structures that stretch up to several centimeters the first and hundreds of micrometers the second. Like all other cells, neurons require a steady stream of protein, mRNA, and organelles to maintain their function. The extreme elongation of the axonal and dendritic arbor poses an additional challenge to the ability of a neuron and other dendritic compartments to the whole dendritic arbor.

The half-life of a protein, in the order of five days, [8], is considerably smaller than the life span of a neuron, which can live as long as a human being. Therefore, during its life, each protein is replaced thousands of times. Despite this fast protein turnover, the connections between neurons can retain memories for decades. In this thesis, I approached the problem of how a neuron can keep providing a steady supply of proteins to each of its compartments.

The three main strategies to have proteins available in distal dendrites are to produce them in the soma and let them diffuse and explore the dendritic freely, they could be attached to a set of molecular motor and being actively transported in dendritic trees, or they could be produced in the dendrites. Having a constant distribution of mRNA in the dendritic trees is the option that minimizes the protein required by the neuron to populate it, but it opens to the problem of transporting mRNA in dendrites; mRNAs, when compared to proteins, have a lower half-life, in the order of few hours.

In sec 1.1 I gave a short description of the principal neuronal components involved in protein transport, and in Sec. 1.2 I gave an overview of the main mechanisms available to the neuron to transport proteins, mRNA, and other neuronal components.

1.1   Neuronal components

Neurons and glia are the two primary components the nervous system. The role of glia is mostly supportive of the neuronal functions, ranging from providing a scaffolding that keeps neurons in

place to controlling the inflammatory response to providing nutrients to neurons [9, 10]. Neurons (see Fig. 1) are the main actors responsible for neuronal computation; they are composed of three main components: the soma, where the nucleus of the cell is, the dendrites, and the axons. The three components are responsible for three distinct tasks, the soma is needed to produce the majority of the neuronal machinery, the dendrites to are needed to receive and integrate excitatory and inhibitory inputs from other neurons, and axons are responsible for transmit the outgoing signal to other neurons.
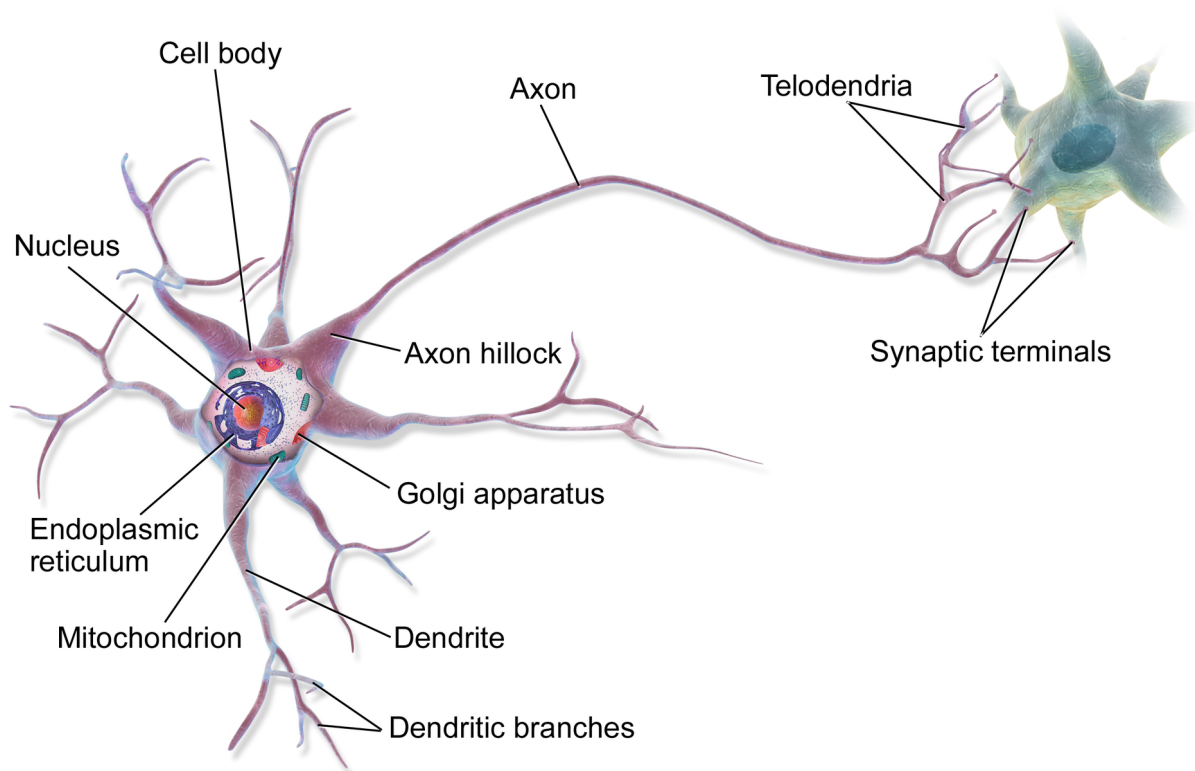
Figure 1: **Diagram of the Neuronal Structure** Diagram of the Neuronal Structure, with the names of its principal components. Image source: work by BruceBlaus, via Wikimedia Commons (Creative Commons).

1.1.1   The Soma

The soma is the central compartment of the neuron; it is approximately spherical, with a diameter of approximately $20\mu m$. A bilipidic layer surrounds the soma, separating it from the external
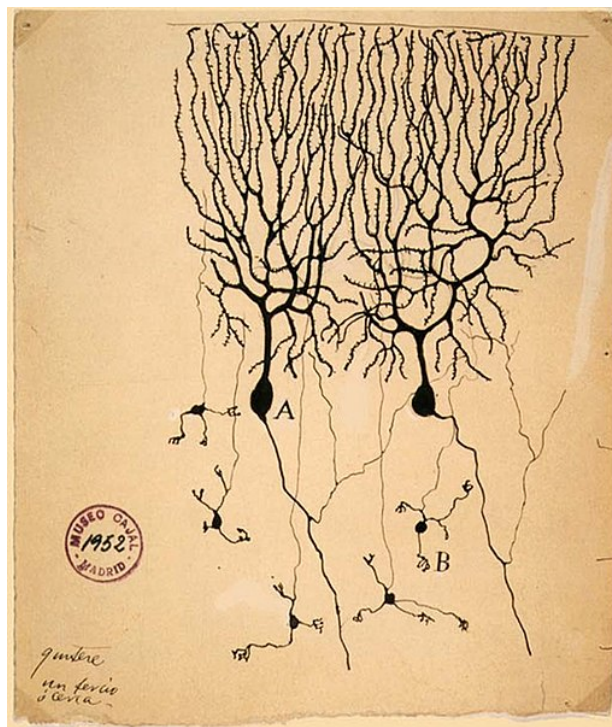
Figure 2: **Dendritic Structure: original drawing** Examples of dendritic morphologies, A) Purkinje cells, B) Granule cells. Image source: draw by Ramon y Cajal, Madrid 1899.

environment; inside the membrane, there is the cytoplasm, the solution containing nutrients, proteins, and other neuronal structures and organelles. The main neuronal structures in the soma are the nucleus, the smooth and rough endoplasmic reticulum, and the Golgi apparatus.

The main task of the endoplasmic reticulum is to synthesize lipids and proteins; the external side of the rough endoplasmic reticulum is rich in ribosomes. For a long time, it has been thought to be the only source of proteins in the neuron. At the end of the 90s, evidence started to accumulate suggesting that proteins were also assembled inside the dendritic arbor [11].

1.1.2   Dendrites

The dendrites are the apparatus that the neuron uses to receive signals from other neurons. It presents a highly diverse and stereotyped morphology that has been used to classify neurons, see Fig. 2. Different classes of neurons have different typical dendritic trees: granule cells have a dendritic arbor spanning a hundred micrometers, while pyramidal neurons can reach up to

thousands of micrometers. Neurons use different morphologies to collect input from a specific area of the brain. A typical example are Purkinje cells [12], their dendritic tree is a planar and highly symmetrical morphology with up to 20-30 consecutive branches [3].

A dendrite is a pipe-like structure where a cylindrical bilipidic layer surrounds the internal cytoplasm. Mature dendrites present extrusions called spines. there are approximatly 0.5-2 spines per micrometer, [13]. Spines are almost isolated neuronal compartments that host synapses, the connection between neurons.

The radius of a dendrite in the brain spans from $0.1 \mu m$ in granule cells to few micrometers in basal pyramidal dendrites, [14]. Some classes of neurons, like the neurons in the stomatogastric ganglia of crabs, have a very disordered structure, where some of the radii can reach $50 \mu m$ micrometer, [2]. The length of a dendrite can refer to either the distance between the soma and the dendritic tip or the distance between two consecutive branches. In this thesis, I used the latter definition of length.

The surface of a dendrite is composed of a bilipidic layer like the one that surrounds the soma, and inside the cytoplasm contains many of the same organelles and structures. For example, the endoplasmic reticulum is the largest structure inside the dendritic tree, followed by the mitochondria. Other organelles that play an essential role in dendritic functioning are ribosomes, lysosomes, and proteosomes.

Dendrites integrate the signal from presynaptic neurons and transmit it to the juncture between the soma and the axon, called axon hillock, where an action potential is initiated and transmitted to postsynaptic dendrites. To do so, the dendrite needs to stretch and branch to be able to meet presynaptic axons. The morphology that a neuron can assume to connect to a fixed set of the presynaptic axon is explored in [15]. The authors explained the different types of morphologies that neurons exhibit by balancing maximizing the signal transmission from the synapse to the soma and minimizing the wiring cost of the dendrite.

1.1.3   Axons

Axons, along with dendrites, are a structure unique to neurons. While the role of dendrites is to receive and integrate the signal, the role of the axons is to transmit action potentials to postsynaptic neurons. The axon starts at the soma, in a region called axon hillock. For years the hillock has been thought to be the place where the somatic action potential was initiated.

After the initial segment, the axon can be surrounded by a protective membrane formed by astrocytes called myeline. Myeline helps with the physical and electrical insulant from surrounding electric signals. The axon often splits and branches in a complex tree; each sub-branch is called telodendria. At the end of each telodendrion, there is an axon terminal where synaptic vesicles containing neurotransmitters are located. The total length of an axonal tree can be even longer than a meter, like in the human sciatic nerve [16]. In recent years it has been observed that somatic action potentials are initiated in the *initial segment*, the area between the axon hillock and the first unmyelinated segment of the axon.

1.1.4   Endoplasmic Reticulum

The endoplasmic reticulum, ER, in cells is principally responsible for synthesizing lipids and cholesterols. In neurons, it also assumes an important role in protein transport. The ER is constituted by an irregular network that effectively connects the whole neurons, from the soma to the distal dendrites, to the axon, and it even enters in synapses, playing a role in synaptic stabilization [17]. The presence of ER in dendrites correlates with the spine density, [18], and it acts as a reservoir of proteins in dendrites, [19] providing membrane proteins, such as glutamate receptors, in dendrites [20]. A 3DEM reconstruction of the SER in dendrites is shown in [21].

1.1.5   Microtubules and Molecular Motors

Microtubules and actins are two types of microfilaments that constitute the cytoskeleton of a neuron. As such, they are a key component of maintaining the external structure of a cell. In
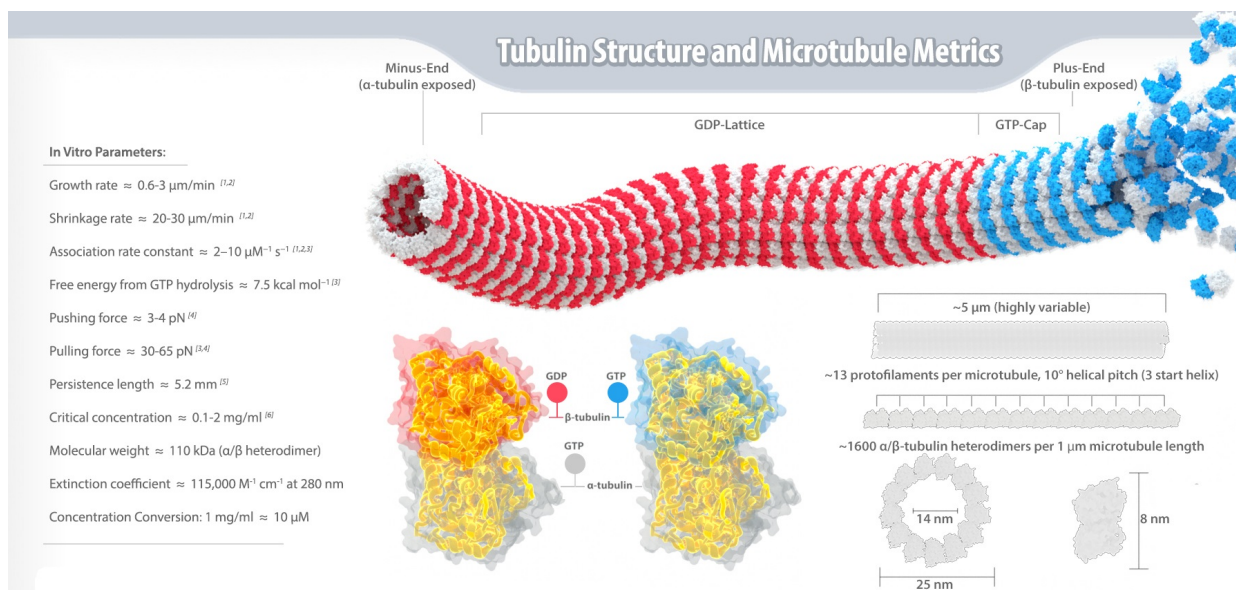
Figure 3: **Infographic of tubulin and Microtubules dynamic** This figure shows the microtubules structure, and its most important parameters. Adapted from Wikipedia Common (Creative Commons), the data showed are summarized from [22, 23, 24, 25, 26, 27].

addition to that, they play an essential role during dendritogenesis, leading the growth direction of both dendrites and axons.

Microtubules are a polymer of tubulin α and tubulin β organized in a repetitive pattern, see Fig. 3. Microtubules show a characteristic orientation, and as shown in Fig. 3, the side with the β-tubulin exposed is referred to as "plus-end", while the other as "minus-end". Microtubules are involved in transporting protein and organelle together with a class of enzymes called molecular motors.

The two relevant super-families of molecular motors that bind to microtubules are kinesins, and dyneins [28]. A third family of molecular motors, myosins, binds on actins, another type of microfilaments. Microtubules are involved in the transport processes across the dendrites and the axons. For this thesis's scope, actins are involved only with the active transport inside the synapses.

As schematized in Fig. 3, the plus-end of a microtubule is highly dynamic, while the minus-end is much more stable. The growth rate of microtubules is particularly relevant during

dendritogenesis, ranging from 0.6 $\mu m/min$ to 3 $\mu m/min$, while the shrinking rate can reach up to $30 \mu m/min$. There are genes for 17 distinct types of tubulin in Humans; further complexity is achieved by post-translational-modifications, PTMs, like acetylation, that stabilizes the plus-end of microtubules. Other modifications to the microtubules can be achieved using Microtubule-associated-proteins MAP; for example, Katanin, Spastin, and Fidgetin cut the microtubule, MAP2 limits the binding of Kinesin-1 to microtubules and its speed, while MAP-7 increases the motility of Kinesin-7.

In axons, microtubules grow parallel and with the same orientation as the ones already there. One of the main actor responsible for this alignment is the protein, $\gamma-$TuRC. Conversely, in dendrites, the microtubule orientation is more randomized, with a 50% plus-end-out and 50% minus-end-out in proximal dendrites [29].

Molecular motors are the second main ingredient necessary to explain the fast transport of neuronal components in axons and dendrites. In Humans, there are 45 genes that code for different kinesins, divided into 14 sub-groups. While there are nine families of dyneins in eukaryotes [30]. Different molecular motors have different velocities and affinities to microtubules. In general, kinesins travel to the plus-end of the microtubule and dyneins toward its minus end.

The neuron can use the different specificity of molecular motors to microtubule to ship a specific cargo. Kinesin-1, for example, does not enter into dendrites, while Kinesin-3 enters both in dendrites and axons. More information about microtubules and molecular motor properties can be found in Burute's review: [28].

1.2   Neuronal Transport

Like every other type of cell, a neuron requires a steady amount of proteins and organelles to survive and sustain its functions. The total number of proteins in a neuron can be estimated to $16 \cdot 10^9$ proteins in a pyramidal cell. To obtain this value, I multiplied the estimated protein density found in [31], $\rho_V = 2 - 4 \cdot 10^6$ proteins$/\mu m^3$, with the estimated volume of a pyramidal neuron

obtained from [32]. $5.3 \cdot 10^3 \mu m^3$. I obtained the volume estimation by adding the estimated volumes of soma, axons, and dendrites.

Under the assumption that the dendrites are ideal cylinders, the dendritic volume is obtained by multiplying their average length, $L_d = 3.08mm$, and their average radius $r_d = 0.45 \mu m$. Therefore, the average dendritic volume is: $V_d = 2 \cdot 10^3 \mu m^3$. Similarly, the average axonal volume is obtained by the average length, $L_a = 10 - 40mm$ and the average radius $r_a = 0.15$, leading to an average axonal volume of $0.7 - 2.8 \cdot 10^3 \mu m^3$. Finally, the somatic volume is obtained by approximating the soma as a sphere of radius $5\mu m$, leading to a somatic volume of $V_s = 520 \mu m^3$. Because the protein density found in [31], the estimated number of proteins in the soma of a pyramidal neuron is $1.6 \ 10^9$, in its dendritic tree is $6 \ 10^9$, and in its axonal tree $8.4 \ 10^9$.

Because of the typical half-life of a protein of 4-6 days, [8], each cell has to produce, traffick and replace, $N = \frac{N_{tot}}{2T_{1/2}} \sim 1.6 \cdot 10^4$ new proteins every second, of these ~ 7000 are directed to the dendritic tree. Here I used $T_{1/2} = 5$ days and, $\rho_V = 3 \ 10^6$ proteins/μm^3.

Given the limited amount of proteins a neuron destinates to the dendrites, is important to understand the upsides and shortcomings of different transport mechanisms. The three main pathways for a protein to reach the tip of the dendritic or axonal arbor are:

1. reach that location using diffusion,

2. reach that location using active transport,

3. being synthesized in that location directly.

A new strategy has been suggested for axons in recent years: recruit proteins from external astrocytes, [33].

1.2.1   Unbiased Diffusion:

Diffusion was first described by Fick in 1855 [34] while studying the evolution of the concentration of salt between two water containers. Einstein and Stokes gave a mechanistic interpretation

to Fick's second law. They related the diffusion movement to the imbalance of the elastic colli-
sion on a rigid sphere; they proved that the diffusion coefficient of a rigid non-interacting sphere
is inversely proportional to the radius of the sphere. For this reason, small, non-interacting pro-
teins like GFP have a high diffusion coefficient, up to $D = 9 \pm 2 \mu m^2/s$, [35]. When describing the
movement of bigger proteins, or an organelle, the diffusion equation does not hold exactly any-
more because space is not homogeneous at the protein scale because of extra dendritic structures
like ER and mitochondria. The same is true for interacting proteins; once they bind to another
protein, the radius of the complex they form is bigger and affects the apparent diffusion coeffi-
cient. For example, Claritin-L, is a protein that plays a major role in the formation of vesicles,
and its diffusion coefficient is $D = 0.0096 \mu m^2/s$, see [36]. This anchoring mechanism is used in
synapses to anchor AMPA receptors to PSD-95, [37], and PSD-95 to $\alpha-$Actinin [38].

Similarly, organelles and vesicles are also big enough to have a very limited diffusion co-
efficient, approximatively $D = 0.0061 \mu m^2/s$, [39]. The diffusion coefficient, together with the
half-life of a diffusing particle, play an essential role to understand how far it can diffuse before
being recycled: the diffusion length $\lambda = \sqrt{\frac{DT_{1/2}}{\log(2)}}$, represents the average distance traveled by a
protein or another neuronal component before being dismantled.

For a typical half-life of 5 days [8], the diffusion length of a proteins spans from $2500 \mu m$
for high diffusion coefficient, $(D = 10 \mu m^2/s)$ to $25 \mu m$ for proteins with low diffusion coefficients
$D = 0.001 \mu m^2/s$; this means that pure diffusion is a simple and suitable process to distribute
small non-interactive proteins in the dendritic tree.

A classic example of surface proteins are the AMPA-channels; an average synapse requires
60 AMPA receptors, and, considering their synaptic dwell time of 3-7 seconds, [40], their lateral
diffusion across the dendrite plays an important role in understanding their availability at the
synapses; in [41] was shown that this lateral redistribution could predict the so-called synaptic
normalization. AMPA receptors can bind an anchor protein in the synapse called PSD95, which
increases the time that an AMPA receptor spend in a synapse up to 2-4 hours, [42]

1.2.2 Active transport

Large proteins and other dendritic components with small diffusion lengths cannot reach distal dendritic sites only via diffusion. In order to have access to those components in distal dendrites, the neuron must make use of other mechanisms. One of them is to use the molecular motors described in Sec. 1.1.5. As discussed in Sec. 1.1.5, the movement of a cargo transporting either organelles, proteins or mRNA, is driven by molecular motors. The two main families of molecular motors have a different preferred direction along each microtubule, and also, the orientation of the microtubules is not constant along the dendritic arbor, and the microtubules tend to organize themself in bundles with the same orientation [28]. The resulting movement can be studied by tagging the cargo with a fluorophore and recording their position in time with a kymograph, as showed in [43].

Modeling active transport is a complex task, and many models have been proposed in the past years. The mechanisms of multiple motors pushing and pulling a cargo in different directions are often referred to as *tug-of-war*, a metaphor introduced in 1998 in [44] and discussed in detail in [45, 46].

In this scenario, many molecular motors pull the same cargo in different directions, resulting in a chaotic behavior where the net movement alternate from retrograde to immobilized to antiretrograde. In [47], the authors showed that both the length of a run and the net velocity of a cargo depend upon the cargo load and the density of ATP.

While active transport has the advantage of speeding up the transport inside the dendrites, it came with the cost of at least 125 ATP per micrometer per molecular motor [48]. The the distribution of the length of the distance between two consecutive change of the direction of a cargo has been modeled, in [49], as a Lèvy walk, and the authors observed that the probability distribution of the waiting time before two movement is long-tailed.

1.2.3   Local Translation

The third main pathway available to the neuron to have protein in distal dendrite is to synthesize them *in situ*. The first indication that the mRNA found in dendrite is translated into proteins and is required for synaptic plasticity is described in [11]. Since then, the understanding of the importance of locally translated proteins and their role in long-term plasticity grew steadily [50, 51, 52]. As I showed, constant availability of mRNA in the dendritic arbor, and therefore a constant production of newly synthesized proteins, leads to a flat distribution of proteins in the dendritic arbor and minimizes the protein requirement in the dendrite.

The minimization of the protein requirement comes with the cost of needing to transport mRNA into the dendritic arbor. This can happen with the two main methods described above, either active or passive transport. The additional level of difficulty for mRNA is its lower half-life; mRNA half-life ranges from 140 minutes for arc mRNA [53], an mRNA transported into a single tagged synapse, [54], to 7 hours for more stable mRNA, like the b-globin mRNA [55], to 10.5 hours reported in [56].

In [57], the authors explore the problem of how a dendrite can function stably despite the small number of available mRNA in dendrites and the consequent higher expected variability in the protein availability. The scarsity of mRNA in dendrites allows only a fraction of spines to undergo local translation, and they suggested that this would induce a selectivity of which synapsis have access to long term plasticity.

To understand the local translation in dendrites and synapses is essential to consider the ribosomes, the machinery needed for protein translation. The amount of ribosomes in synapses of a hippocampal neuron varies from zero to eight ribosomes per synapse [54], allowing different synapses to react and adapt to stimuli in distinct ways.

2   Protein Density

2.1   Diffusion equation

The diffusion equation is a partial differential equation of the first order in time and second order in space that can be used to describe many different physical phenomena. It was first introduced by Adolf Fick in 1855 [34] to describe the evolution of the concentration of salt between two water containers. The First Fick's Law describes the flux of the soluble salt in water:

$$\Phi(x) = -D\frac{d\rho(x)}{dx}. \tag{5}$$

The second Fick's Law is what today is referred to as *diffusion equation*, and states the temporal evolution of the density of a diffusing species in a media:

$$\frac{\partial\rho(x,t)}{\partial t} = D\frac{\partial^2\rho(x,t)}{\partial x^2}. \tag{6}$$

An alternative formalization of the diffusion equation starts from the continuity equation:

$$\frac{d}{dt}\rho(x) = -\nabla\cdot\Phi(x) + K_1(x) - K_2(x), \tag{7}$$

where $K_1(x)$ is the source term, while $K_2(x)$ is the sink term.

Integrating Eq. 7 over an interval dx, its left side represents the variation of the density $\rho(x,t)$, in time, and the right side of it represents how many proteins are entering into $x, x + \delta x$ minus the ones that are leaving the same interval, plus the number of objects that are produced in it, minus the ones that are destroyed at the same location. By setting $K_1 = K_2 = 0$, the second Fick's Law can be obtained using the continuity equation and by imposing the flux described in the first Fick's law.

A more general definition of the flux that includes a velocity term is:

$$\Phi(x,t) = -D\rho'(x,t) - v\rho(x,t),\tag{8}$$

leads to more general diffusion equations like the the convection-diffusion equation also called diffusion with drift.

$$\frac{d\rho(x)}{dt} = D\frac{d^2\rho(x)}{dx^2} + v\frac{d\rho(x)}{dx}.\tag{9}$$

2.1.1   Diffusion on the ER: Fractal and Random Walk Dimensions

One of the main assumptions underlying the diffusion equation is that the space the proteins are exploring must be isotropic; namely, the ability of a protein to diffuse toward the left or the right should not be affected by the exact position where the protein is. If this requirement is relaxed, the problem become more complex, but it allows to study diffusive process on disordered structures, like discussed in [58]. In [59] the authors shows that the mean square displacement, MSD in the ER is subdiffusive:

$$\mathrm{MSD}(t) \approx t^{0.5},\tag{10}$$

where the exponent is called anomalous diffusion exponent, [60]. Eq.10 is often written in term of the *random walk dimension*, d_W:

$$\mathrm{MSD}(t) \sim t^{2/d_W}.\tag{11}$$

The anomalous diffusion exponent and the random walk dimension should not be confused with the *fractal dimension*, d_F, that can be measured using a box-counting algorithm; the authors in [59] also measured the fractal dimension of the endoplasmic reticulum: $d_f \approx 1.6$.

The fractal dimension and the random walk dimension are generally not the same, and if

the graph is *smooth*, as defined in [61] the two are linked by the relation:

$$d_W = d_F + 2 - d_\Omega, \tag{12}$$

where d_Ω is the resistance dimension, [61, 62].

How to approach the description of anomalous diffusion is still an open problem, and accordingly, to the scale one is interested it can be investigated by making use of Continuous-Time-Random-Walks (CTRW), or the fractional Focker-Planck equation, [63].

Anomalous diffusion with an anomalous exponent smaller than one, as in the diffusion in the ER, is less efficient at populating the distal dendrites than normal diffusion, so in this thesis, I focused my attention on normal diffusion. For this reason, in the following, I referred often to surface proteins and not to membrane-associated protein to refer specifically to the membrane-associated proteins that are diffusing on the surface of the dendrite.

2.1.2   Dimensionality Reduction

When proteins diffuse in a linear dendrite, they explore it in all three dimensions. Because of the radial symmetry of a neuronal process, namely axons and dendrites, which can be approximated to a pipe of diameter diam $\lesssim 1.5\mu m$ and a length up to hundreds of micrometers, I assumed that the protein density is homogenous in the cross-section of the dendrite. This allowed me to decouple the diffusion in the cross-section plane from the diffusion along the dendrite and to define the linear density of proteins as:

$$\rho(x) = \int_A \rho(x, y, z) \, dy dz, \tag{13}$$

where A is the cross-section of the dendrite for cytoplasmic proteins, or its circumference for surface proteins. If interested in the surface density for membrane-associated proteins or in the volumetric density for soluble proteins, one needs to divide the linear density, $\rho(x)$ by the radius

or radius square of the dendrite, respectively. In the following, I referred to the linear density $\rho(x)$ as protein density.

While the proteins are diffusing on a linear dendrite, their movement along the x-axis is affected by the medium only due to the different viscosity of the medium itself, and the shape and binding rate of the protein, leading to a different diffusion coefficient for each protein, both classes of proteins follow the same diffusion equation:

$$\frac{\partial}{\partial t}\rho(x,t) = D\frac{\partial^2}{\partial x^2}\rho(x,t).$$ (14)

See Eq. 116 in the Appendix for the temporal evolution of this system on an infinite dendrite if all the proteins were concentrated in a narrow area at $t = 0$.

The main difference between surface and cytoplasmic proteins is encountered at a branch, and it is discussed in Sec. 2.5.

2.1.3   Diffusion, Protein Synthesis and Degradation

The first two main ingredients of the model are the production and the degradation of proteins. If only the production of proteins is included in the model, the overall number of proteins would grow linearly, and conversely, if only the degradation is included, the number of proteins would decrease exponentially, and no proteins would be left in the system. A protein synthesis that is not compensating for protein degradation leads to a transient protein density that can be used to model a different demand of proteins after STP or STD [6].

Protein synthesis happens when a ribosome translates an mRNA into a protein and degradation where a protein encounters either a lysosome or a proteasome. These three organelles are discrete objects, but their contribution can be described using a smooth function due to the uncertainty about their position.

In this work, I assumed that lysosomes and proteosomes distributions are constant and abundant in the dendritic arbor, and therefore the degradation term can be written as the fraction

of proteins that are encountering a recycling organelle:

$$DEG = \phi \, \rho(x,t). \tag{15}$$

The proportionality factor, ϕ, is the inverse of the mean life of a protein, τ, or inversely propor-

tional to the half-life, $T_{1/2}$:

$$\phi = \frac{1}{\tau} = \frac{\log(2)}{T_{1/2}}. \tag{16}$$

The production term can be written as:

$$SYNT = \beta \, \rho_{mRNA}(x,t), \tag{17}$$

where $\rho_{mRNA}(x,t)$ is the amount of mRNA at position x at time t. In the following, I included all

the information about mRNA abundance, and ribosomes accessibility in a single function $\varepsilon(x)$:

$$SYNT = \varepsilon(x,t). \tag{18}$$

Including these two terms into Eq. 6 I obtained the diffusion equation with protein degradation

and production:

$$\frac{\partial}{\partial t}\rho(x,t) = D\frac{\partial^2}{\partial x^2}\rho(x,t) - \phi\rho(x,t) + \varepsilon(x,t). \tag{19}$$

If there is no net influx of proteins from either side of the dendrite, A and B, and assuming

that the following limit exists,

$$\lim_{t \to \infty} \int_A^B \varepsilon(x)\,dx = E, \tag{20}$$

Eq. 19 allows to calculate the amount of proteins at equilibrium:

$$N_{eq} = \frac{E}{\phi} \tag{21}$$

If proteins are synthesized outside of the dendrite, for example, in the soma, the synthesis

therm can be described by setting the flux of protein at zero $\Phi(0) = \beta$; an equivalent way is to set the flux of proteins at zero to $\Phi(0) = 0$ and adding a synthesis term in zero: $\beta\delta(x)$.

2.1.4   The equilibrium

In this work, I often considered the distribution of proteins at equilibrium, namely the distribution of proteins after a time that is considerably bigger than all the time scales of the system: in this work, this means $t \gg T_{1/2}$.

Under this condition the distribution of proteins $\rho(x,t)$ doesn't depend on time and instead of considering a partial differential equation (PDE), I simplified Eq. 19 into a ordinary differential equation (ODE):

$$0 = D\frac{\partial^2}{\partial x^2}\rho(x) - \phi\rho(x) + \varepsilon(x). \tag{22}$$

An ODE of second-order, like Eq. 22, is fully determined by two boundary conditions.

In Appendix, I showed how to obtain the general solution to Eq. 22 in two ways: either by taking the limit of the general solution of Eq. 19, see Sec. A.2, or by solving Eq. 22 directly, see Sec. B. The advantage of working directly with the ODE, as I did in Sec. B, is that it allows to impose the boundary conditions in an easier and more intuitive way.

2.1.5   Boundary conditions

The diffusion equation with degradation and synthesis, Eq. 19, is a partial differential equation of the first order in t and of the second order in x. Its solution is fully specified, imposing its initial condition, IC, and two boundary conditions. At the same time, the diffusion equation with degradation and synthesis, Eq. 22 at equilibrium is a second-order differential equation which solution is fully determined by two boundary conditions.

Here I focused on the boundary conditions that can be imposed on the diffusion equation at equilibrium. The general solution to Eq. 22 is given in Appendix in Sec. B. The way the two boundary conditions are imposed depends on the domain upon which one is solving the

differential equation, and therefore on the approximation that have been done about the geometry of the dendrite.

In the first scenario, I considered a dendrite that is significantly longer than the typical distance explored by the protein of interest, *span*; and the proteins are synthesized in a localized area of the dendrite. The first scenario can describe the synthesis of synaptic proteins in a spine or the burst in translation following synaptic activation, [6]; this can be modeled by considering the diffusion equation on an infinite support: $x \in (-\infty, \infty)$. Furthermore, the two boundary conditions are obtained by imposing a vanishing abundance of proteins far away from the region where the proteins are synthesized. The two boundary conditions for the first scenario are:

$$\lim_{x \to \infty} \rho(x) = 0 \tag{23}$$

and

$$\lim_{x \to -\infty} \rho(x) = 0. \tag{24}$$

From a practical point, one of the two boundary condition could be replaced by imposing the number of proteins in the system:

$$\int_{-\infty}^{\infty} \rho(x)\,dx < \inf, \tag{25}$$

because to have a finite integral, vanishing conditions at the infinite are required.

In the second scenario, I assumed that the proteins are produced in the proximity of the soma, $x = 0$, and the length of the dendrite is longer than the typical span of the protein of interest. This can be modeled by considering a semi-infinite dendrite: $x \in [0, \infty)$. The boundary conditions for this system are vanishing density at infinite:

$$\lim_{x \to \infty} \rho(x) = 0; \tag{26}$$

and the flux of proteins at the soma:

$$\Phi(0) = \beta = N\frac{\log(2)}{T_{1/2}}. \tag{27}$$

From a practical point, one of the two boundary condition could be replaced by imposing the number of proteins in the system:

$$\int_0^\infty \rho(x)\,dx = N. \tag{28}$$

In the last scenario, I considered dendrites with a length comparable to the typical span of the protein of interest. In this scenario, I had to consider the finite length of the dendrite. This can be modeled by imposing the differential equation's domain: $x \in [0, L]$.

To impose the boundary condition at $x = L$, one has to understand the behavior of the proteins that reach the termination of the dendrite. If the dendrite is perfectly sealed, no protein can escape and one can impose a no-flux condition at $x = L$:

$$\Phi(L) = -D\left.\frac{d\rho}{dx}\right|_{x=L} + v\rho(L) = 0 \tag{29}$$

If the dendrite is still in its growing stage, some of the proteins that reach the dendritic tip are absorbed and used to expand the dendrite. The limiting case where all the protein are absorbed can be modeled by imposing an absorbing condition at $x = L$:

$$\rho(L) = 0. \tag{30}$$

Finally, if the dendrite does not finish at $x = L$, but one wants to focus the analysis only in the range $x \in (0, L)$ they would need to specify the flux at $x = L$:

$$\Phi(L) = J, \tag{31}$$

this is the boundary condition I imposed for dendritic branches, in Sec. 2.5.

Similarly to what I did for the semi-infinite case the first boundary condition could either be imposed by setting the flux of proteins at $x = 0$ or by imposing the total number of proteins in the dendrite:

$$\Phi(0) = N\phi = \beta, \tag{32}$$

or

$$\int_0^L \rho(x)\, dx = N. \tag{33}$$

2.1.6   Diffusion, no local translation

A broad class of proteins is not actively transported in the dendritic tree, and their ability to populate the dendritic tree is solely based on their diffusion properties and on the location where the protein synthesis happens.

Here I focused on the case in which the proteins are synthesized in the soma, and they all diffuse into the dendrite from the same side of the dendrite, as a convention, from the left. Assuming a finite dendrite of length L, $x \in (0,L)$, the boundary conditions are $\Phi(L) = 0$, no-flux condition at the termination, and $\Phi(0) = \beta$, influx from the soma. The following differential equations describe this problem:

$$\begin{cases} D\frac{\partial^2 \rho(x)}{\partial x^2} - \phi\rho(x) = 0, \\[2mm] \qquad \Phi(0) = 0, \\[2mm] \qquad \Phi(L) = 0, \end{cases} \tag{34}$$

and they can be analytically solved, see Appendix Eq. 145:

$$\rho(x) = \frac{N}{\lambda} \frac{\cosh\left[\frac{L-x}{\lambda}\right]}{\sinh\left[\frac{L}{\lambda}\right]}, \tag{35}$$

where the number of proteins at equilibrium is $N = \frac{\beta}{\phi}$, and λ is the diffusion length defined as

$$\lambda = \sqrt{\frac{D}{\phi}}.$$ (36)

The dependency of Eq. 35 to its parameters is shown in Fig. 4 in blue.

2.1.7 Diffusion, constant local translation

In the second limiting case, I considered a finite dendrite of length L, with constant local translation and no influx of proteins from the soma. The constant local translation adds an extra term to the diffusion equation: $\frac{\pm\beta}{L}$, and the boundary conditions are $\Phi(L) = 0$, and $\Phi(0) = \beta$. The following differential equations describe this problem:

$$\begin{cases} D\frac{\partial^2 \rho(x)}{\partial x^2} - \phi\rho(x) + \frac{\beta}{L} = 0, \\ \qquad\qquad \Phi(0) = 0, \\ \qquad\qquad \Phi(L) = 0, \end{cases}$$ (37)

can be solved analytically, and the protein distribution is intuitively flat, Fig. 4, red; see Appendix Sec. D.2:

$$\rho(x) = \frac{\beta}{\phi L}.$$ (38)
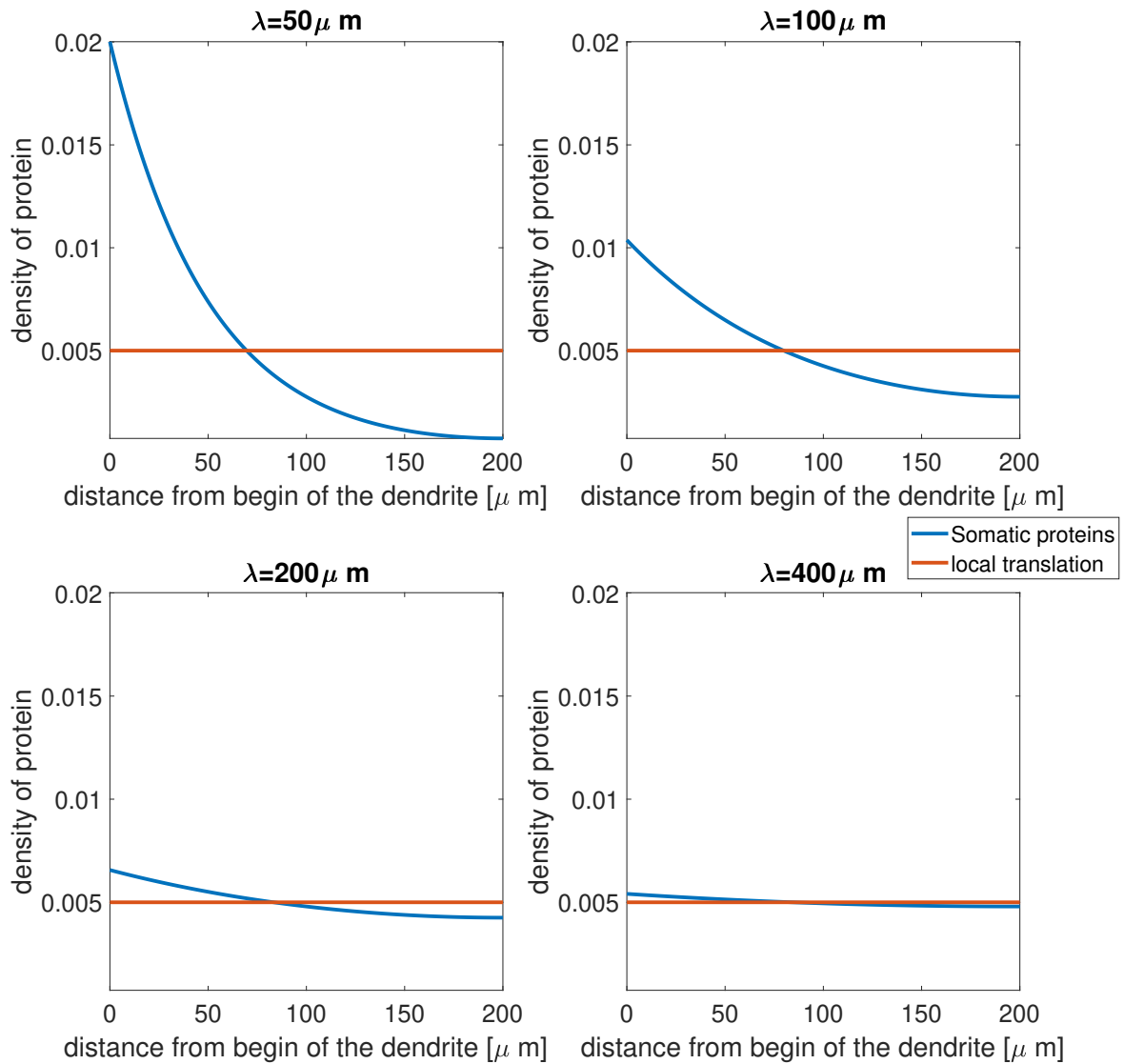
Figure 4: **Protein Distribution: Pure Diffusion** In This figure I showed the protein profile in case of purely diffusive proteins in a dendrite of fixed length $L = 200\mu m$, a protein half-life of 5 days and for different values of the diffusion length λ. In red the protein profile obtained by a flat protein translation is shown, in blue the protein profile obtained in case of somatic translation.

2.2   Active Transport

As described in the introduction, the two key components of active transport in dendrites are microtubules and molecular motors.

The first represents the infrastructure network along which molecular motors move protein, vesicles, and organelles in dendrites and axons. The two families of molecular motors active in axons and dendrites are Kinesin and Dynein. The first travels toward the plus-end of the microtubule, and the second toward the minus-end. In axons, all the microtubules are aligned with the plus-end out, while in dendrites, they present a more complex disposition [28].

As discussed in [1], the dynamics of a vesicle transported by molecular motors can be modeled by a three-state system, schematized in Fig. 5; the vesicle can move either toward the end of the dendrite or toward its beginning with velocity v, or being in a rest state. Other than the velocity, the other three additional parameters needed for the models are the retrograde-to-rest and antiretrograde-to-rest rates K_- and K_+, respectively, and the transition rate from rest to either retrograde or antiretrograde movement: K_0.
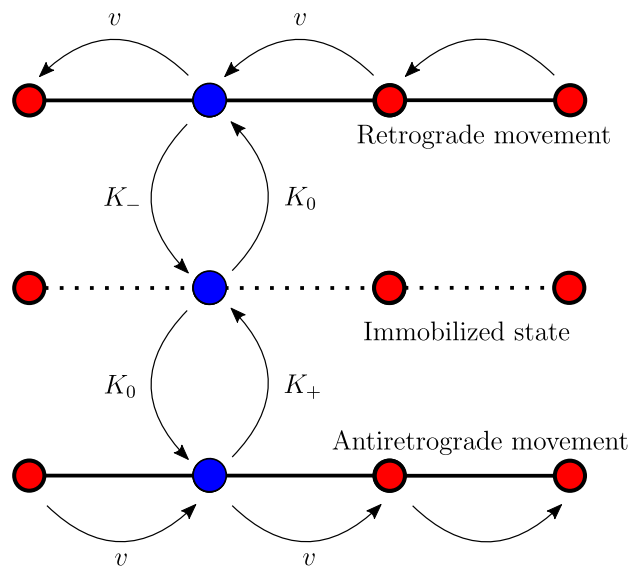
Figure 5: **Active Transport: Scheme of the three-state system** Active transport can be modeled as a three-state system where cargos could move retrogradely toward the soma (top line), stay still (center line), or toward the end of the dendrite (bottom line). In Bressloff [1], they showed how a rate from retrograde to immobilized different from antiretrograde to immobilized results in a net effective velocity.

Because of the stochastic nature of the retrograde/antiretrograde motion, the behavior of the transported cargo, for times bigger than the time scales of the transition rates, can be described

using an effective velocity v_{eff} and an effective diffusion coefficient D_{eff}:

$$v_{\text{eff}} = \frac{v}{\zeta}\left(\frac{1}{K_+} - \frac{1}{K_-}\right) \tag{39}$$

$$D_{\text{eff}} = \frac{(v - v_{\text{eff}})^2}{\zeta K_+^2} + \frac{(v - v_{\text{eff}})^2}{\zeta K_-^2}, \tag{40}$$

where

$$\zeta = \frac{1}{K_+} + \frac{1}{K_-} + \frac{1}{K_0}. \tag{41}$$

If the transition rates K_+ and K_- are identical, the system can be described by the diffusion equation discussed in the previous paragraphs but with a higher diffusion coefficient.

In this case, the fraction of time spent in the retrograde and antiretrograde state is the same. Knowing the typical time spent in the movement state τ, and the average length of a run l it is possible to identify l^2 as the mean squared displacement after a time τ, and therefore

$$D = \frac{l^2}{2\tau}. \tag{42}$$

Using this simplified relations one can describe the active transport of arc mRNA, [53], as an increased diffusion coefficient: the mean length of a run is $l = 7.3\,\mu m$ and the mean time spent in it is $\tau = 25.7\,s$, resulting in an effective diffusion coefficient $D = 0.97\,\mu m^2/s$.

In this section, I focused on that class of proteins and other actively transported dendritic components in the dendrites; more specifically, where the time spent in antiretrograde movement (toward the tip of the dendrite) is different from the time spent in retrograde movement, resulting in a non-zero effective velocity. In the following, for simplicity, I denoted the effective velocity with v.

$$\frac{\partial \rho}{\partial t} = D\frac{\partial^2 \rho}{\partial x^2} - v\frac{\partial \rho}{\partial x} - \phi\rho + \varepsilon(x). \tag{43}$$

A negative value of v represents a retrograde drift, and a positive velocity an antiretrograde move-

ment toward the dendritic tips.

2.2.1   Active transport and translation at the soma

I first considered the limiting case where all the mRNA are localized at the soma, and therefore the soma is the only source of proteins in the system. This can be modeled by setting the source term $\varepsilon(x)$ in Eq. 43 to zero, and imposing the no-flux boundary condition at the end of the dendrite, in $x = L$, and an influx β of protein from the soma in $x = 0$:

$$\begin{cases} \frac{\partial \rho}{\partial t} = D\frac{\partial^2 \rho}{\partial x^2} - v\frac{\partial \rho}{\partial x} = 0, \\[2mm] \qquad \Phi(0) = \beta, \\[2mm] \qquad \Phi(L) = 0, \end{cases} \tag{44}$$

The solution at the equilibrium of Eq. 44 can be obtained using the methods described in the Appendix, see Eq.153. Its functional form is relatively complex, so I chose a set of biologically plausible values of the diffusion coefficient and half-life, and I showed the protein profile in Fig. 6, blue.

2.2.2   Active transport and translation in dendrites

The other limiting case I discussed is when the mRNA distribution is flat throughout the whole dendritic arbor. This scenario is described by the following set of diffusion equations:

$$\begin{cases} \frac{\partial \rho}{\partial t} = D\frac{\partial^2 \rho}{\partial x^2} - v\frac{\partial \rho}{\partial x} + \frac{\beta}{L} = 0, \\[2mm] \qquad \Phi(0) = 0, \\[2mm] \qquad \Phi(L) = 0, \end{cases} \tag{45}$$

The complete analytical expression is in Appendix, in Sec. D.5; here, I chose a set of biologically plausible values of the diffusion coefficient and half-life, and I showed the protein profile in Fig.

6, red.

In section 3.3 and 3.2, I discussed the implications of those protein profiles in terms of the number of proteins that the neuron needs to produce to sustain the whole dendrite.
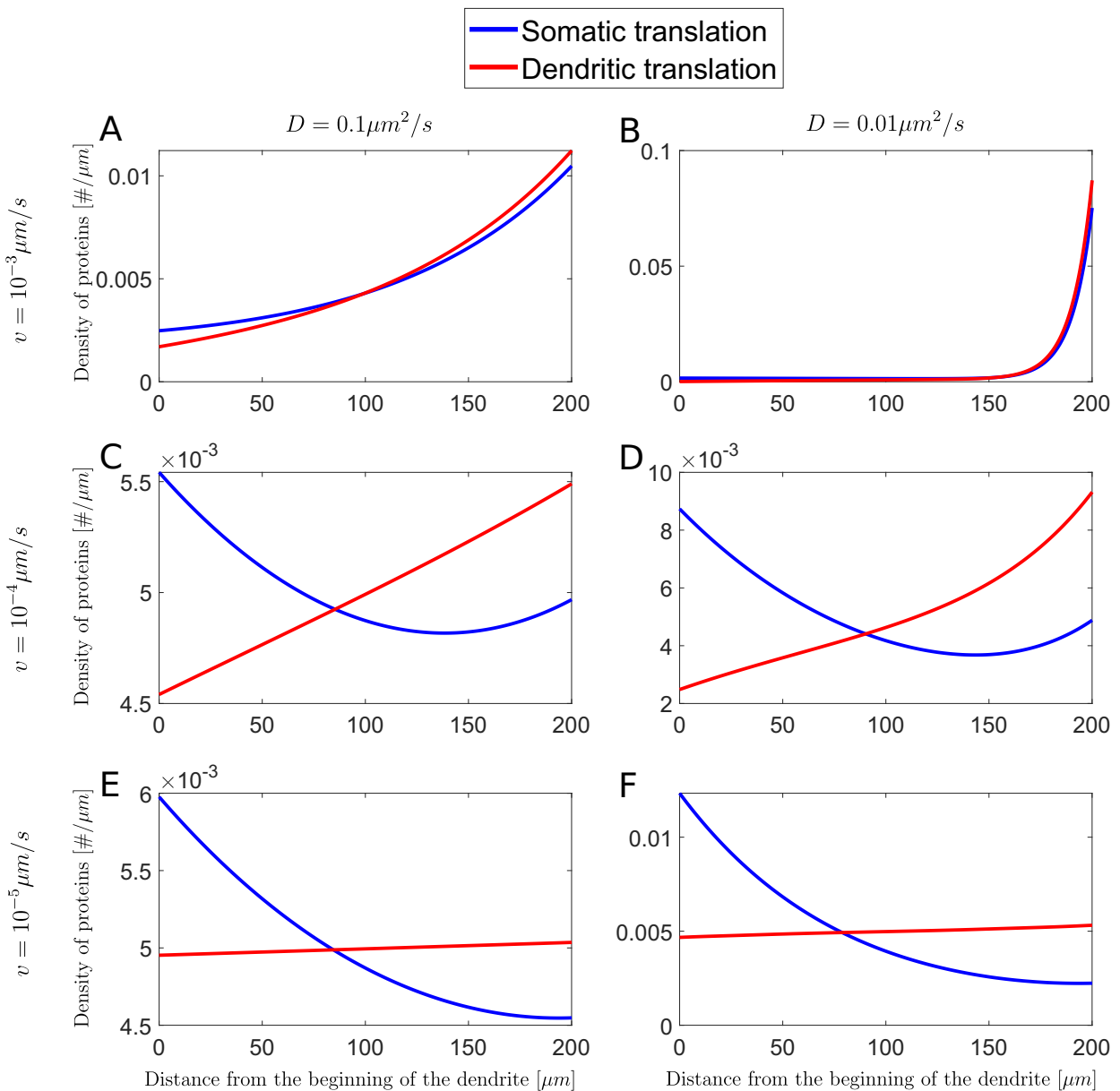
Figure 6: **Protein Distribution: Active Transport** In this figure, I show the protein profile in the case of active transport for a dendrite of fixed length $L = 200\mu m$, a protein half-life of 5 days, and for different values of v and D. In red, the protein profile obtained by a flat protein translation is shown; in blue, the protein profile obtained in the case of somatic translation.

In Fig. 6-B, the protein profile increases exponentially toward the dendritic tip. This arises

when the diffusion coefficient is insufficient to compensate for the active transport, and almost all the proteins accumulate at the dendritic tip.

This accumulation of proteins at the end of the dendrites, is due to the fact that the chosen diffusion coefficient is not big enough to compenesate for the active transport. Trapping mechanisms, like the one discussed in [49], could compensate this accumulation also without increasing the effective diffusion coefficient. I am currently working on the hypothesis that the protein intake into synapses could also reduce the accumulation of proteins in dendritic terminations.

2.3   mRNA Translation

In the previous paragraphs, I considered mRNA translation to happen either only at the soma or constant throughout the dendrite. This second model relies on the assumption that the availability of mRNA and ribosomes is independent of the distance from the soma, but this might be difficult for the dendrite to achieve. The mRNA is first transcribed in the soma and then trafficked in the dendrite, often via active transport. A better approximation for its availability in the dendritic tree, $\rho_{\mathrm{mRNA}}(x)$, is obtained by assuming a similar profile to what I obtained in Eq. 153, and shown in blue in Fig. 6. The protein density profile is therefore obtained by solving:

$$
\begin{cases}
D_{\mathrm{Protein}}\frac{\partial^2 \rho(x)}{\partial x^2} - \phi_{\mathrm{Protein}}\rho(x) + K\rho_{\mathrm{mRNA}}(x) = 0, \\[2mm]
\Phi\left(\rho_{\mathrm{Protein}}(0)\right) = 0, \\[2mm]
\Phi\left(\rho_{\mathrm{Protein}}(L)\right) = 0, \\[2mm]
D_{\mathrm{mRNA}}\frac{\partial^2 \rho(x)}{\partial x^2} - v_{\mathrm{mRNA}}\frac{\partial \rho_{\mathrm{mRNA}}(x)}{\partial x} - \phi_{\mathrm{mRNA}}\rho(x) = 0, \\[2mm]
\Phi\left(\rho_{\mathrm{mRNA}}(0)\right) = \beta_{\mathrm{mRNA}}, \\[2mm]
\Phi\left(\rho_{\mathrm{mRNA}}(L)\right) = 0,
\end{cases}
\tag{46}
$$

The system of equations 46 can be analytically solved, see Eq. 162 in Appendix. While the mRNA distribution is susceptible to the velocity of the active transport and can vary up to several

orders of magnitude for the chosen set of parameters, the protein distribution is considerably more stable across the dendritic arbor for a wide range of parameters. The profile of the protein distribution for different choices of D_p and v_m is shown in Fig. 7.
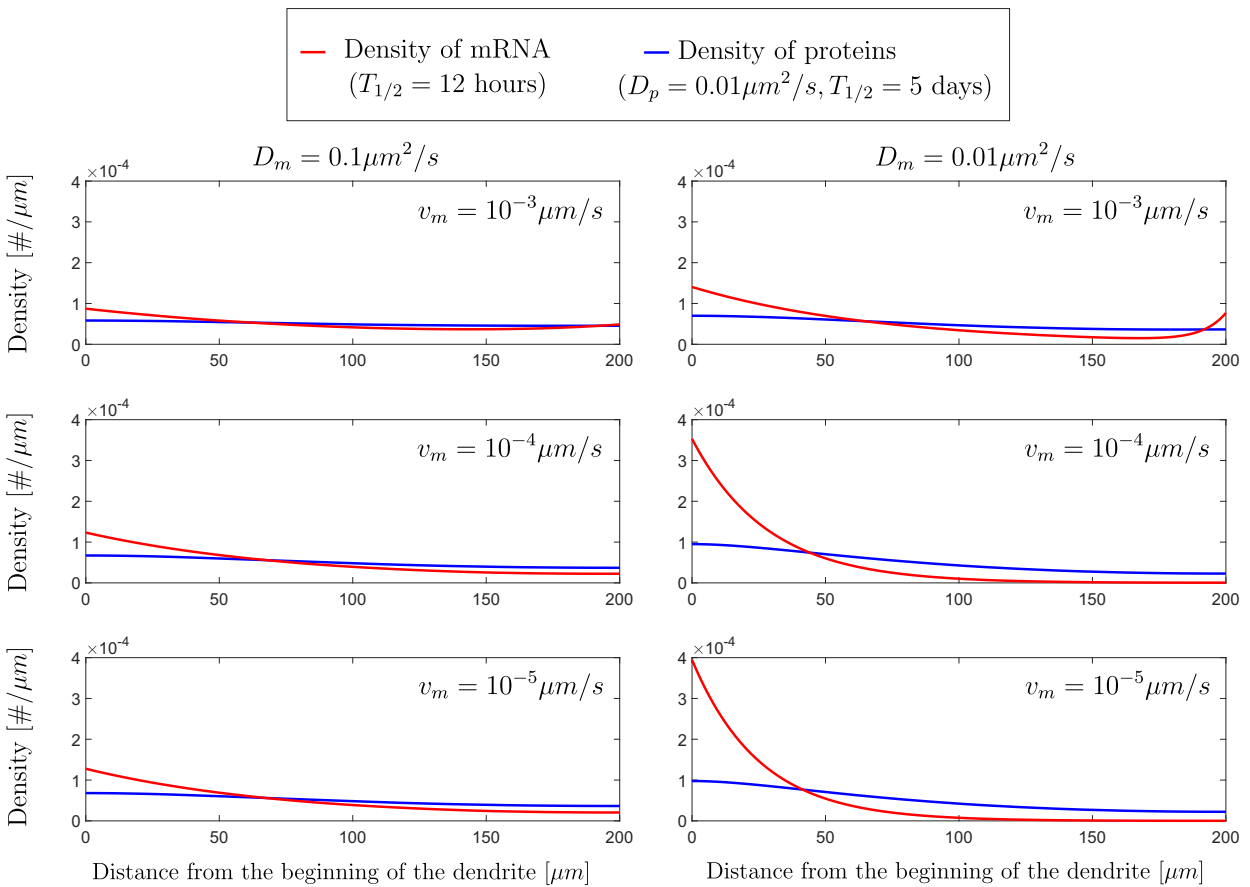
Figure 7: **Protein Distribution: Local translation of actively transported mRNA** In this figure, I showed the protein profile in case of active transport for an mRNA, and then it is translated into proteins in the dendritic tree. The mRNA and protein profiles are shown in red and blue, respectively. The length of the dendrite is kept fixed at $L = 200\mu m$. I set the parameters describing the dynamic of the proteins to $D_p = 0.01\mu m^2/s$ and $T_{1/2} = 5 days$. I varied the diffusion coefficient and velocity of mRNA from $0.01\mu m^2/s$ to $0.1\mu m^2/s$ and from $10^{-3}\mu m/s$ to $10^{-5}\mu m/s$ respectively, and I fixed its half-life to 12 hours. The production rates β_m and β_p are chosen such that $N_p = N_m = 1$.

2.4   Discrete Approach

Solving the differential equation and obtaining an analytical solution is often the best approach to understanding the protein profile in a dendrite but is not always viable. In the case of non-constant velocity or a dendritic tree with a high number of branches, an explicit solution of the differential equation might not be known.

An approach that allows incorporating discontinuities more simply is to discretize the time-dependent diffusion equation and let the system evolve to its equilibrium point. This approach is slower than solving the steady-state equations directly, but it allows the visualization of the temporal evolution of the protein profile. This numerical procedure allows to include branches, spines, and multiple populations of diffusive and actively transported particles in the same neuron; it only requires to know for each compartment of the dendritic tree the fraction of protein moving in it from each of its adjacent compartment. These information can be obtained by discretizing the diffusion equation; therefore, this method only requires knowing the morphology of the neuron, and the values of the parameters in it, usually half-life, velocity, and diffusion coefficient. Furthermore, understanding how to discretize a dendritic arbor correctly is a powerful way to get insight into a diffusive protein's behavior in different scenarios.

The idea behind the numerical approach is to discretize the diffusion equations and then follow step-by-step its temporal evolution using a forward Euler scheme, see [64]. For simplicity, I neglected the production term, which can be easily added later.

Let's start from the diffusion equation:

$$\frac{\partial \rho(x,t)}{\partial t} = D\frac{\partial^2 \rho(x,t)}{\partial x^2} - v\frac{\partial \rho(x,t)}{\partial x} - \phi\rho(x,t). \tag{47}$$

I can use finite difference approach to discretize the derivatives in Eq. 47:

$$f'(x) = \frac{f(x+\Delta x) - f(x)}{\Delta x} + O(\Delta x) = \frac{f(x+\Delta x) - f(x-\Delta x)}{2\Delta x} + O(\Delta x^2), \tag{48}$$

$$f''(x) = \frac{f(x+\Delta x) + f(x-\Delta x) - 2f(x)}{\Delta x^2} + O(\Delta x^2). \tag{49}$$

Eq. 47 becomes:

$$\rho(x,t+\Delta t) = \rho(x,t) + \Delta t \left[D\frac{\rho(x+\Delta x,t) + \rho(x-\Delta x,t) - 2\rho(x,t)}{\Delta x^2} \right.$$
$$\left. - v\frac{\rho(x+\Delta x,t) - \rho(x-\Delta x,t)}{2\Delta x} - \phi\rho(x,t) \right]. \tag{50}$$

Doing so I embedded the dendrite into a lattice with distance δx between nodes in the x direction, and δt, in time. For simplicity I assumed that δx and δt are constant. The biggest value of Δt that can be chosen without incour in numerical instabilities is:

$$\Delta t = \frac{\Delta x^2}{2D}, \tag{51}$$

Using it, I simplified Eq. 50 into

$$\rho(x,t+\delta t) = +\frac{1}{2}[\rho(x+\delta x) + \rho(x-\delta x)] + \frac{v\delta x}{4D}(\rho(x+\delta x) - \rho(x-\delta x)). \tag{52}$$

Using Eq. 51, simplifies considerably the equations and the code, but it introduces a saw tooth noise, described in [65]. For this reason, I averaged every measurement over an even number of compartments, usually 2.

The interpretation of Eq.52 is the follow: at time $t + \delta t$ the number of proteins in x is equal to half the sum of the molecules present at time t in the first neighbor of x: $x + \delta x$ and $x - \delta x$, plus a little bias toward positive or negative x, accordingly with the sign of v. A positive velocity v implies a bias toward positive x and a negative v a bias toward negative x.

An equivalent approach to this is summarized in Fig. 8: instead of describing for each compartment where it gets protein from, I assigned to each compartment a set of rules that instruct it to how many proteins it would transfer to adjacent compartments, in Fig. 8-A the schematization of a linear dendrite. The fraction of proteins moving toward an adjacent compartment can

be interpreted as the probability of a single protein moving in such a compartment. For a linear dendrite, these probabilities are:

$$P(x \to x + \delta x) = \frac{1}{2} + \delta x \frac{v}{4D} \tag{53}$$

$$P(x \to x - \delta x) = \frac{1}{2} - \delta x \frac{v}{4D}. \tag{54}$$

Using a similar argument on terminal branches, one can discretize Eq. 29 and show that:

$$P(L \to L) = \frac{1}{2} + \delta x \frac{v}{4D} \tag{55}$$

$$P(L \to L - \delta x) = \frac{1}{2} - \delta x \frac{v}{4D}, \tag{56}$$

, which is the same set of equations of the linear dendrite, but the proteins that would have moved to the compartment in $x = L + \delta x$ will stay in $x = L$.

2.5   Branches and boundary condition

The differential equations I presented so far are well defined when the considered dendrite is a simple cylinder. The majority of the dendritic arbor contains many consecutive branches, and the total length of the dendrites can be above 10 *mm*. It is therefore essential to understand how to include the presence of branching structures in the model. In this work, I labeled the mother dendrite, the one closer to the soma, with the subscript 0, and the two daughter dendrite with the subscripts 1 and 2, furthermore I oriented the dendrite in such a way that the compartment closest to the soma is at $x = 0$.

The first simplification to tackle the problem is to consider the distribution of proteins at equilibrium, which allows me to work with an ordinary diffusion equation of the second-order
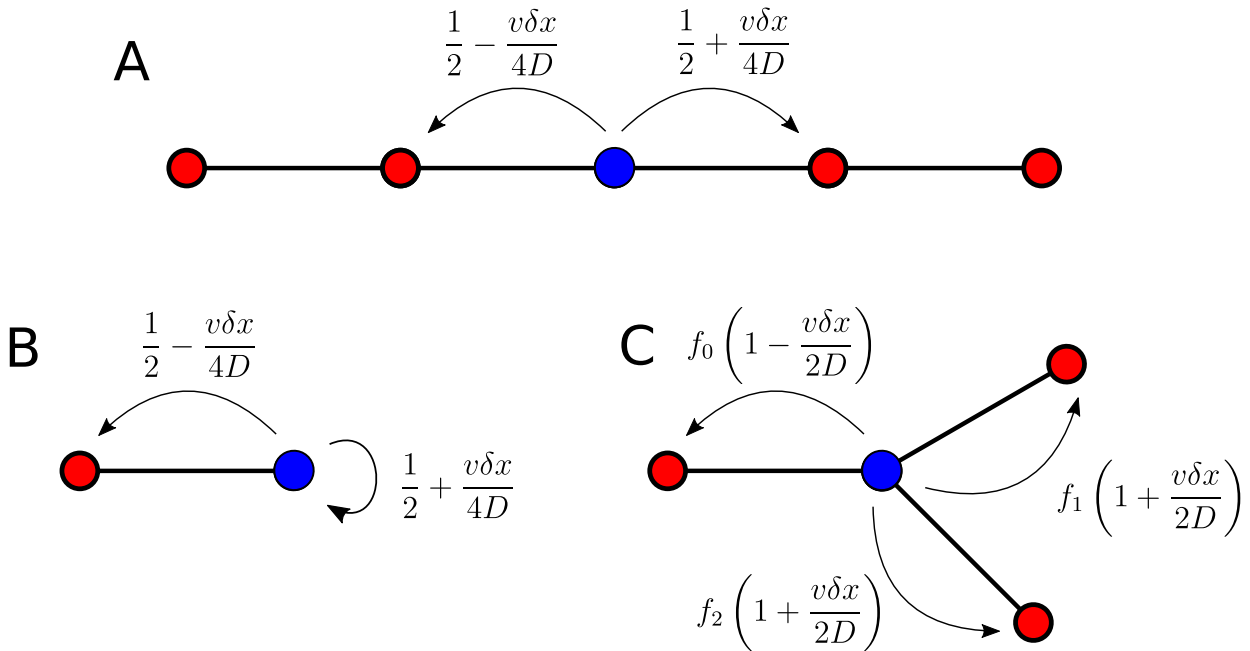
Figure 8: **_Discretization Schematization_** In this figure, I showed the fraction of protein moving toward the adjacent dendritic compartment in case of diffusion with active transport. In A), the case of a linear dendrite is shown; in B), a termination is shown; in C), a bifurcation is shown. In all these three subplots, the compartment more to the left is assumed to be the one closest to the soma. The values of f_0, f_1 and f_2, and how they are linked to the radii is discussed in Sec. 2.5.

and not with a partial differential equation. I solved many ODEs on a linear dendrite in the previous sections by imposing two appropriate boundary conditions. The effect of a branch in a dendritic tree is to link the three otherwise independent differential equations that describe the protein density in the mother and in the two daughter dendrites.

Once three dendrites are linked together, each of the three afferent dendrites loses one of its boundary condition: the no-flux boundary condition cannot be used anymore for the mother dendrite at $x = L$, and the incoming flux for the two daughter dendrites at $x = 0$ now depends on the whole system.

If I assume that both the daughter dendrites are terminal dendrites, which are not followed by any other daughter dendrites, I can retrieve the first two boundary conditions:

$$D \left. \frac{\partial \rho_{i=1,2}}{\partial x}(x) \right|_{L_{i=1,2}} = v\rho(x,t). \tag{57}$$

Then I imposed that the flux of proteins from the soma, $\Phi[0] = \beta = N\phi$, this flux to brings N proteins in the branch:

$$\sum_{i=1}^{3} \int_{0}^{L_i} \rho_i(x_i)\, dx_i = N. \tag{58}$$

The remaining three boundary conditions are related to the interplay between the three dendrites at the branch. The first boundary condition is obtained by making use of the continuity equation:

$$\sum \Phi_{in} = \sum \Phi_{out}, \tag{59}$$

namely, the total incoming flux of protein must be equal to the total outgoing flux of proteins, the continuity equation should also include a degradation term that takes into account the particles that are dismantled in the branch compartment, but in the limit of small branch size, that term can be set to zero.

In case of $v = 0$, the first new boundary condition become:

$$\left.\frac{\partial \rho_0}{\partial x}(x)\right|_{L_0} = \left.\frac{\partial \rho_1}{\partial x}(x)\right|_{0} + \left.\frac{\partial \rho_2}{\partial x}(x)\right|_{0}. \tag{60}$$

The other two boundary conditions can be determined by imposing what is the ratio of proteins at the branch:

$$\rho_1(0) = f_1 \rho_0(L_0) \tag{61}$$

$$\rho_2(0) = f_2 \rho_0(L_0). \tag{62}$$

In the case of multiple consecutive branches, I repeated this argument iteratively. Every branch added to a dendrite adds four new degrees of freedom, two for each daughter dendrite, and it removes the no-flux boundary conditions of the mother dendrite but introduces three boundary conditions for the branch and two for the no-flux boundary conditions of the daughter dendrites.

2.5.1   Diffusion on the Surface and in the Cytoplasm

If the movement is purely diffusive, and the diffusion length is much longer than the length of the dendrite, the surface and volumetric density of protein are constant, and therefore the number of proteins in either compartment is proportional to the available space in that compartment. The same is true if the diffusion length is not considerably longer than the dendrite length, but one focuses on a small segment of dendrite. For this reason, one can assume that the surface and volumetric density of proteins immediately before and after a branch is constant.

The immediate consequence of this is the fact that the total number of protein immediately before and after a branch is proportional to the available space in that compartment, which is equal to $S_i = 2\pi r_i \Delta x$, for surface proteins, like Nlg and ion channels, and $V_i = \pi r^2 \Delta x$ for cytoplasmic ones, like β-actin, GFP and Kamk2, and Δx is a short interval around the branch.

If the chosen interval Δx is small enough the density of protein per unit of space is constant and the ratio between the number of proteins in dendrite i and dendrite j is determined by the ratio between the $\gamma-$power of the radii, where $\gamma = 1$ in case of surface diffusion and $\gamma = 2$ in case of cytoplasmic diffusion:

$$f_i = \frac{R_i^\gamma}{R_2^\gamma + R_1^\gamma + R_2^\gamma} \tag{63}$$

Interestingly, Eq. 63, does not depend on the actual values of R_i and R_j, but only on their ratio. I, therefore, expressed the radii in terms of the radius of the mother dendrite:

$$R_i = r_i R_0; \tag{64}$$

where r_i is denoted as normalized radius. Therefore, I obtained the dependency of the last two boundary conditions on the dendrites' radii by plugging Eq. 63 into Eq. 62.

I show the complete analytical solution for a dendrite with a single branch in the Appendix, see Eq. 172.

In Sec. 2.1.1, I mentioned how the ER has a non-integer fractal dimension d_f. Therefore,

the available space on its surface scales as the d_f power of its radius, which is smaller than the radius of the dendrite. Assuming that the Radius of the ER in the dendrites is proportional to the radius of the dendrite itself, Eq. 63 still holds with $\gamma = 1.6$. The ER at the branch point would have properties that are intermediate between surface and cytoplasmic diffusion.

2.6   Brief Summary

In this section I calculated the protein profile for several transport models, obtaining the predicted protein profile for each of them. Here I modeled both passive diffusion and active transport. Using the work of Bressloff [1], I described active transport either as an increased diffusion coefficient, and as velocity term in the diffusion equation. In the case of the velocity term, I showed how for relatively small values of the velocity there is an accumulation of proteins at the dendritic tips.

Finally, I derived a rule for how to split the flux of proteins at a dendritic branch, discovering two qualitatively different rules for surface and cytoplasmic proteins.

3   Protein Requirement

A steady supply of proteins is necessary to maintain normal synaptic functions. For example, the number of AMPA receptors per synapse is estimated between 60 and 190, [66, 67, 68], considering the typical half-life of an AMPA receptor, in average, a new channel has to be substituted every 30 to 90 minutes. Under the assumption that the intake into synapses is proportional to the number of proteins in the dendrite, it is possible to use the protein profiles found in sec. 2, to calculate the minimum number of proteins that the neuron needs to produce to provide enough proteins to all synapses. The solutions of the diffusion equations are, due to its linearity, proportional to the production rate β, see Eq. 145, (in case of somatic translation and no active transport), Eq. 148 (in case of constant dendritic translation and no active transport), Eq. 151 (in case of mix of constant dendritic and somatic translation, and no active transport), Eq. 153 (in case of somatic translation and active transport), Eq. 155 (in case of in case of constant dendritic translation and active transport) and Eq. 162 (in case of dendritic translation induced by actively transported mRNA, and no active transport).

Therefore, given the minimum number of proteins per micrometer N_{min} that the dendrite needs, one can infer the production rate needed to supply the whole dendrite (or dendritic tree) with the corresponding model, obtaining the total amount of proteins that the neuron needs to produce. In the following, I referred to the number of proteins that the neuron needs to produce to provide at least $N_{min} = 1$ protein per micrometer, as *protein requirement*: N_{Req}.

Except for the two simplest cases, where the protein can only diffuse, or it is strictly decreasing with the distance from the soma, the analytical value of the protein requirement is not known. However, it can be obtained via numerical methods, by imposing the normalization $\int_0^L \rho(x) = 1$, and looking at the inverse of its minimum over the whole dendritic arbor:

$$N_{Req} = \frac{1}{\min_x(\rho(x))} \tag{65}$$

3.1   Protein Requirement: No Active Transport

If the protein can only diffuse, and all the mRNA are localized in the soma, the protein profile follows Eq. 35, and it is strictly decreasing. Therefore the protein requirement is given by the inverse of 35, evaluated at $x = L$:

$$N_{Req} = \lambda \sinh\left(\frac{L}{\lambda}\right). \tag{66}$$

If the translation happens with a constant rate throughout the dendrite, the protein density is constant, as I showed in Eq. 38. This means that the protein requirement is defined as the inverse of the protein profile in any of its point:

$$N_{Req} = \frac{1}{L}. \tag{67}$$

The behavior of these two cases is summarized in Fig. 9.

Because the protein requirement is defined as the inverse of the minimum density, the smaller the variability of the protein profile is, the smaller the protein requirement; among all the possible models, a constant translation is the one that minimizes the protein requirement for every dendritic morphology.

Because of this property the protein requirements in Figures 10, 11, and 12 are shown normalized to the protein requirement resulting from constant translation.

In the case of more complex protein densities, the value of the protein requirement is obtained numerically. To simplify the comparison of different models, in the following, I fixed the length of each dendrite to 200 μm and varied the other parameters.
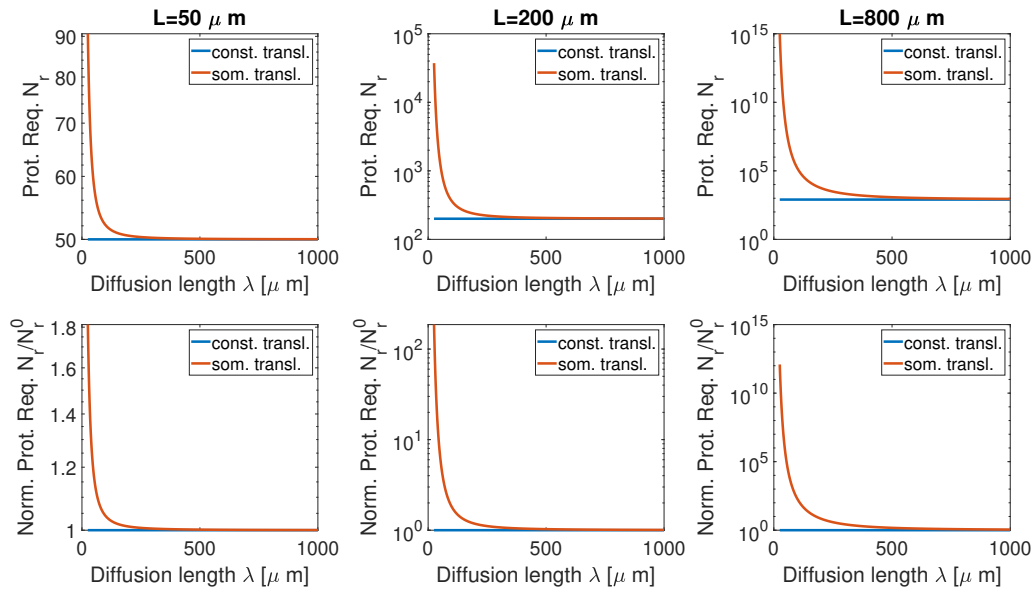
Figure 9: **Protein Requirement: Pure diffusion** In this figure I showed the dependency of the protein requirement N_r onto the diffusion length for a three fixed values of the length of the dendrite, from left to right $L = 50, 200,$ and $400 \mu m$. The same data are shown in the bottom row, normalized by the protein requirement in case of constant translation, $N_r^{(0)}$.

3.2   Protein Requirement: Active Transport and Somatic Translation

A more broad phenomenology appears when active transport is included, as seen in Fig. 6, blue: the slope of the protein density could be monotonically increasing if the effective velocity is high enough, monotonically decreasing if the velocity points toward the soma, be convex with a minimum between 0 and L. This minimum of the protein distribution inside the dendrite is a direct consequence of the boundary conditions.

Fig. 10 shows the protein requirement for different choices of the three parameters of the model. Unsurprisingly, when I increased the diffusion coefficient (see top row), the protein requirement decrease, meaning that the protein distribution became more homogeneous. The impact of the other two parameters, velocity, and half-life, is not equally straightforward. In the middle row, I showed the effect of velocity on the protein requirement, and I saw that the value at which N_{req} is minimized depends both on the half-life and on the diffusion coefficient. Velocities slower than the optimal velocity are not sufficient to move the distribution's peak away from the

beginning of the dendrite, while velocities faster than the optimal velocity accumulate protein at the end of the dendrite. In the bottom row, I showed the effect of the half-life upon N_{req}, noticing that for a high value of the velocity, when proteins would tend to accumulate at the end of the dendrite, a smaller value of the half-life could compensate the accumulation.

It is important to point out that minimizing the protein ratio by reducing the half-life of a protein could be a suboptimal strategy for the neuron because, as seen in Fig.10-G,H,I in yellow the value of the half-life that minimizes it is particularly small, and the neuron would need to produce that type of protein constantly.

3.3   Protein Requirement: Active Transport and Local Translation

In the previous section, I discussed how a constant translation in the dendritic arbor without active transport is the optimal strategy that the neuron could apply for proteins. Any increase in the velocity due to the active transport would move the system away from the global minimum of protein requirement.

Fig. 6 shows the slope of the protein density for different sets of parameters. Because of the symmetry of this system, a positive or negative velocity have the same impact on the protein requirement. In the case of negative velocity, the proximal dendrite would show an accumulation of proteins, while in the case of positive velocity, the accumulation would happen in distal dendrites. For this reason, in Fig. 10, I showed only the protein requirement for positive values of v.

When the velocity is different from zero, the value of the diffusion coefficient and of the half-life that minimizes the protein requirements are the ones that made the protein distribution as flat as possible. For this reason, the higher the diffusion coefficient, the more the system can counteract the effect of the active transport, and the lower is the protein requirement. Similarly, the shorter is the half-life of a protein, the less time it has to accumulate toward one of the extremities of the dendrite, resulting in a smaller protein requirement.
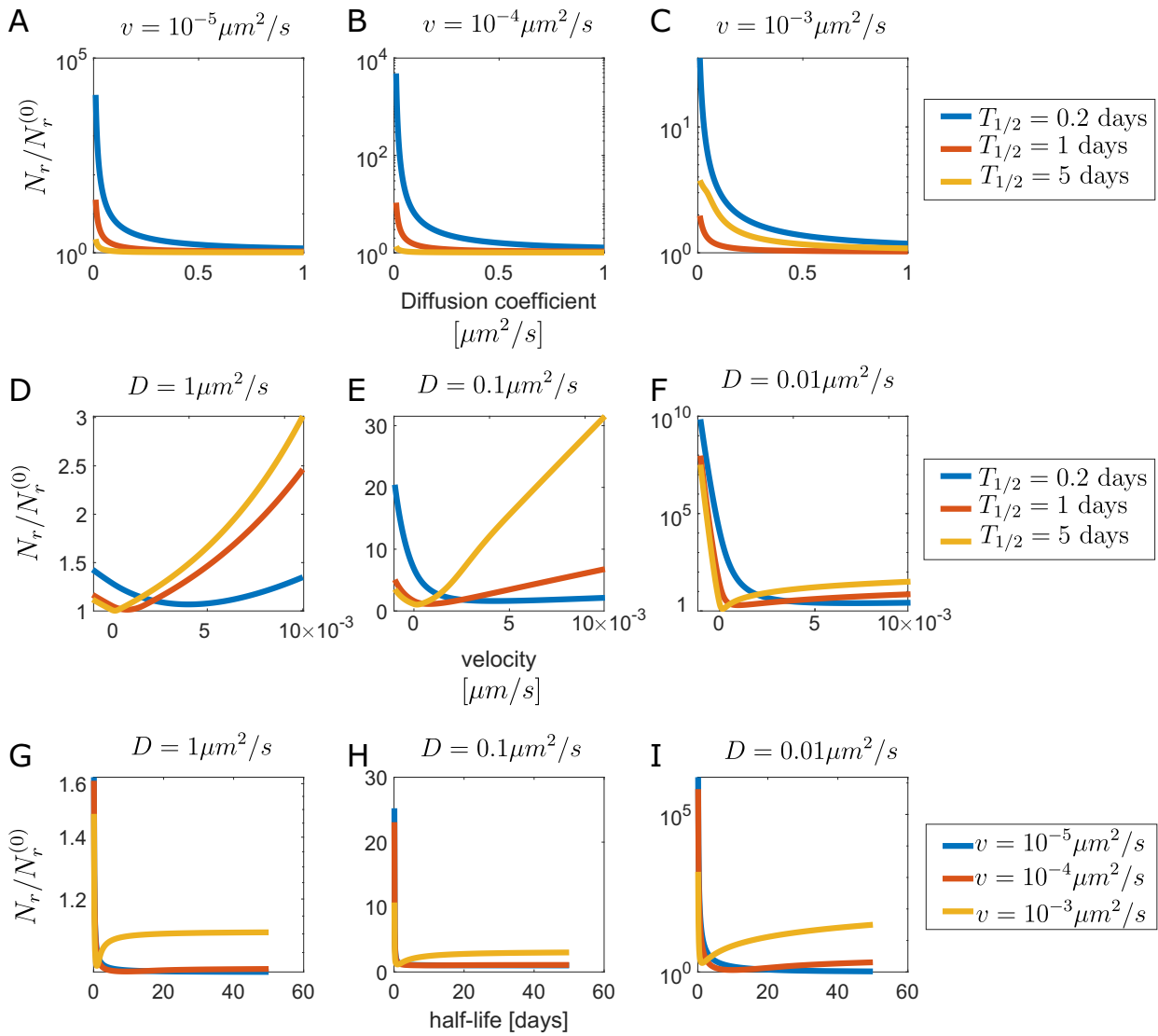
Figure 10: **Protein Requirement: Active Transport and Somatic Translation** This figure shows the ratio between the protein requirement of different choices of the diffusion length, half-life, and velocity, normalized by the minimal protein requirement possible. The length of the dendrite is fixed to $200\mu m$. In the top row, I varied the diffusion coefficient; in the second, I varied the velocity, and in the third, the half-life of the protein.

3.4   Protein Requirement: No Active Transport and Local Translation of actively transported mRNA

The previous section showed that a constant distribution of mRNA originates the model that requires the least overall amount of proteins. Therefore, it is intuitive that increasing the amount
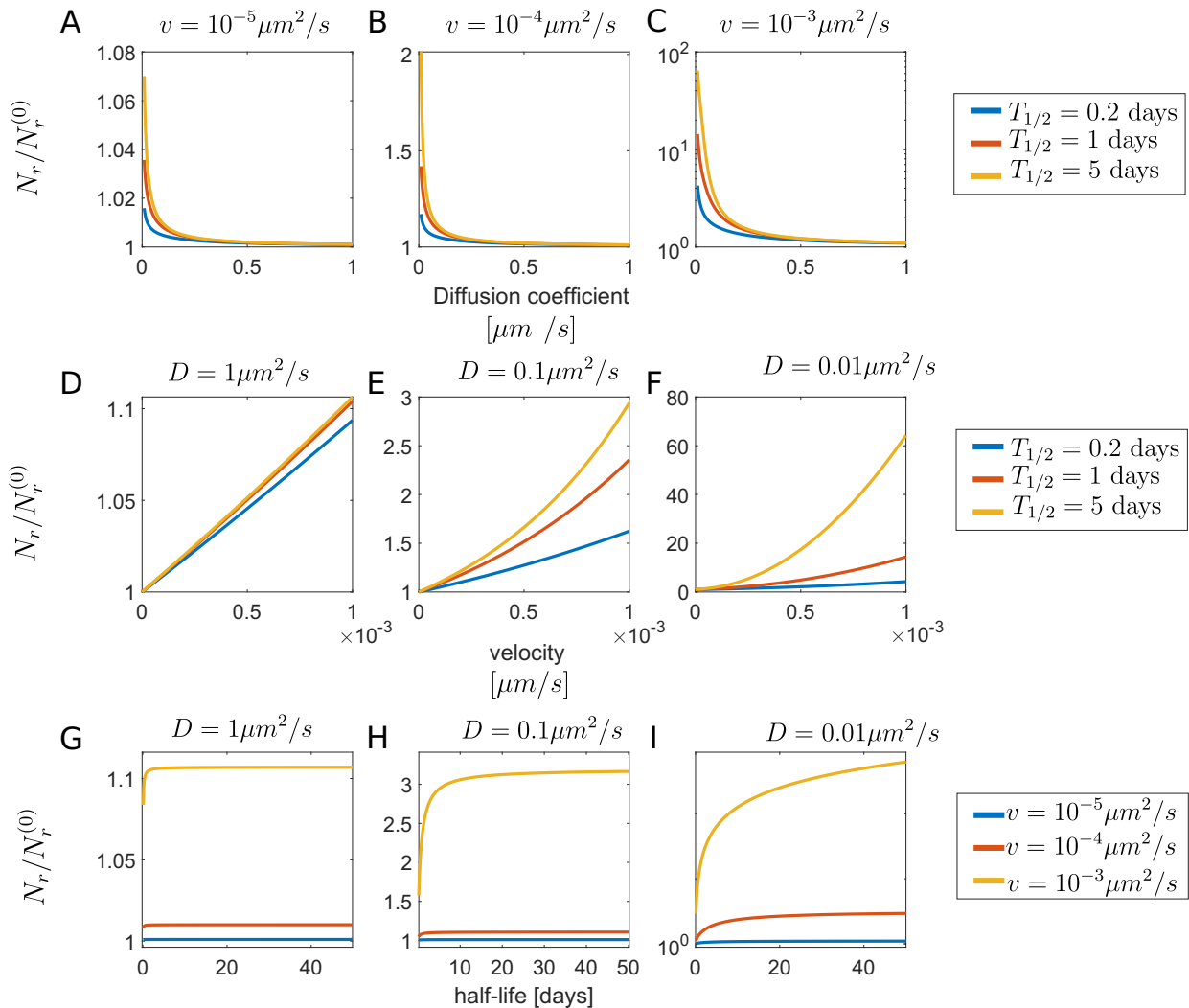
Figure 11: **Protein Requirement: Active Transport and Constant Dendritic Translation** This figure shows the ratio between the protein requirement of different choices of parameters normalized by the minimal protein requirement possible, obtained in the constant dendritic translation scenario. I fixed the length of the dendrite to 200*μm* and varied the other parameters. In the top row, I varied the diffusion coefficient; in the second, I varied the velocity, and in the third, the half-life of the protein.

of mRNA in dendrites would decrease the protein requirement closer to its minimum. Fig. 12 shows the normalized protein requirement for different choices of the diffusion coefficient, half-life, and velocity of the mRNA, for a protein with a reduced motility. The half-life and the diffusion coefficient of the protein are 5 days and 0.005 *μm²/s* respectively, leading to a diffusion length of 55.8 *μm*.
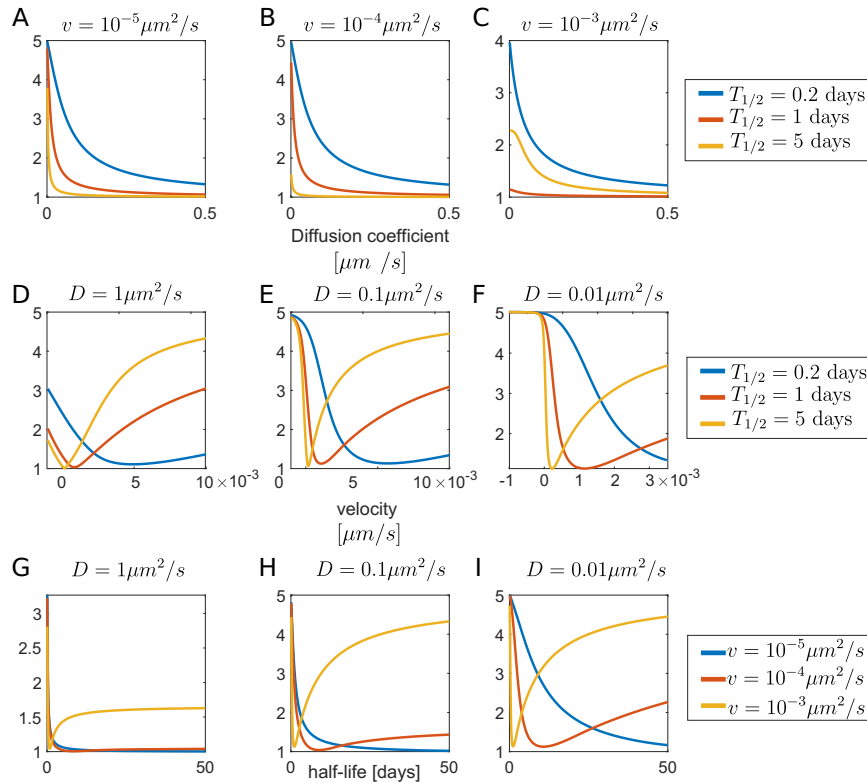
Figure 12: **Protein Requirement: Local Translation of actively transported mRNA** In this figure, I showed the ratio between the protein requirement of different choices of parameters divided by the minimal protein requirement possible, obtained in the constant dendritic translation scenario. I fixed the length of the dendrite to $200\mu m$ and varied the other parameters. In the top row, I varied the diffusion coefficient; in the second, I varied the velocity, and in the third, the half-life of the protein.

3.5   Protein Requirement: Single dendritic branch, purely diffusive proteins

In Sec. 2.5, I described a procedure to obtain the protein distribution in the case of purely diffusive proteins in a branching dendrite. Following the same argument I used for obtaining Eq. 66, because of the monotonically decreasing protein distribution in a dendritic branch, the protein requirement, N_{req} is equal to the inverse of the minimum of the protein density at the end of one of the two daughter dendrites:

$$N_{req} = \frac{1}{\min_{i=1,2} \rho_i (L_i)}, \tag{68}$$

where $\rho_i(L_i)$ are derived in 172. Exploring the full parameter space is rather complex, because of its high dimensionality, six parameters are needed for its full description: three for the length of the mother dendrite, L_0 and the two daughter dendrites L_1 and L_2, one for the diffusion length λ, and two for the fraction of proteins moving from the branch toward the daughter dendrites: f_1 and f_2. The fraction that is moving to the mother dendrite is determined by imposing $1 = f_0 + f_1 + f_2$. In Fig. 13, top I showed that the normalized protein requirement decreases when increasing the diffusion length, as happened with the single dendrite, without branches, while once the radius of one of the two dendrites is fixed, in the case of Fig. 13, bottom $R_1 = 0.5\,R_0$, there is a specific value of R_2 that minimize the protein requirement. I referred to that value of the radius as the *optimal radius*. Interestingly, The normalized protein requirement in Fig-13-A does not decrease to one with $\lambda \to \infty$. The reason is that the radius of the daughter dendrites is smaller than the radius of the mother dendrite. Therefore, in the limit of $\lambda \to \infty$, the surface, and the volumetric density became constant in the dendritic arbor, but the density of proteins in each dendritic compartment did not.

3.6   Brief Summary

In this section, I introduced the concept of protein requirement, defined as the number of proteins that a neuron needs to produce to bring at least one protein in each dendritic compartment. I then calculated the protein requirement for all the transport models described in Sec. 2. I showed that the model that minimizes the protein requirement is when the proteins are synthesized in the dendrite at a constant rate; this model solves the problem of transporting proteins but creating the problem of transporting mRNA.

Finally, I explored the protein requirement for dendrites with a single branch in the case of pure diffusion. I showed that there is a single value of the ratio of the daughter dendrites radii that minimize the protein requirement.
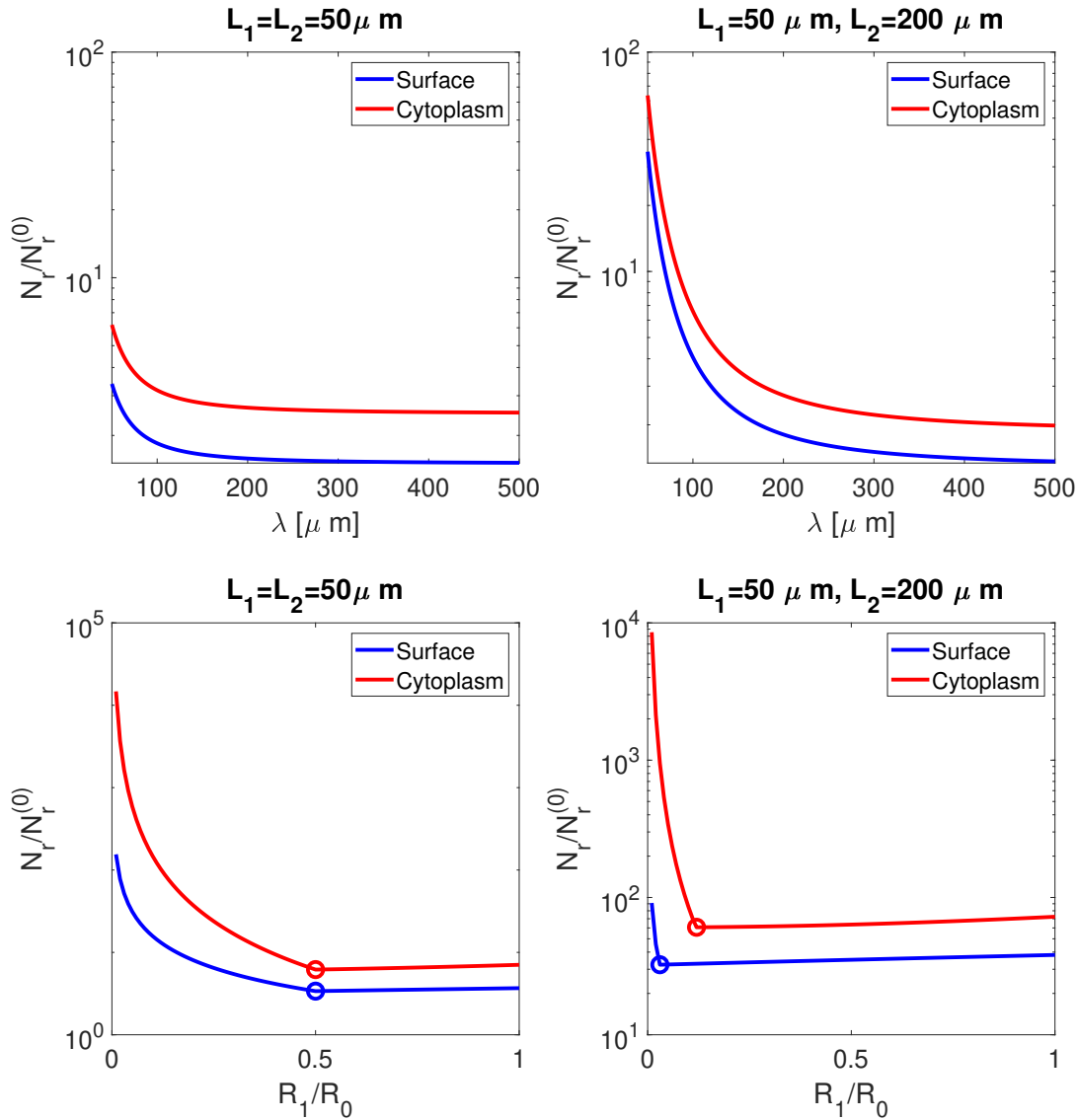
Figure 13: **Protein Requirement: Single Branch, Diffusive Proteins** A,B) The protein requirement, divided by the minimum protein requirement, where all the dendrites are provided with exactly 1 proteins per micrometer, is shown as a function of the diffusion length λ. In A) Both the length of the daughter dendrites are fixed to $50\mu m$, and the radii of the two daughter dendrites to $R_1 = R_2 = 0.5R_0$. In B) I imposed the same radii, but $L_2 = 200\mu m$; C,D) The normalized protein requirement is shown as a function of the normalized radius r_1, while r_2 is kept fixed at 0.5. In C) both the daughter dendrites have the same length, and the optimal radius r_1 is $r_1 = r_2 = 0.5$; in D) where the dendrite 2 is four times longer than dendrite 1, the optimal r_1 is smaller than r_2.

4   Optimal Branching Radii

In Fig.13-B, I observed that once the daughter radius of dendrite 1 is fixed to R_1, there is a single value of R_2 that minimize the Proteins Requirement, and I called that optimal radius. I showed that the optimal radius R_2^{opt} is not an intrinsic propertiy of the neuronal morphology, but it is also a function of the other radius, of the diffusion length λ, and of the dimensionality of the explored space, γ: $R_2^{opt} = R_2^{opt}(R_1, \gamma, L_1, L_2, \lambda)$.

4.1   Optimal Branching Radii

The fractions f_i, defined Eq. 63, represent the fraction of proteins that from the branch compartment flow toward the $i - th$ dendrite, and these are defined as the $\gamma-$power of the radius of the $i - th$ dendrite, divided by the sum of the γ-power of the radii of the three dendrites. Therefore, the neuron can tune how many proteins are diffusing in either direction simply by increasing or decreasing the radius of that dendrite.

The value of the optimal radius is obtained by equalizing the protein density at the termination of both daughter dendrites. By imposing $\rho_1(L_1) = \rho_2(L_2)$, in 172, and that f_1 and f_2 are defined by Eq. 63 I discovered that the Optimal Radius R_2 must satisfy the following equation:

$$\frac{\cosh(L_1/\lambda)}{\cosh(L_2/\lambda)} = \frac{R_1^\gamma}{R_2^\gamma}, \tag{69}$$

where $\gamma = 1$ for diffusion at the surface, and $\gamma = 2$ for diffusion in the cytoplasm. In Fig. 14-A one can see that for a fixed value of $L_2 = 50\mu m$ the optimal normalized radius, r_2, decreases if the length of the opposite dendrite is increased, in this way less protein would flow toward the dendrite 2, increasing the protein going to the dendrite 1; conversely, in Fig. 14-B I showed that the optimal normalized radius increases with the length of the its own dendrite.

In Fig. 14-C, D I observed for different choices of L_1 and L_2 that when the diffusion length grows, the optimal normalized radius r_2 tends to r_1; this is due to the distribution inside

each dendrite becoming increasingly flat, and therefore proportional to the fraction of proteins entering the dendrite: f_i. This is why in Fig. 13, the protein requirement never decreased to the optimal protein requirement, which could only happen for infinitely large values of λ, and $R_0 = R_1 = R_2$.

In Fig. 14-D,E I showed the dependency of the normalized optimal radius r_2, on the ratio between L_1/L_2, for two distinct values of λ. In Fig. 14-G,H I showed the logarithm of the optimal dendritic ratio r_1/r_2 varying both L_1/λ and L_2/λ, the colorcode is in logarithmic scale.

4.2   Optimal Consecutive Branches

In Sec. 4.1, I found the rule to obtain the optimal radii for every given diffusion length for a fixed value of the two dendritic daughter lengths. But Eq. 69 only works for terminal branches. An iterative procedure to assign an optimized normalized radius to each dendritic segment is needed for multiple consecutive branches. A protein traveling toward the tip of cortical pyramidal neurons can cross more than 20 consecutive branches before reaching the dendritic tip.

To optimize the radii of multiple consecutive branches, I followed an iterative algorithm that resembles the one described in [69]. The idea of the algorithm is that starting from the terminal branches, one collapses the mother dendrite and the two daughter dendrites into a single dendrite of effective length L_{eff} and radius equal to the radius of the mother. Doing so for each terminal branch, transform second-to-terminal branches into terminal branches, and the length of the two terminal branches is equal to the effective length of those branches. Proceeding by step:

1. for every terminal branches I calculated r_1 and r_2, as described in Sec. 4.1.

2. knowing (r_1, r_2, λ, L_0, L_1, L_2, and γ), I calculated L_{eff} using Eq. 71.

3. I considered the effective morphology where the three terminal dendrites are replaced by a single dendrite with effective lengths L_{eff};

4. repeat from point 1, until all the dendrites attached to the soma have no branches.

The whole procedure is schematized in Fig. 15.

4.2.1   Effective length

The idea that underlies finding the effective lengths is relatively simple. If the radii are optimized for a certain diffusion length, the density of proteins at both dendritic tips must be the same: $\rho_1(L_1) = \rho_2(L_2)$. I could therefore analyze the decay of the protein density from the begin of the mother dendrite $\rho_0(0)$ to the end of either daughter dendrites:

$$\text{DECAY} = \frac{\rho_0(0)}{\rho_1(L_1)}. \tag{70}$$

I can then wonder how long a dendrite should be to incur in the same decay; Using Eq. 70, and the solution for diffusive proteins with somatic translation, Eq. 145:

$$L_{\text{eff}} = \lambda \operatorname{arccosh}\left[\frac{\rho_0(0)}{\rho_1(L_1)}\right] \tag{71}$$

.

In Appendix, see Eq. 172, I found a closed solution for $\rho_i(x)$, that allows to find a numerical value for L_{eff}.

4.3 $3/2$- **Rall's Rule**

Rall's Rule, introduced by Wilfrid Rall [70, 71], explains how to collapse two daughter dendrites of the same length into a single dendrite with the same electrical conductance of the sum of the two collapsed ones. This allows determining the optimal branching radius to maximize the electrical signal collected at the soma coming from distal dendrites. In [69], the authors proved that the optimal tapering for dendrites is the quadratic tapering and described an algorithm that allows collapsing a dendritic tree with daughter dendrites of different lengths into an equivalent dendrite. The Rall's Rule sets a relation between the radius of the mother dendrite and the sum

of the radii of the two daughter dendrites:

$$R_0^{3/2} = R_1^{3/2} + R_2^{3/2}, \tag{72}$$

or in terms of normalized radii:

$$1 = r_1^{3/2} + r_2^{3/2}. \tag{73}$$

In the following, I referred to these equations as the 3/2-Rall's Rule. In Fig. 16-A the dependency of r_2 upon r_1 is shown. Recalling the definition of the f_i, in Eq. 63, and imposing the 3/2-Rall's Rule, I expressed the fraction of proteins moving toward the dendrite i-th only as a function of the normalized radius r_1. By doing so, I obtained the probability of moving toward dendrite i as a function of the radius of the dendrite 1:

$$f_i(r_1) = \frac{r_i^{\gamma}}{1 + r_1^{\gamma} + r_2^{\gamma}} = \frac{r_i^{\gamma}}{1 + r_1^{\gamma} + \left(1 - r_1^{3/2}\right)^{2\gamma/3}}. \tag{74}$$

As a consequence of Eq. 72, both the radii of the daughter dendrites must be smaller than the radius of the mother. The profile of f_0, f_1, and f_2 can be seen in Fig. 16-B,C,D. I also described the probability of diffusing away from the soma, namely $f_1 + f_2$, in Fig 16-E.

In Fig. 16- E, one can observe that the probability of surface proteins to move away from the soma is always higher than 1/2, while the probability of cytoplasmic proteins to move away from the soma is always smaller than 1/2. This is a direct consequence of the geometry of the system. For a 3/2- Rall exponent, the surface of two segments of the same length Δx after the branch is bigger than the surface of a segment of the same length before the branch

$$2\pi R_0 \Delta x \leq 2\pi (R_1 + R_2) \Delta x, \tag{75}$$

while the volume immediately after the branch is smaller than the volume in the same short

interval before the branch

$$\pi R_0^2 \Delta x \geq \pi \left(R_1^2 + R_2^2 \right) \Delta x. \tag{76}$$

4.4   Probability Ratio and Surface Bias

In Eq. 76, and 75 I showed that when the for a Rall exponent $\alpha = 3/2$, surface proteins are more likely to diffuse away from the soma at a branch, while cytoplasmic proteins are more likely to move toward the soma.

This properties can be quantified via the *probability ratio* defined as:

$$Q_P = \frac{R_1^\gamma + R_2^\gamma}{R_0^\gamma}. \tag{77}$$

The probability ratio represents the relative increase in protein after each branch. If $Q_P > 1$, the total number of proteins in the first compartment of the two daughter dendrites is higher than the number of proteins in the last compartment of the mother dendrite.

To compare the probability ratio of surface and cytoplasmic proteins I made use of the *surface bias* defined as:

$$Q_P^{S/C} = \frac{Q_P^S}{Q_P^C} - 1. \tag{78}$$

Recalling the assumption of cylindrical dendrites Eq. 78 can be simplified into:

$$Q^{S/C} = \frac{r_1 + r_2}{r_1^2 + r_2^2} - 1. \tag{79}$$

While the single values of the probability ratio Q^S and Q^C provides information relative to the bias toward distal dendrites compared to the mother dendrite, the surface bias represents the increase of the relative abundance of surface and cytoplasmic proteins immediately before and after the branch.

4.5   Generalized Rall Rule

For almost all real dendritic tree, the assumption of the 3/2 Rall exponent, is too restrictive. The 3/2 Rall exponent was introduced for mathematical simplicity, not in accordance to experimental data. In [72] Ascoli et al. reported the values of the Rall exponent in different classes of neurons:

- $\alpha = 2.36 \pm 1.2$ in Purkinje cells,

- $\alpha = 2.24 \pm 1.2$ in stellate neurons,

- $\alpha = 2.58 \pm 1.8$ in granule cells,

- $\alpha = 1.69 \pm 0.48$ in motoneurons,

- $\alpha = 2.28 \pm 0.89$ in basal pyramidal neuron,

- $\alpha = 1.69 \pm 0.48$ in apical pyramidal neurons.

To be able to describe a more broad range of possibilities, I changed the parameter 3/2 in Eq. 72, to a generic value α, as was done also in [2], doing so I obtained the *generalized Rall rule*:

$$R_0^\alpha = R_1^\alpha + R_2^\alpha, \tag{80}$$

or, as I did for the 3/2 case, I expressed it in terms of normalized radii:

$$1 = r_1^\alpha + r_2^\alpha. \tag{81}$$

If both the radii R_1 and R_2 are smaller than the mother dendrite, the value of the Rall exponent is positive: $\alpha \in (0, \infty)$ if they are both smaller than the mother dendrite $\alpha < 0$, and if one of the two is bigger than the mother dendrite, and the other smaller, Eq. 81 does not have a real solution for α.

I divided the values of α in categories, that leads to different behaviors: $\alpha < 0$, $0 < \alpha < 1$, $1 < \alpha < 2$, $\alpha > 2$, and $\alpha \notin \mathbb{R}$. See Fig. 18-A.

4.5.1 Rall Exponent $\alpha < 0$

A negative Rall exponent, to be consistent with Eq. 80, can be obtained if both the radii of the daughter dendrites are bigger than the mother dendrite.

In Fig. 17-A I showed the dependency of r_2 upon r_1. One can see that the radius of the second dendrite decreases by several orders of magnitude with a small variation of r_1; despite that, both daughter dendrites have a bigger radius of the mother dendrite, and therefore the available space at the surface and in the cytoplasm after the branch is higher than the available space before. In Fig. 17-B, C I showed the dependency of the probability of going back to the soma as a function of the radius of one of the two dendrites, and both for surface (blue) and cytoplasm proteins (red), this is smaller than $1/2$. Therefore,

$$0 \leq f_0^C \leq f_0^S \leq \frac{1}{2}; \tag{82}$$

and it can be shown that the probability ratio of cytoplasmic proteins is bigger than the probability ratio of surface proteins, 17-C, with:

$$2 < Q_S \leq Q_C. \tag{83}$$

This range of α corresponds to $r_1 \geq r_2 \geq 1$, white in Fig. 18-A;

4.5.2 Rall Exponent $0 < \alpha < 1$

A positive Rall exponent, to be consistent with Eq. 80, can be obtained only if both the radii of the daughter dendrites are smaller than the mother dendrite.

In Fig. 17-A I showed the dependency of r_2 upon r_1. One can observe that the radius of the second dendrite goes to zero very rapidly when r_1 goes to 1; its decrease is small enough to have both for surface and for cytoplasmic diffusion less available space after the branch than before.

The probabilities of going back to the soma, as shown in Fig. 17-E follow:

$$\frac{1}{2} \leq f_0^S \leq f_0^C \leq 1. \tag{84}$$

This range of α correspond to $r_2 < 1 - r_1$, darkest gray in Fig. 18-A.

4.5.3 Rall Exponent $1 < \alpha < 2$

The range $1 < \alpha < 2$, behaves similarly to the $3/2$-Rall's rule described in Sec. 4.3. For a fixed value of $\alpha = 3/2$, the dependency of r_2 upon r_1 is shown again in Fig. 17-G, the probability of moving backward to the soma in Fig. 17-H, and the probability ratio in 17-I. It is trivial to show that

$$1 - \sqrt{2} \leq f_0^S \leq \frac{1}{2} \leq f_0^C \leq \frac{2}{3}, \tag{85}$$

and that:

$$\frac{1}{2} \leq Q_P^C \leq 1 \leq Q_P^S \leq \sqrt{2}. \tag{86}$$

For these values of α, surface proteins are more likely to move away from the soma, while cytoplasmic proteins are more likely to move back to the soma. This range of α corresponds to $1 - r_1 < r_2 < \sqrt{1 - r_1^2}$, dark gray in Fig. 18-A;

4.5.4 Rall Exponent $\alpha > 2$

In the range $\alpha > 2$, the probability of moving back to the mother dendrites is smaller than $\frac{1}{2}$ both for surface and cytoplasmic diffusion:

$$\frac{1}{2} \geq f_0^C \geq f_0^S \geq \frac{1}{3}. \tag{87}$$

In the limit, $\alpha \to \infty$ the radii of one of the daughter dendrites tends to be equal to the radius of the mother dendrite. The dependency of r_2 upon r_1 is shown again in Fig. 17-G, the probability of

moving backward to the soma in Fig. 17-H, and the probability ratio in 17-I. It's trivial to show that

$$1 - \sqrt{2} \le f_0^S \le \frac{1}{2} \le f_0^C \le \frac{2}{3}, \tag{88}$$

and that:

$$\frac{1}{2} \le Q_P^C \le 1 \le Q_P^S \le \sqrt{2}. \tag{89}$$

In this range of α, both surface and cytoplasmic proteins are more likely to move away from the soma than toward it, but surface proteins are more likely than cytoplasmic proteins to do so.

This range of α corresponds to $r_2 > \sqrt{1 - r_1^2}$, gray in Fig. 18-A;

4.5.5   Rall Exponent $< \alpha \notin \mathbb{R}$

When one of the two daughter dendrites is bigger than the mother dendrite, and the other is smaller, no real value of α can be used to fulfill Eq. 80. In this scenario, if one of the two daughter dendrites is bigger than the mother dendrite,

$$0 \le f_0^X < \frac{1}{2}, \tag{90}$$

but nothing can be said about whether $f_0^S > f_0^C$ or $f_0^S < f_0^C$.

In this range of α, both surface and cytoplasmic proteins are more likely to move away from the soma than toward it, but nothing can be said about which of them is more likely to do so. This range of α corresponds to $r_1 > r_0 > r_2$, lightest gray in Fig. 18-A;

4.6   Brief Summary

In this Section, I introduced the probability ratio, defined as the ratio of the available space after the branch point divided by the available space before the branch point; because of Eq. 62, the probability ratio is also equal to the ratio of the proteins after the branch divided by the protein

before it. Fig. 18-B shows an overview of the lower and upper bounds on the probability of moving backward to the soma for $\alpha \in (-5,5)$.

In Fig. 17 I showed an overview of the values that the probability ratio can assume for four values of α, and in Fig. 18-C I showed the upper and lower bound that Q_P^S, and Q_P^C can have for $\alpha \in (-5,5)$; and in Fig. 18-D I did the same for the surface bias.
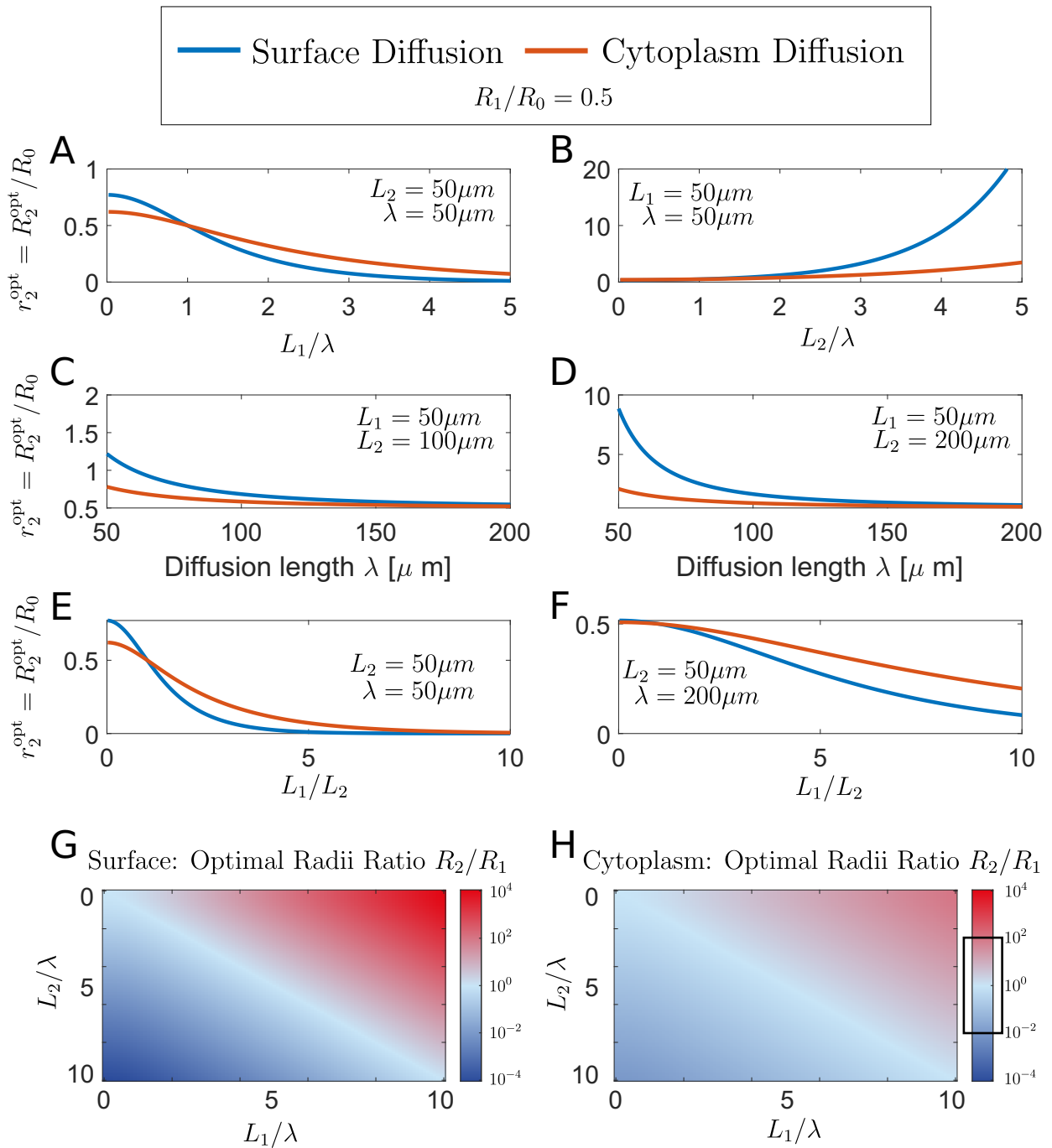
Figure 14: **Optimal Radii: Single Branch** In this Figure the dependency of the optimal normalized radius r_2 upon different parameters is explored. In A) the optimal normalized radius is plotted against the length of dendrite 1 divided by the diffusion length. λ is kept fixed to $\lambda = 50\mu m$ and $L_2 = 50\mu m$. B) The optimal normalized radius is plotted against the length of dendrite 2 divided by λ, with $L_1 = \lambda = 50\mu m$. C,D) The optimal normalized radius r_2 is plotted against the diffusion length λ. E,F) The Optimal normalized radius r_2 is plotted against the ratio of the dendritic lengths: L_1/L_2. G,H) The ratio of the optimal dendritic radii ratio $R_1^{optimal}/R_2$ is shown as function of the rescaled lengths of the daughter dendrites: L_i/λ. The colormap is in logarithmic scale.
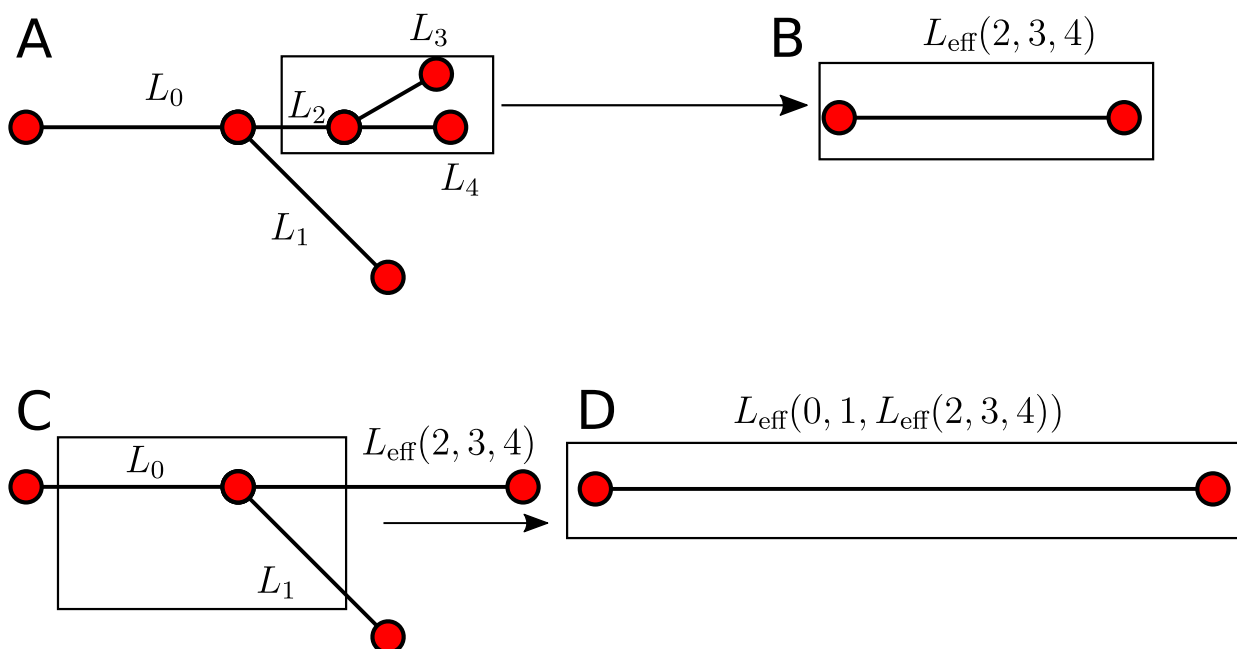
Figure 15: **Optimal Radii: Reduction Scheme** In this Figure I showed a schematization of the algorithm for reducing a dendritic tree to a single dendrite with equivalent length.
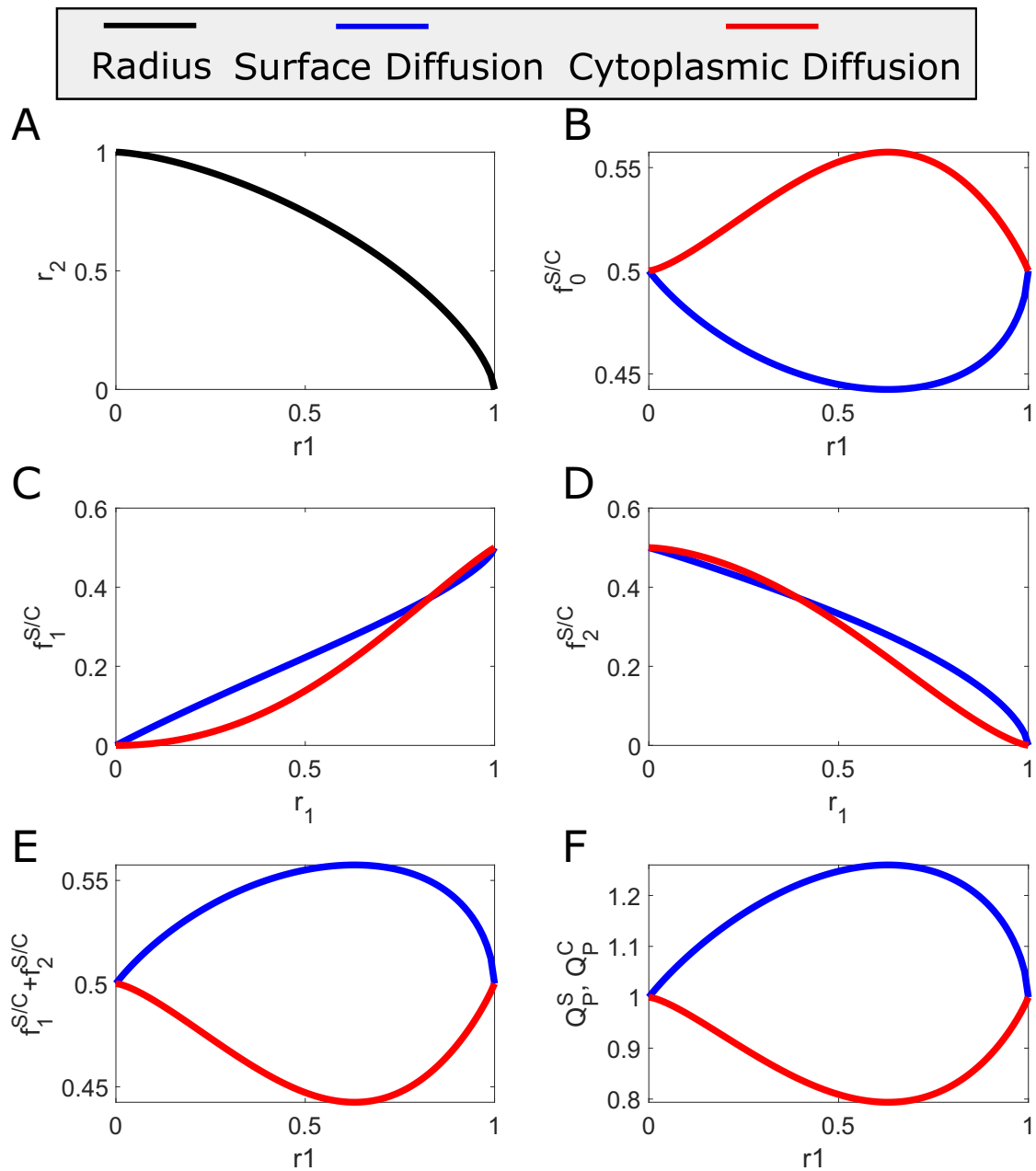
Figure 16: **3/2 Rall Rule** A) the dependency of r_2 on r_1 is shown. B) The probability of diffusing toward the mother dendrite, f_0 is shown as a function of the radius of one of the two daughter dendrites, r_1. C) The probability of diffusing toward the dendrite 1 is shown as a function of its normalized radius. D) The probability of diffusing toward the dendrite 2 is shown as a function of the normalized radius of the other dendrite. E) The probability of diffusing in one of the daughter dendrites is shown as a function of the radius of one of the two daughter dendrites. F) The probability ratio is defined as in Eq. 77 is shown as a function of one of the normalized radius of one of the two daughter dendrites. From B to F, blue lines represent the values in the case of diffusion on the surface, and red lines the values in diffusion in the cytoplasm.
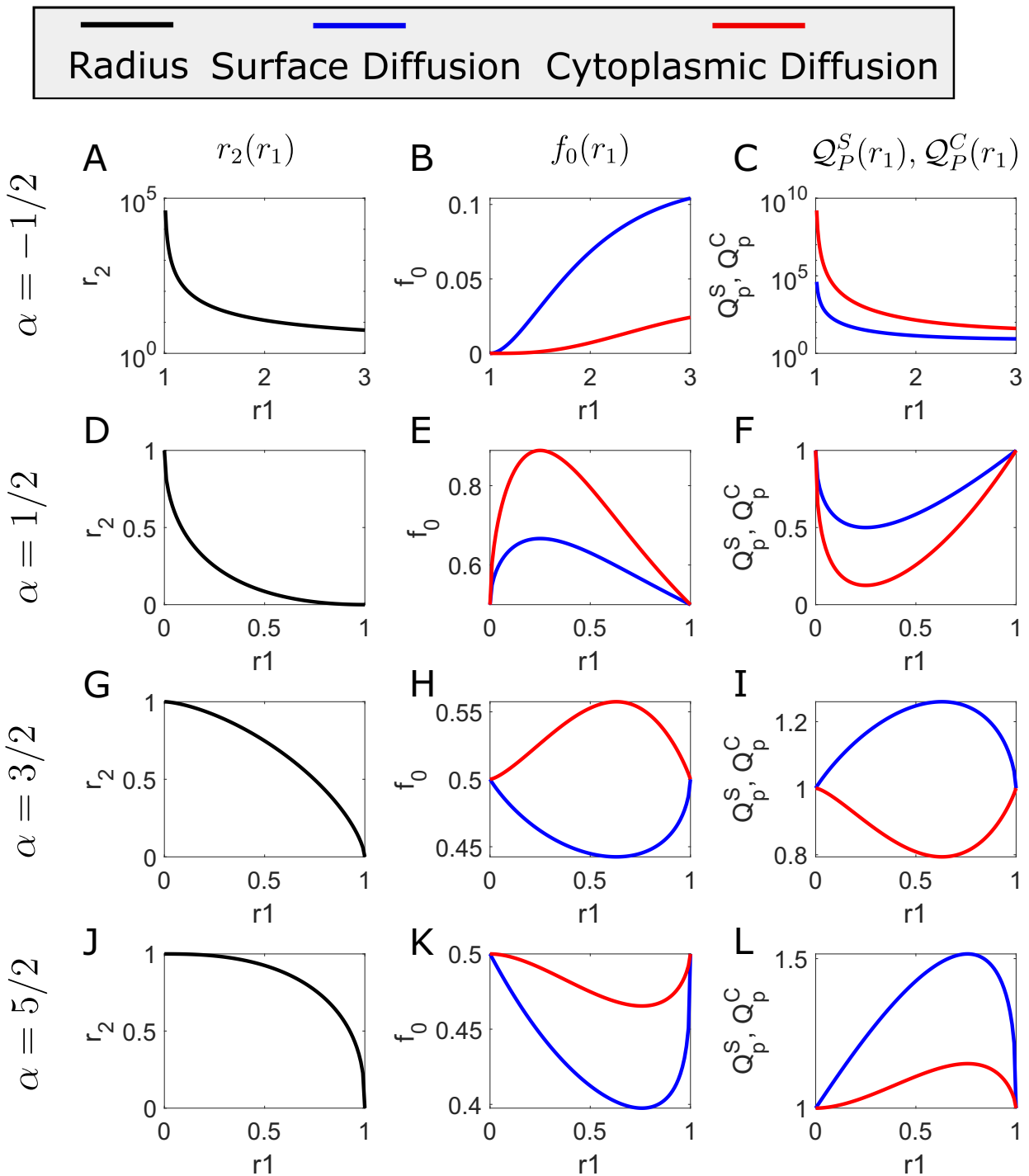
Figure 17: **Generalized Rall Rule** A generalization of what shown in Fig. 16 for $\alpha = 3/2$ is now shown for four different values of α: $\alpha = -\frac{1}{2}$ (first row), $\alpha = +\frac{1}{2}$ (second row), $\alpha = \frac{3}{2}$ (third row), $\alpha = \frac{5}{2}$ (forth row). In the left column, the dependency of r_2 upon r_1 is shown for different value of α. In the central column the probability of moving back toward the soma, f_0 is shown as function of r_1, both for surface proteins (blue) and cytoplasmic proteins (red). In right column the probability ratio Q_P is shown as function of r_1 both for surface protein (blue) and cytoplasmic protein (red).
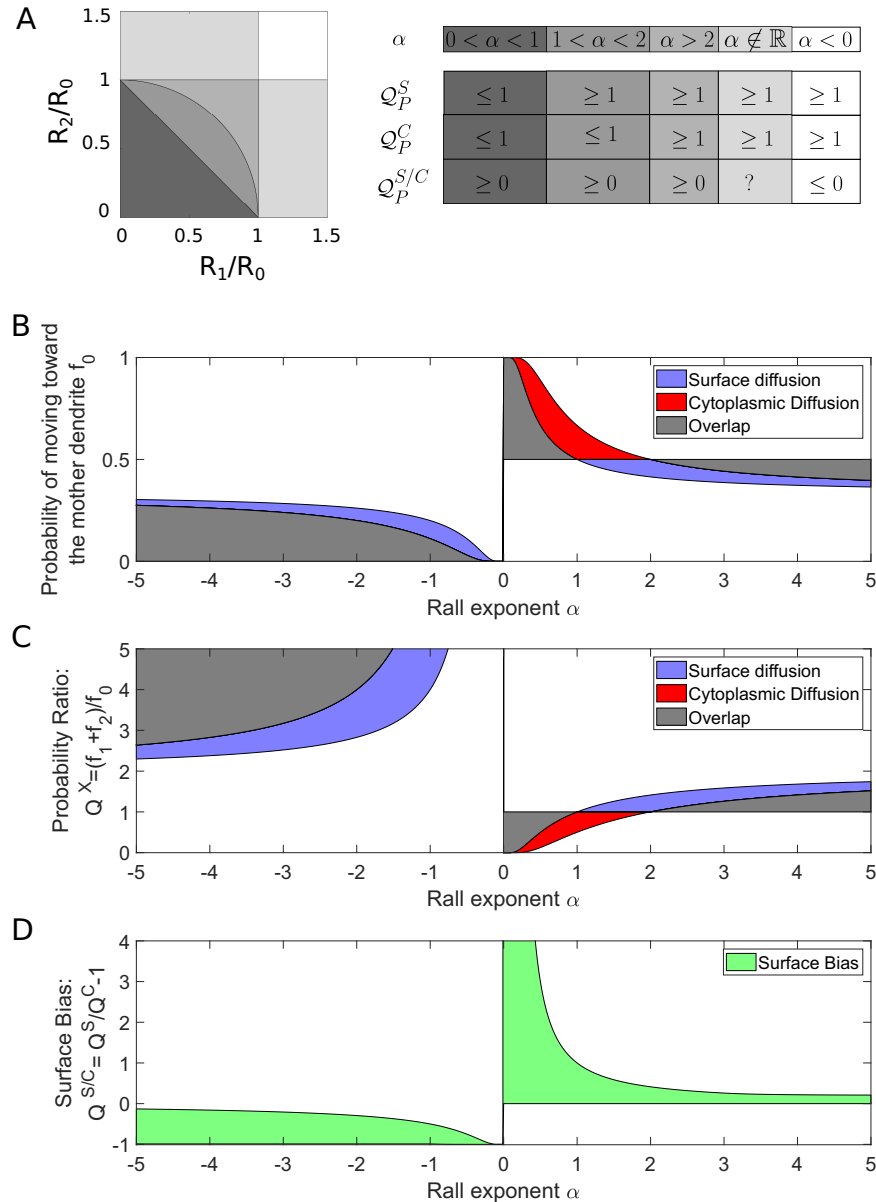
Figure 18: **Generalized Rall Rule: Overview** In A) The range of values that of the Rall exponent as a function of the two normalized radii, on the left a summary table of the probability ratios and surface bias. B) For every value of $\alpha \in (-5,5)$ I showed the upper and lower bound of the probability of moving toward the mother dendrite for surface proteins (blue) and for cytoplasmic ones (red), in gray the overlap between the two. C) for every value of $\alpha \in (-5,5)$ I showed the upper and lower bound of the probability ratio of surface proteins (blue) and for cytoplasmic ones (red), in gray the overlap between the two. D) for every value of $\alpha \in (-5,5)$ I showed the upper and lower bound of the probability ratio of surface bias (green).

5   Measured Branching Radii

In this section, I used data from three different datasets to calculate the Rall exponent, the probability ratio, and surface bias for the three classes of neurons: cultured rats hippocampal neurons, three-dimensional electron microscopy (3D-EM) reconstructed pyramidal neuron from mice's Prefrontal Cortical, and crab's stomatogastric ganglia neurons (STG).

5.1   Cultured Hippocampal Neurons

The first class of neurons I analyzed are cultured rat hippocampal neurons.

Our collaborator Anne-Sophie Hafner prepared two sets of dishes of cultured hippocampal neurons, following the procedure explained in Sec. F.1. The first set of these dishes contained neurons transfected with GFP, while the second set of neurons transfected with GFP::Nlg-1. The first is a soluble fluorescent protein, called Green Fluorescent Protein, and it is diffusing in the cytoplasm, the second a membrane-bound protein, called Neuroligin-1 associated to the same fluorescent protein, and it is diffusing on the neuronal surface.

For each of these neurons, I focused on clean branches. A clean branch is a branch composed of one mother dendrite and two daughter dendrites, with low background noise, where all three afferent dendrites do not present overlap with other dendrites or axons and do not have synaptic spines in the proximity of the branch, see 31

For each of these clean branches, the radius of the afferent dendrites was measured following the procedure described in Sec. F.4.

5.1.1   Radii Statistic

The first thing I analyzed is the Radii statistic for cultured neurons. In Fig 19-A I showed the full distribution of the 67 measured branches, from left to right of R_0, R_1 and R_2; Where I defined R_1 to be the bigger of the two daughter dendrites. The average radii are: $\mathbb{E}[R_0] = 0.84 \pm 0.32 \, \mu m$, $\mathbb{E}[R_1] = 0.69 \pm 0.25 \, \mu m$, and $\mathbb{E}[R_2] = 0.51 \pm 0.14 \, \mu m$. It is important to notice that this does not

represent the average radius of mother or daughter dendrites in cultured neurons because small dendrites were not considered due to the limited optical precision. For reference the range of measured radii spans from $R_{min} = 0.34 \mu m$ to $R_{min} = 1.95 \mu m$. The complete distribution of the normalized radii, pulling together all the daughter normalized radii, is shown in Fig 19-D.

5.1.2   Cultured Neurons: Rall Exponent

Knowing the normalized radii for both daughter dendrites, as shown in Fig 19-B, I calculated the value of of the Rall exponent of each branch, see Fig 19-C, and Fig 19-E for the full distribution of the Rall exponents.

The mean Rall exponent for the cultured neurons that I analyzed is $\mathbb{E}[\alpha] = 2 \pm 4$, but, because of the high variability, and asymmetry of the distribution, is more meaningful to use its median: $\mathbb{E}[\alpha] = 2.0$ (IQR: $1.5 - 2.9$).

5.1.3   Cultured Neurons: Probability Ratio

The other two quantities I calculated knowing the normalized radii are the probability ratio for surface and cytoplasmic proteins (see Fig. 19-F blue and red respectively). The mean probability ratio for surface proteins is $\mathbb{E}\left[Q_p^S\right] = 1.5 \pm 0.3$, its standard error of the mean is 0.03, and the median is $\mathbb{E}\left[Q_p^S\right] = 1.45$ (IQR: $1.27 - 1.65$).

The mean probability ratio for cytoplasmic proteins I measured are $\mathbb{E}\left[Q_p^C\right] = 1.17 \pm 0.43$, its standard error of the mean is 0.05, and the median is $\mathbb{E}\left[Q_p^C\right] = 1.12$ (IQR: $0.84 - 1.38$).

5.1.4   Cultured Neurons: Surface Bias

The last quantity I calculated starting from the normalized radii is the surface bias that represents the relative increase in the ratio of surface and cytoplasmic protein after and before each branch, see Fig. 19-G. The average surface bias is $\mathbb{E}\left[Q_p^{S/C}\right] = 0.31 \pm 0.16$, and the standard error is 0.1, while its median is $\mathbb{E}\left[Q_p^{S/C}\right] = 0.28$ (IQR: $0.20 - 0.46$).

	mean, std (s.e.m)	median (IQ1,IQ3)
Rall exponent α	2 ± 4 (0.27)	2.0 (1.5, 2.9)
Q_P^S	1.48 ± 0.28 (0.03)	1.45 (1.27, 1.65)
Q_P^C	1.17 ± 0.43 (0.05)	1.12 (0.84, 1.38)
$Q_P^{S/C}$	0.32 ± 0.18 (0.10)	0.28 (0.20, 0.46)

Table 2: **Cultured Neurons: Overview** In this table, I summarized the mean, standard deviation, standard error of the mean, median, and first and third interquartiles of the Rall exponent, the probability ratio of surface and cytoplasmic proteins surface bias.

5.2   STG Neurons: Stomatogastric Ganglia

The second dataset I analyzed is composed of 252 branches of crab stomatogastric ganglia neurons, or STG neurons, and was published in [2]. These neurons belong to four different subgroups, but I decided to analyze them together to make the results more readable. The STG neurons are located in the crab stomach; therefore, they are not affected by the same tight packing and spatial constraints of cortical neurons. This reflects into a much more disordered distribution of the radii, or to use the word that the authors used in the article's title where this data was published, "sloppy".

5.2.1   STG: Radii distribution

The first thing I analyzed is the radii statistic for crab's STG neurons published in [2]. in Fig 20-A I showed the full distribution of the 252 measured branches, from left to right of R_0, R_1 and R_2 where $R_1 > R_2$. The average Radii are: $\mathbb{E}[R_0] = 5.0 \pm 5.8 \mu m$, $\mathbb{E}[R_1] = 4.6 \pm 5.8 \mu m$, and $\mathbb{E}[R_2] = 1.8 \pm 2.5\ \mu m$. For reference the range of measured radii spans from $R_{min} = 0.05\ \mu m$ to $R_{min} = 41.6\ \mu m$. The complete distribution of the normalized radii, pulling together all the daughter normalized radii, is shown in Fig 20-D.
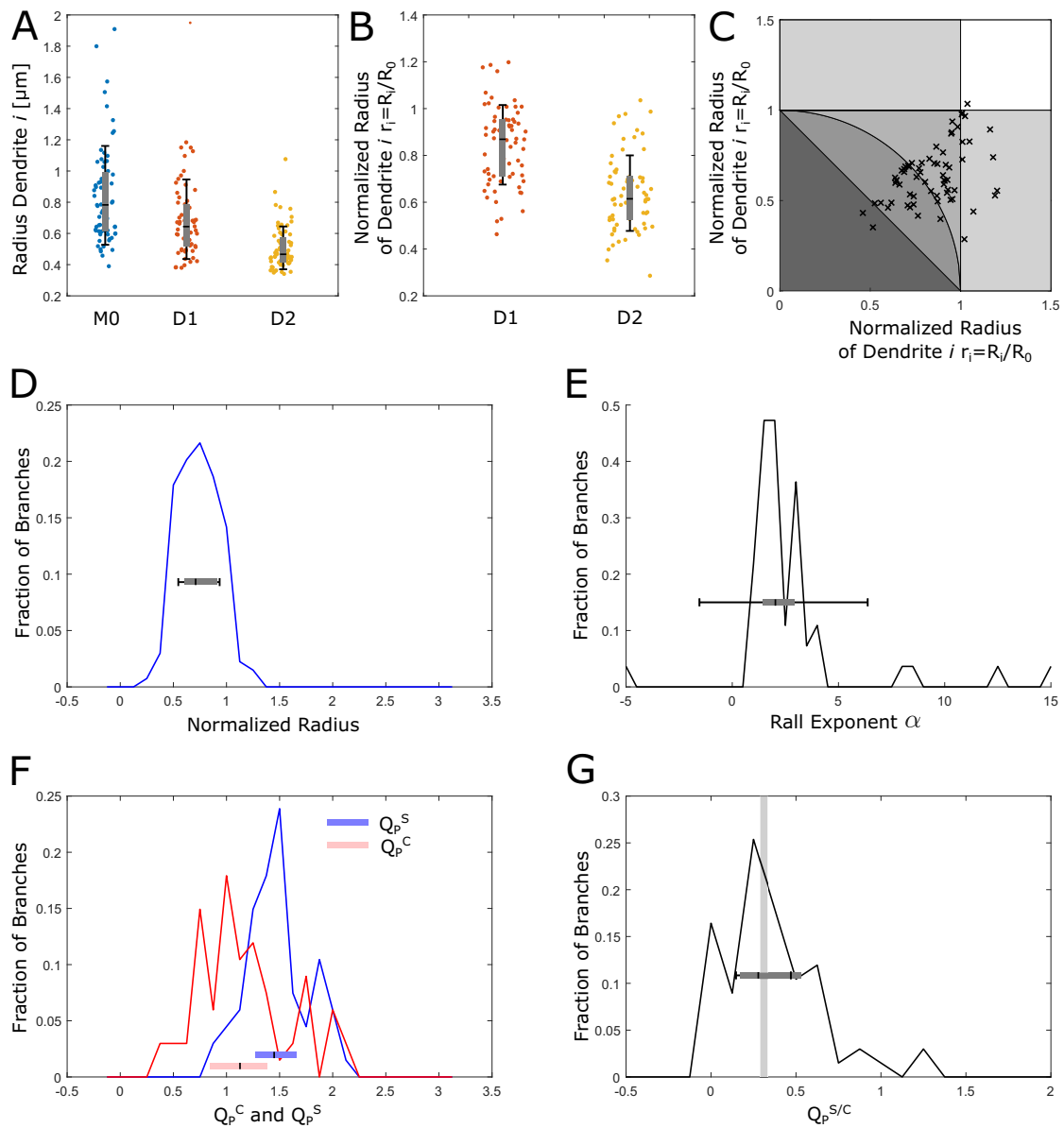
Figure 19: **Real Neurons Radii: Cultured Hippocampal Neurons** A) Scatterplot of all the measured radii, in order of the mother dendrite R_0, of the bigger daughter dendrite R_1, and of the smaller daughter dendrite R_2; B) Scatterplot of all the normalized radii, in order of the bigger daughter dendrite r_1 and of the smaller daughter dendrite r_2; C) Phase diagram of the radii distribution. The color code represents the range of values of alpha, as discussed in Sec. 4.6; D) Normalized radii distribution; E) Rall exponent distribution; F) Probability ratio distribution, in blue for surface proteins, in red for soluble proteins; G) Surface bias distribution. From A) to G), the black errorbars represent the mean and the standard error, while the rectangles the median, IQ1 and IQ2.

5.2.2   STG: Rall Exponent

Knowing the normalized radii for both daughter dendrites, see Fig 20-B, I calculated the value of

of the Rall exponent of each branch, see Fig 21-C, and Fig 20-E for the entire distribution of the

Rall exponents.

The mean Rall exponent for STG neurons that we measured is $\mathbb{E}[\alpha] = 0.88 \pm 2.27$, because

of the high variability, and asymmetry of the distribution, is more meaningful to observe its

median: $\mathbb{E}[\alpha] = 1.00$ (IQR: $0.72 - 1.47$).

5.2.3   STG: Probability Ratio and Surface Bias

The other two quantities I calculated knowing the normalized radii are the probability ratio for

surface and cytoplasmic proteins (see Fig. 20-F blue and red respectively. The mean probability

ratio for surface proteins is $\mathbb{E}[Q_p^S] = 1.58 \pm 2.00$, with s.e.m=0.12 and its median is: $\mathbb{E}[Q_p^S] =$

1.23 (IQR: $0.94 - 1.68$). The mean probability ratio for cytoplasmic proteins is $\mathbb{E}[Q_p^C] = 1.20 \pm$

0.41 with s.e.m.=2 and its median is: $\mathbb{E}[Q_p^C] = 0.93$ (IQR: $0.52 - 1.58$).

The last quantity I calculated is the Surface bias, see Fig. 20-G. The average surface bias is

$\mathbb{E}[Q_p^{S/C}] = 0.56 \pm 1.14$, with s.e.m=0.2 while its median is: $\mathbb{E}[Q_p^{S/C}] = 0.34$ (IQR: $0.23 - 0.78$).

	mean, std (s.e.m)	median (IQ1,IQ3)
Rall exponent α	0.88 ± 2.27 (0.17)	1.0 (0.72, 1.47)
Q_P^S	1.58 ± 2.00 (0.12)	1.23 (0.94, 1.68)
Q_P^C	5 ± 36 (2)	0.92 (0.52, 1.58)
$Q_P^{S/C}$	0.4 ± 0.4 (0.2)	0.34 (0.10, 0.67)

Table 3: **STG Neurons: Overview** In this table, I summarized the mean, standard deviation, standard error of the mean, median, and first and third interquartiles of the Rall exponent, the probability ratio both of surface and cytoplasmic proteins, and the surface bias.
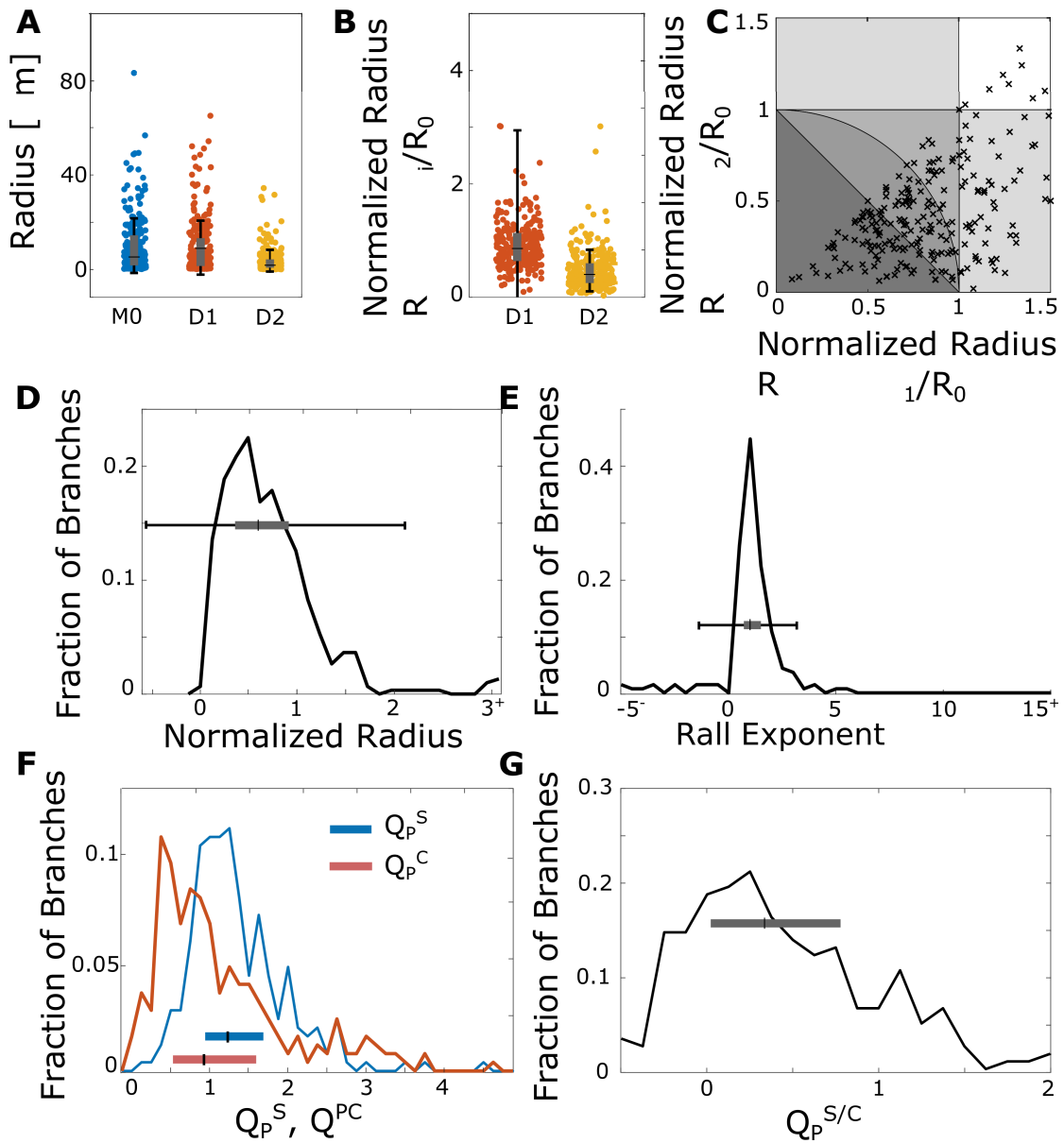
Figure 20: **Real Neurons Radii: Stomatogastric Ganglia Neurons** A) scatterplot of all the measured radii, in order of the mother dendrite R_0, of the bigger daughter dendrite R_1, and of the smaller daughter dendrite R_2; B) scatterplot of all the normalized radii, in order of the bigger daughter dendrite r_1 and of the smaller daughter dendrite r_2; C) phase diagram of the radii distribution. The color code represents the range of values of alpha, as discussed in Sec. 4.6; D) normalized radii distribution; E) Rall exponent distribution; F) probability ratio distribution, in blue for surface proteins, in red for soluble proteins; G) surface Bias distribution. From A) to G), the black error bars represent the mean and the standard error, while the rectangles the median, IQ1, and IQ2.

5.3   PPC Neurons: Cortical Pyramidal Neurons

The third dataset of neurons I analyzed contained 68 branches of pyramidal neurons in the prefrontal cortex. This dataset was provided to us by one of our collaborators, Ali Karimi; the dataset and the methodology used to obtain it was previously published in [73]. These branches were reconstructed using 3D electron microscopy, which allowed us to have very accurate information about the radii of each branch.

5.3.1   PPC: Radii Statistic

The first thing I analyzed is the Radii statistic. in Fig 21-A I showed the full distribution of the 68 measured branches, from left to right of R_0, R_1 and R_2 where $R_1 > R_2$. The average Radii are: $\mathbb{E}[R_0] = 0.61 \pm 0.20 \, \mu m$, $\mathbb{E}[R_1] = 0.52 \pm 0.20 \, \mu m$, and $\mathbb{E}[R_2] = 0.38 \pm 0.10 \, \mu m$. It's important to notice that this doesn't represent the average radius of mother or daughter dendrites in PPC pyramidal neurons, because our sampling was biased toward terminal dendrite. For reference the range of measured radii spans from $R_{min} = 0.119 \, \mu m$ and $R_{max} = 1.196 \, \mu m$.

The average radius of a normalized daughter radius is $\mathbb{E}[r] = 0.75 \pm 0.19$, and the standard error of the mean is 0.02, while the median of the normalized radii is: $\mathbb{E}[r] = 0.74$ (IQR: $0.63 - 0.87$) The complete distribution of the normalized radii, pulling together all the daughter normalized radii, is shown in Fig 21-D.

5.3.2   PPC: Rall Exponent

Knowing the normalized radii for both daughter dendrites, see Fig 21-B, I calculated the value of of the Rall exponent of each branch, see Fig 21-C, and Fig 21-E for the full distribution of the Rall exponents.

The mean Rall exponent for pyramidal neurons is $\mathbb{E}[\alpha] = 2.6 \pm 1.8$, with s.e.m.= 0.24, because of the high variability, and asymmetry of the distribution, is more meaningful to observe its median: $\mathbb{E}[\alpha] = 2.3$ (IQR: $1.8 - 3.3$).

This value is compatible with the one previously reported in literature, see [72]: $\alpha = 2.28 \pm$ 0.89 for basal dendrites, and $\alpha = 1.69 \pm 0.48$ for apical dendrites.

5.3.3   PPC: Probability Ratio and Surface Bias

The other two quantities I calculated are the probability ratio for surface and for cytoplasmic proteins, see Fig. 21-F blue and red respectively. The mean probability ratio for surface proteins is $\mathbb{E}[Q_p^S] = 1.50 \pm 0.26$, with s.e.m.=0.03, and its median is $\mathbb{E}[Q_p^S] = 1.5$ (IQR: $1.3 - 1.6$). The mean probability ratio for cytoplasmic proteins is $\mathbb{E}[Q_p^C] = 1.20 \pm 0.41$, with s.e.m.=0.04 and its median is $\mathbb{E}[Q_p^C] = 1.14$ (IQR: $0.95 - 1.37$).

The last quantity I calculate using the normalized radii is the surface bias, see Fig. 21-G. The average surface bias is $\mathbb{E}[Q_p^{S/C}] = 0.29 \pm 0.12$, with s.e.m.=0.07, while its median is $\mathbb{E}[Q_p^{S/C}] = 0.29$ (IQR: $0.20 - 0.38$).

	mean, std (s.e.m)	median (IQ1,IQ3)
Rall exponent α	2.56 ± 1.78 (0.24)	2.3 (1.8, 3.3)
Q_p^S	1.50 ± 0.26 (0.03)	1.49 (1.35, 1.65)
Q_p^C	1.20 ± 0.41 (0.05)	1.14 (0.95, 1.37)
$Q_p^{S/C}$	0.29 ± 0.12 (0.07)	0.29 (0.20, 0.38)

Table 4: **Pyramidal Neurons: Overview** In this table, I summarized the mean, standard deviation, standard error of the mean, median, and first and third interquartiles of the Rall exponent, the probability ratio of surface and cytoplasmic proteins, and the surface bias.

5.4   Brief Summary

In this section I analyzed three datasets of neurons to study their branching statistics. I applied the definition of Rall exponent, probability ratio, and surface bias derived in the previous sections, a summary of the median values of those quantities for the three types of neurons analyzed is shown in 5
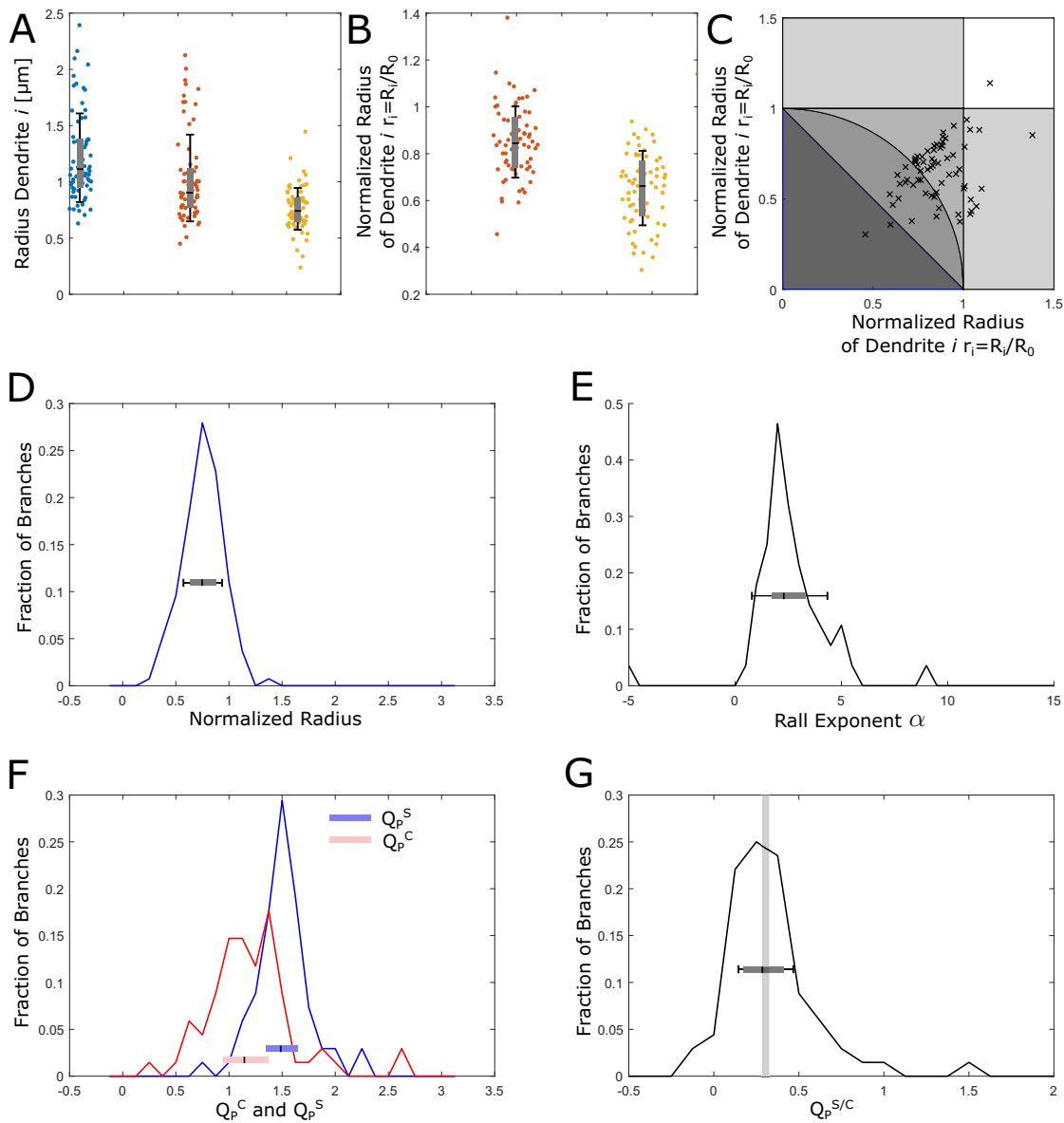
Figure 21: **Real Neurons Radii: PPC 3D-EM Reconstructed Pyramidal Neurons** A) Scatter-plot of all the measured radii, in order of the mother dendrite R_0, of the bigger daughter dendrite R_1, and of the smaller daughter dendrite R_2; B) Scatterplot of all the normalized radii, in order of the bigger daughter dendrite r_1 and of the smaller daughter dendrite r_2; C) Phase diagram of the radii distribution. The color code represents the range of values of alpha, as discussed in Sec. 4.6; D) Normalized radii distribution; E) Rall exponent distribution; F) Probability ratio distribution, in blue for surface proteins, in red for soluble proteins; G) surface bias distribution. From A) to G), the black error bars represent the mean and the standard error, while the rectangles the median, IQ1, and IQ2.

median (IQ1,IQ3)	Cultured	Pyramidal	STG
α	2.0 (1.5, 2.9)	2.3 (1.8, 3.3)	1.0 (0.72, 1.47)
Q_P^S	1.45 (1.27, 1.65)	1.49 (1.35, 1.65)	1.23 (0.94, 1.68)
Q_P^C	1.12 (0.84, 1.38)	1.14 (0.95, 1.37)	0.92 (0.52, 1.58)
$Q_P^{S/C}$	0.28 (0.20, 0.46)	0.29 (0.20, 0.38)	0.34 (0.10, 0.67)

Table 5: **Overview of the three classes of neurons analyzed,** for each of them I showed the median value and the interquartile range of: Rall exponent, probability ratio and surface bias.

6   Protein Fluorescence in Cultured Neurons

In this chapter I analyzed the fluorescence of two diffusive proteins, one is a fluorescent soluble proteins called GFP, and the other is a surface protein GFP::Nlg, a surface protein associated with GFP. Analyzing the intensity of the fluorescence I calculated the ratio of proteins before and after the branch, and I compared those fractions with the fraction predicted by the radii statistics of cultured neurons derived in Sec. 5.

Our collaborator, Anne-Sophie Hafner, imaged 22 individual neurons, half of which were transfected with GFP, Green Fluorescence protein and half with GFP::Nlg, Neuroligin associated with GFP, the first is a cytoplasmic fluorescent protein, and the second a surface protein associated with a surface protein. Having two populations of neurons transfected with proteins of two different species allowed me to compare the fluorescence intensity before and after each branch.

Using FIJI, an open software that allows measuring the luminosity of each recorded voxel, I analyzed the sum of the projected intensities on the X-Y plane, see Fig. 22-A. Once the three-dimensional image was reduced to a bi-dimensional one, I identified all the *clean* branches and selected a narrow area around them. I referred to this area as the *region of interest* or RoI. The RoI was selected to be as close as possible to the edges of the dendrite to minimize the effect of the background noise but big enough to include all the fluorescent signal of the dendrite. The definition of *clean* branch and a detailed description of how I selected the branches are in Appendix, see Sec. F.3. Measuring the fluorescence in FIJI allowed me to express it as a function of the distance from the beginning of the *region of interest*. As a convention, all the RoI were oriented such that $x = 0$ was the closest point to the soma. The signal $f_i(x)$ that I obtained was then integrated over the interval $x \in (m, m + \Delta)$:

$$F_i(m, \Delta) = \int_m^{m+\Delta} f(x)dx. \tag{91}$$

For a schematization, see Fig. 22-B.

Following the assumption that the fluorescence of a protein is proportional to the abundance

of the protein itself, $F_i = KN_i$; limiting the analysis to a narrow interval around the branch, I assumed that the proportionality constant K is the same in the three connected dendrites.

In Fig 22-C and D, I showed the individual values of the point-wise fluorescence ratio defined as:

$$f(x) = \frac{f_1(x) + f_2(x)}{f_0(x)}. \tag{92}$$

The error bars represent the mean and standard deviation of the point-wise fluorescence ratio for each of the branches. The main limitation of this approach is the high fluctuation of the point-wise fluorescence ratio. To limit them, I decided to consider the integrated fluorescent ratio, defined as

$$Q_F^X(m,\Delta) = \frac{F_1(m,\Delta) + F_2(m,\Delta)}{F_0(m,\Delta)}. \tag{93}$$

Both Eq. 93, and Eq. 77, quantify the expected ratio of protein after and before the branch. The first uses the intensity of the fluorescence of the protein to calculate that ratio, and the second the radii of the dendrites.

In Fig. 22-E, I showed the integrated fluorescence ratio for different choices of m and Δ. The error bars show the mean and the standard error of the mean for each set of m and Δ. The shaded area is the expected mean and standard error of the mean of the probability ratio, as obtained in Sec. 5.1.3. The high value of the fluorescence ratio for Nlg protein and $m = 1, \Delta = 1$ is due to two outlier in the fluorescence of two of the daughter dendrites; due to the small integration interval, their impact is easily noticeable. The reason that the standard error of the mean increases with $m + \Delta$, is due to the fact that Eq. 93 can be applied only to branches with $\min(L_0, L_1, L_2) > m + \Delta$. The complete distribution of the Fluorescence ratio for different choices of m and Δ, is shown in Appendix, see Fig. 32.

In Fig. 22-F, I showed the mean and the standard error of the mean of the fluorescence

surface bias, defined, analogously to the surface bias in Eq. 78:

$$Q_F^{S/C} = \frac{Q_F^S}{Q_F^C} - 1. \tag{94}$$

The fluorescent surface bias cannot be calculated directly from the fluorescent signals of the two proteins, for this reason, for each value of m and Δ, I defined it as:

$$Q_F^{S/C}(m, \Delta) = \frac{Q_F^S(m, \Delta)}{Q_F^C(m, \Delta)} - 1. \tag{95}$$

6.1   Summary of Protein Fluorescence

As I predicted, both the measured probability ratio and fluorescence ratio are in good agreement, see Table 6, the same is true also for the surface bias and fluorescence surface bias.

	mean $\pm$ std, S.E.M.	median, (1st - 3rd IQ)
Q_F^S	$1.57 \pm 1.17, /$	$1.32\,(1.08 - 1.71)$
Q_P^S	$1.48 \pm 0.28, (0.03)$	$1.45\,(1.27 - 1.65)$
Q_F^C	$1.24 \pm 0.45, /$	$1.16\,(0.981 - 1.41)$
Q_P^C	$1.17 \pm 0.45, (0.05)$	$1.12\,(0.84 - 1.37)$
$Q_F^{S/C}$	$0.22 \pm 0.65, /$	$0.24\,(0.17 - 0.26)$
$Q_P^{S/C}$	$0.36 \pm 0.28, (0.03)$	$0.28\,(0.17 - 0.53)$

Table 6: **Overview of the fluorescence ratio and of the probability ratio** for surface (S) and cytoplasmic (C) proteins. And also of the fluorescence surface bias. For each quantity the mean, standard deviation, median and first to third interquartile (IQ) range are specified. For the values obtained from the radii, I calculated also the standard error of the mean, s.e.m.
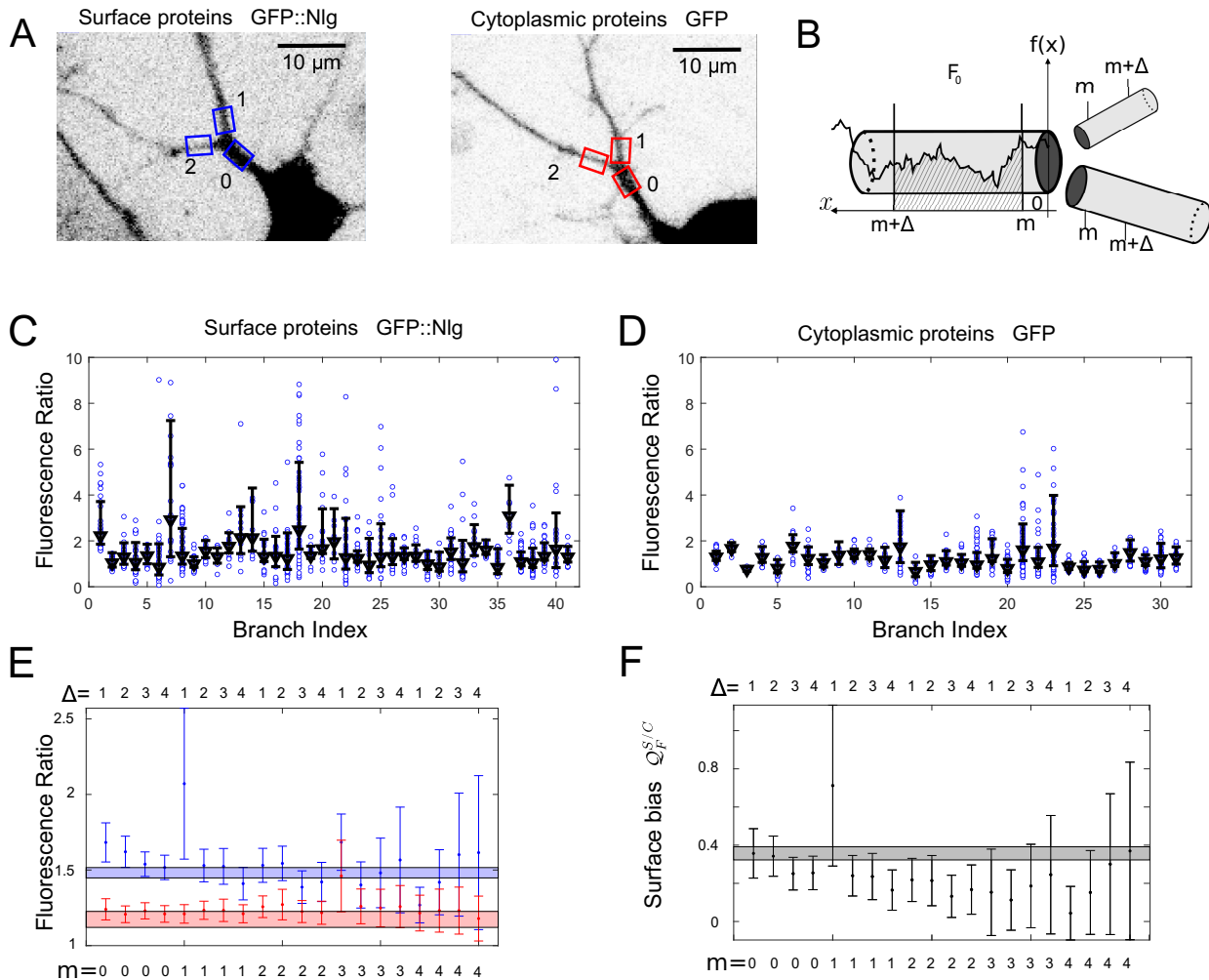
Figure 22: **Fluorescence of Cultured Hippocampal Neurons** A) In this figure, I showed two examples of cultured neurons, one for a surface protein: GFP::Nlg, and one for a cytoplasmic protein: GFP. B) The schematization on how the fluorescent signal is extracted from an image, integrating it from a distance m to a distance $m+\Delta$ from the soma. C,D) mean and standard deviation of the fluorescence ratio for each of the branches. The individual dots are the fluorescence ratio of the signal at distance d from the branch: $\frac{f_1(d)+f_2(d)}{f_0(d)}$, and the errorbar is the average over d, and the standard deviation. E) mean integrated fluorescence ratio and standard error of the mean for different values of m and Δ. G) mean integrated surface bias and its standard error of the mean for different values of m and Δ. Subplots A), B) are adapted from [7].

7   Optimal Branching In Real Morphologies

In this section, I analyzed the relationship between the radii of 28 pyramidal branches with the length of their daughter dendrites. I inverted the equation found in Sec. 4 to associate to every branch the type of protein whose diffusion is optimized by the branch itself. Then, I compared the distribution of the diffusion length of those proteins, with the diffusion lengths of real proteins and I calculated the cost for deviating from those optimal diffusion lengths.

Our collaborator, Ali Karimi, provided us with 68 branches of cortical pyramidal neuron data. In Sec. 5.3 I analyzed the statistics of their radii. 28 of those 78 branches were terminal, and that allowed me to invert Eq. 69 and obtain the *optimized diffusion length* for each branch. Then I compared the distribution of optimized λ with the distribution of the diffusion length of 26 proteins finding that the peaks of the two distributions overlap. Furthermore, the distribution of the diffusion lengths of real proteins is higher than the distribution of the optimized diffusion lengths, both for surface and cytoplasmic proteins. Therefore, I analyzed the cost for a protein not to have the optimized diffusion length, and I found that, in average, the percentage cost, in terms of how many extra proteins each branch needs to produce grows faster for smaller diffusion lengths than for higher ones.

7.1   Optimized Diffusion Length

The 28 terminal branches are the only ones where the argument used to obtain Eq. 69 can be applied. This is because the no-flux condition must be imposed on both daughter dendrite termi-nation to obtain Eq. 69, and it can be applied only to terminal branches. The dependency of L_2 on L_1 is shown in Fig. 23-A.

In the following, I assumeed that $L_1 \geq L_2$. If $R_1 > R_2$ I obtained, numerically, the value of λ that solves Eq. 69, and I called it *optimized diffusion length*. In 9 of the 28 branches, the longer dendrite is associated with the smaller radius, so there is no real value of λ that satisfies Eq. 69. In these cases, I defined the optimized diffusion length as the value of the diffusion length

that minimizes the protein requirement for the branch. In Fig. 23-B, I plotted the dependency of the protein requirement on the diffusion length for all these irregular branches, showing that the protein requirement decreases monotonically with λ; the optimized diffusion length of these irregular branches is, therefore, $\lambda = \infty$.

In Fig. 23-C, I showed the distribution of the optimized diffusion length for surface and cytoplasmic proteins, in blue and red, respectively. Restricting the analysis only to the finite values of λ, the median values of the optimized λ are 109 μm for surface proteins and 65 μm for cytoplasmic proteins.

For each branch, the optimized diffusion length for diffusion at the surface is higher than the optimized diffusion length for diffusion in the cytoplasm because of the power γ in Eq. 69.

7.2 Real diffusion lengths

From Eq. 69, I obtained the distribution of the optimized diffusion lengths; here, I wanted to compare such distributions with the distribution of the diffusion lengths of real proteins. To obtain the diffusion length of a real protein, I needed two parameters: the half-life and the diffusion coefficient. I took the majority of the value of the half-life from [8], and I searched in the literature for the diffusion coefficients. The principal techniques used to measure the diffusion coefficients of dendritic proteins are FRAP, fluorescence recovery after photobleaching, FCS fluorescence correlation spectroscopy, and SPT, single particle tracking. For an explanation of these techniques, see Appendix, Sec. G.4, Sec. G.3, and G.2 respectively.

The distribution of the diffusion length of real proteins is shown in 23-C, yellow, and the median of that distribution is $\lambda = 329 \ \mu m$. For the complete list of the diffusion lengths of dendritic proteins, see Table 11 in Appendix.

7.3   Costs for deviating from optimality

Each branch is optimizing for a different value of the diffusion length, and the distribution spans across multiple order of magnitude; the same is true for the diffusion length of real proteins. The question that arises naturally is how high is the cost the system has to pay for not following Eq. 69? First, I used the information about the lengths of the dendrite, and check the cost for a percentage deviation from the optimal radii, then I used both the information about the lengths of the daughter dendrites and the radii of the daughter dendrites, and I calculated the percentage increase in the protein requirement as a function of λ.

7.3.1   Cost For Non-optimal Radii

The first thing I checked was the extra percentage cost for non-optimal radii. I fixed the length of the daughter dendrites to their measured value, and the value of $\lambda = 329 \, \mu m$, the median from the protein distribution, and the value of one of the normalized radii $r_2 = 0.74$.

Fig. 23-D shows that the protein requirement increases more rapidly when one of the two radii is smaller than its optimal value than when it is bigger. This is easily understandable from Eq. 63: decreasing r_1 affects the protein requirement of dendrite 1 while when the radius of the dendrite 1 is increased, the other two dendrites would contribute together to compensate for the increased demand.

The protein requirement for $r_1 = r_1^{optimal} + 50\% = 1.5 \, r_1^{optimal}$ is 2-8 times smaller than $r_1 = r_1^{optimal} - 50\%$ for surface protein and 3-90 times smaller for cytoplasmic proteins. Furthermore, the same deviation, in percentage, from the optimal radius implies a much higher extra cost in cytoplasmic diffusion than in the case of surface diffusion.

7.3.2   Cost For Non-optimal diffusion length

In Fig. 23-E, I checked the extra percentage cost as a function of the diffusion length for the radii not to be optimal. In this scenario, I imposed one of the normalized radii to be equal to

the typical value of the normalized radii in pyramidal neurons and the other to be the optimal radius for a fixed value of λ. I compared the protein requirement of such a system with the protein requirement obtained from the measured values of the radii. I observed that increasing the diffusion length above $100\mu m$ leads to a small increase in the extra cost for not optimal radii, compared to smaller diffusion lengths, resulting in faster growth in the protein requirement.

7.4 Summary

In this section, I analyzed 29 dendritic branches, and I used their radii and their length to invert Eq. 69 and find the diffusion length that each branch is optimizing for. I showed how the optimized diffusion length is smaller than the ones from real proteins and that the increase of the protein requirement for $\lambda > \lambda_{opt}$ increases more slowly than the protein requirement of protein with $\lambda < \lambda_{opt}$.
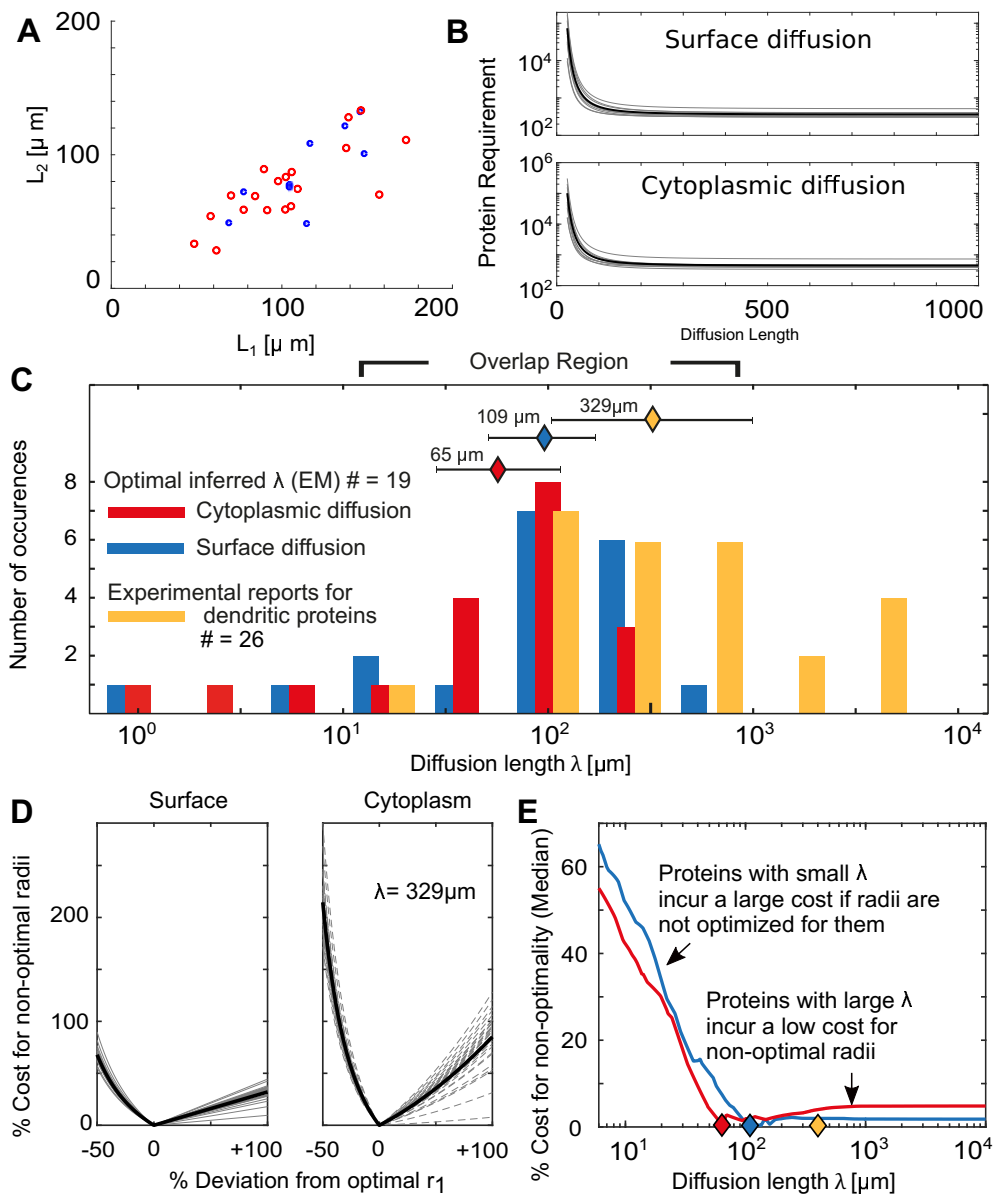
Figure 23: **Optimal and Real Diffusion Lengths** This figure compares the distributions of optimized diffusion lengths obtained from the morphologies to the protein diffusion length and shows the cost for non-optimal diffusion lengths and radii. A) The lengths of the two daughter dendrites are plot one against the other. The Red circles are branches where $R_1 > R_2$, and the blue circles branches where $R_1 < R_2$. B) When $R_1 < R_2$, λ cannot be calculated, here I showed that increasing the value of λ reduces the protein requirement for these branches. C) The comparison of optimal inferred λ and the real λ is shown. The optimal inferred one is obtained for the red circled dots of A) using Eq. 69. D) The percentage cost for non-optimal radii is shown as a function of the percentage deviation from the optimal r_1 E) proteins with small diffusion lengths have a higher cost for not fulfilling Eq. 69, than proteins with a high diffusion length. Panel C) and E) are adapted from [7]

8   Complete Neuronal Morphologies

In the previous sections, I first derived a set of instructions to understand how the protein flux splits at a dendritic branch. I predicted a different behavior at a branch for surface and cytoplasmic proteins, and I tested this prediction using fluorescent proteins. Then I derived an equation to find the optimal radii ratio for each value of the diffusion length and analyzed the cost for a deviation from the optimal radii ratio. This chapter builds upon that model by applying what I just described to a complete dendritic arbor. I obtained the reconstructed morphologies of three categories of neurons, hippocampal pyramidal neurons, like the one in Fig. 24-A, cerebellum Purkinje neurons like the one in Fig. 24-B, and granule cells like the one in Fig. 24-C from the online database Neuromorpho [3]. Then I simulated the diffusion equation on those graphs, and I analyzed both the protein distribution, and the protein requirement for each of them.
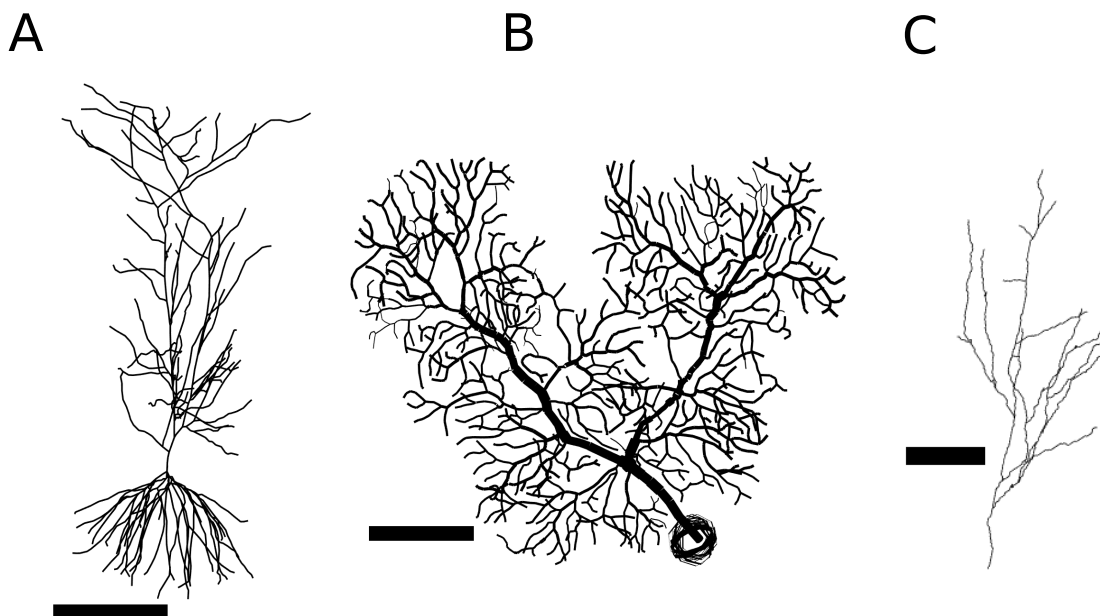
Figure 24: **Overview of the Dendritic Morphologies** This figure shows the three classes of dendritic morphologies I used in the simulations. A) Cortical pyramidal neuron, morphology adapted from [74]. The scale is 200 μm. B) Purkinje neuron, morphology adapted from [75]. The scale is 100 μm. C) Granule cell, morphology adapted from [76]. The scale is 20μm.

8.1   Simulation details

In this section, I described the algorithm I followed to simulate the protein dynamic in the re-constructed morphologies. The morphologies found in Neuromorpho are in the *SWC* format. An SWC file contains an $N \times 8$ matrix, where every line encodes the information of a single com-partment. The first column is an increasing number that labels each compartment. The second is the structure identifier, 1 represents soma, 2 axon, and 3 and 4 proximal and distal dendrites. The $4 - 6$-th columns the x-y-z position, the $7th$ column the radius, and $8th$ column the index of the parent compartment (-1 for the starting point of the graph).

The time step of the simulations have been fixed in Eq. 51: $\Delta t = \frac{\Delta x^2}{2D}$. This requires that all the compartments are equally spaced one from the other. To achieve that, I identified the be-ginning and end of each dendrite, and I regularized it by merging and splitting the compartments into compartments of length Δx. In the following simulations, $\Delta x = 1 \ \mu m$.

At time zero, I inserted 1 protein in the soma, and I followed the fraction of proteins in each compartment in time. At each time step, a fraction $\phi \Delta t \rho(x)$ of proteins are removed from each of the neuronal compartments, including the soma, representing the fraction of dismantled proteins in each compartment. Then, I moved all the proteins from each compartment to the adjacent ones accordingly with the methods described in Sec. 2.4, see Eq. 51 for linear dendrites, Eq. 62 in branches, and Eq. 56 for terminal compartments, these three equation were used with the assumption of no velocity induced by active transport: $v = 0$. Finally, I added $N = \phi \Delta t$ proteins to the soma to compensate for the decayed one; this kept the total number of proteins constant in time. Because of the linearity of the system, I set the $N = 1$. The simulations stop when the system has reached the equilibrium with a precision θ; this means that the maximum relative difference between two consecutive time step (200 hours) is smaller than θ:

$$\theta > \max_x \left(\frac{|\rho(x,t) - \rho(x,t+\delta t)|}{\rho(x,t)} \right). \tag{96}$$

8.1.1 Radii Selection

One of the major shortcomings of this database is the unreliability of many of the measured radii. In Neuron *Purkinje-slice-ageP37-5.CNG*, [77], for example each compartment has exactly the same diameter. For this reason, I decided not to rely on the reported radii and to assume that each branch follows the Rall's rule, with the same exponent $\alpha = 2.3$ found for pyramidal neurons in Sec. 5.3. The Rall exponent by itself is not sufficient to fully determine the normalized radii of the two daughter dendrites: I also needed the value of their ratio.

Here I wanted to explore the impact of the optimality rule I described in Sec. 4.1. To do so, I compared the protein profile and protein requirement in the case of symmetrical branches, where the ratio of the normalized radii is $\frac{r_1}{r_2} = 1$, and optimal branches, where the ratio of the normalized radii is determined by Eq. 69. The optimal radius is also dependent on the diffusion length and on the medium where the protein are diffusing (surface or cytoplasm). For this reason, I studied both surface and cytoplasmic proteins for two values of the diffusion length λ: $\lambda = 109 \ \mu m$, and $\lambda = 473 \ \mu m$. The first is the median of the distribution of the diffusion lengths that the measured branches are optimizing for, as discussed in Sec. 7.1, and the second is the diffusion length of one of the subunits of the GABA receptors, an inhibitory ion channel involved in synaptic plasticity [78, 79].

8.2 Real Morphologies: Pyramidal Neurons

Pyramidal neurons are among the most studied types of neurons and can be found in several brain areas, including the cortex, the hippocampus, and the amygdala. Their structure is easily recognizable (see Fig. 24-A) because of their polarized structure. One of the dendrites stemming from the soma extends for several hundreds of micrometer in a straight direction, and it is called apical dendrite, while the others, from 3 to 5, shorter than the apical one, are called basal dendrites and collect inputs from areas closer to the soma. The length of the apical dendrites is dependent on the area of the brain and the animal species; human pyramidal neurons are usually twice as long

as rat pyramidal neurons, [3]. I selected 64 reconstructed morphologies following the protocol explained in Sec. E.

8.2.1   Protein Distribution and Protein Requirement

Fig.25 shows the Protein distribution of surface and cytoplasmic protein both in the case of symmetrical branches, A-D and in the case of optimized branches, E-H. It can be noticed that the protein distribution of surface protein is higher than the one of cytoplasmic protein in distal dendrites and vice-versa. This is a direct consequence of the probability rule, discussed in Sec. 2.5.

In Fig. 25-A, B, I showed the protein profile in the eight scenarios described before. The box in the color bar alongside shows the minimal and maximal protein density in each compartment. That shows that increasing the diffusion length four times has a limited impact on the protein density while changing the diffusion medium from surface to cytoplasmic, or the radii rule from symmetrical to optimized, has a much more significant impact. This can be better observed in Fig. 26, In the left column, I showed the average number of proteins at a distance x from the soma, while on the right side, I showed the number of proteins needed to populate a percentage f of the whole dendric arbor. In each subplot, the red color represents symmetrical radii, while the blue line optimized radii.

The numbers on the side show the protein needed to populate the 100% (95%) of the dendritic arbor. These results for the eight scenarios are summarized in Table 4. Recalling the estimated number of proteins in the dendritic arbor of a pyramidal neuron, $N_d = 6\ 10^9$, [32, 31], in Table 4, I showed that completely populate the dendritic arbor in case of symmetrical branches would require an unreasonably high number of proteins. In contrast, in the case of perfectly optimized radii, even cytoplasmic protein with a relatively low diffusion length requires fewer than the 0.01% of the protein pool to populate the 95% whole dendritic arbor. I showed both in the figure and in the table the protein requirement for the 95% of the dendritic trees, because the 100% treshold contains a single point, and is much more subject to fluctuations.

	PYR 100%	% for 100%	PYR 95%	% for 95%
$\lambda = 109\,\mu m$, (C,S)	$4.7\ 10^{14}$	$7.8\ 10^6$	$2.9\ 10^{10}$	480
$\lambda = 473\,\mu m$, (C,S)	$3.6\ 10^{12}$	$6\ 10^4$	$1.2\ 10^9$	20
$\lambda = 109\,\mu m$, (S,S)	$3.6\ 10^{11}$	$6\ 10^3$	$4.8\ 10^8$	8
$\lambda = 473\,\mu m$, (S,S)	$2.1\ 10^8$	3.5	$3.6\ 10^6$	0.06
$\lambda = 109\,\mu m$, (C,O)	$9.6\ 10^8$	16	$1.7\ 10^6$	0.03
$\lambda = 473\,\mu m$, (C,O)	$1.0\ 10^6$	0.02	$6.2\ 10^4$	0.001
$\lambda = 109\,\mu m$, (S,O)	$1.2\ 10^8$	2	$1.2\ 10^6$	0.02
$\lambda = 473\,\mu m$, (S,O)	$1.8\ 10^5$	0.003	$3.4\ 10^4$	$6\ 10^{-4}$

Table 7: **Pyramidal Neurons: Protein Requirement Overview:** Protein requirement for the 100% and the 95% of the pyramidal dendritic arbor, and percentage of the total dendritic protein available. (C,S) stands for cytoplasmic diffusion and symmetrical radii; (C,S) stands for cytoplasmic diffusion and symmetrical radii; (C,O) stands for cytoplasmic diffusion and optimal radii; (S,S) stands for surface diffusion and symmetrical radii; (S,O) stands for surface diffusion and optimal radii.

8.3   Purkinje Neurons

Purkinje neurons are cells located in the cerebellum, and they receive input from the granule neurons, which are described in Sec. 8.4. Purkinje were the first neurons to be identified by Jan Evangelista Purkyně in 1832. I selected 32 complete morphologies from Neuromorpho [3], and for each of those, I run the same set of simulations that I described in Sec. 8.2.

In the selected morphologies, the median maximal distance from the soma together with the 50% confidence interval is $M_D = 0.23$ (IQR: 0.23) mm, while the median length of the dendritic arbor is $T_L = 6.00^{+0.93}_{-0.95}$ mm. When compared to a pyramidal neuron, $M_D = 0.90^{+0.28}_{-0.14}$ mm, and $T_L = 14.4^{+3.1}_{-3.2}$ mm, Purkinje are more localized and fill the plane much more densely: while the maximal length of Purkinje cells is four times smaller than the maximal length of pyramidal neurons, the total length is just its half. This is due to the higher number of branches in Purkinje cells than in pyramidal neurons: 340^{+70}_{-50} compared to 92^{+12}_{-7}. In addition to the higher density of branches, the dendritic arbor of Purkinje cells is planar, while pyramidal neurons extend and branch in all three directions.

8.3.1   Protein Distribution and protein Requirement

Analogously to what I did for pyramidal neuron, I simulated both for cytoplasmic and surface proteins, for two values of the diffusion length and symmetrical and optimized radii. To maintain a direct comparison of the simulated morphologies, I used the same branching rule I imposed for pyramidal neurons also for Purkinje cells: $R_1 = R_2 = 0.74$, and $\alpha = 2.3$

Because of the higher number of branches, Purkinje cells have a protein requirement of a similar magnitude of pyramidal neurons, although they are considerably shorter than pyramidal neurons. Fig. 27, shows the protein distribution in all the eight scenarios analyzed. The color code is in a logarithmic scale, and the box in the bar alongside each figure shows the maximum and minimum density of protein in each compartment. In Table 8, I summarized the protein requirement obtained for Purkinje cells in the different scenarios.

8.4   Granule Neurons

Granule was a name used to indicate multiple types of neurons with a common trait; they possess a short dendritic tree and a small soma. Here I focused my analysis on the granule neurons in the cerebellum. Granule neurons are the most abundant types of neurons in the brain [80], they receive inputs from the mossy fibers, and they project their output to Purkinje cells. The average length of a granule cell is considerably shorter than pyramidal and Purkinje neurons, having a median maximal length of $M_L^{\mathrm{Gra}} \sim 148\,\mu m$ compared to the $M_L^{\mathrm{Pyr}} \sim 897\,\mu m$ of pyramidal neurons. Because their morphological properties are highly different from the ones of pyramidal and Purkinje neurons and their abundance in the brain, I decided to test my model on this class of neurons.

8.4.1   Protein Distribution and Protein Requirement

As I did for pyramidal and Purkinje neurons, I run the same set of simulations on granule cells. I selected 143 granule neurons, and I showed the average protein distribution and protein require-

ment in Fig. 29 and in Fig. 30. As was expected, the total number of proteins needed to populate a granule cell is significantly smaller than for pyramidal and Purkinje neurons. The protein requirement for the 95% and 100% of the dendritic arbor are shown both in 30, right column, and summarized in Table, 8.

8.5   Brief Summary

In this section, I simulated the protein distributions for three types of neurons and analyzed the number of proteins needed to populate a certain percentage of their dendritic arbor. I repeated this process for 64 distinct dendritic morphologies in the case of pyramidal neurons, 32 morphologies for Purkinje neurons, and 143 for granule neurons. For each of those morphologies, I simulated two values of the diffusion length: $\lambda = 109\ \mu m$ and $\lambda = 473\ \mu m$, and two rules for the branching radius: symmetrical with $R_1 = R_2 = 0.74R_0$, and optimal, accordingly with the procedure described in Sec. 4.2. The summary of the protein requirement for a specific percentage of the dendritic arbor is summarized in Table 8.

For pyramidal branches, I compared the protein requirement with the total number of dendritic proteins, as estimated in the introduction: $N_d \sim 6\ 10^9$, and I expressed the protein requirement in terms of percentage of the total dendritic proteins, see Table 7. I showed that optimizing the radii reduces the fraction of proteins needed to match the protein requirement below the 0.1% for every type of proteins with a relatively low diffusion length $\lambda \geq 109\mu m$.

	PYR 100%	PYR 95%	PUR 100%	PUR 95%	GRA 100%	GRA 95%
$\lambda = 109\ \mu m$, (C,S)	$4.7\ 10^{14}$	$2.9\ 10^{10}$	$1.2\ 10^{19}$	$1.4\ 10^{11}$	$5.5\ 10^{5}$	$4.8\ 10^{3}$
$\lambda = 473\ \mu m$, (C,S)	$3.6\ 10^{12}$	$1.2\ 10^{9}$	$7.9\ 10^{18}$	$1.0\ 10^{11}$	$4.3\ 10^{4}$	$3.4\ 10^{3}$
$\lambda = 109\ \mu m$, (S,S)	$3.6\ 10^{11}$	$4.8\ 10^{8}$	$1.2\ 10^{11}$	$1.3\ 10^{7}$	$6.7\ 10^{3}$	$1.8\ 10^{3}$
$\lambda = 473\ \mu m$, (S,S)	$2.1\ 10^{8}$	$3.6\ 10^{6}$	$4.0\ 10^{10}$	$6.3\ 10^{6}$	$3.7\ 10^{3}$	$1.2\ 10^{3}$
$\lambda = 109\ \mu m$, (C,O)	$9.6\ 10^{8}$	$1.7\ 10^{6}$	$9.5\ 10^{9}$	$7.4\ 10^{5}$	$3.3\ 10^{3}$	$1.9\ 10^{3}$
$\lambda = 473\ \mu m$, (C,O)	$1.0\ 10^{6}$	$6.2\ 10^{4}$	$3.0\ 10^{9}$	$4.0\ 10^{5}$	$1.9\ 10^{3}$	$1.4\ 10^{3}$
$\lambda = 109\ \mu m$, (S,O)	$1.2\ 10^{8}$	$1.2\ 10^{6}$	$1.9\ 10^{7}$	$8.4\ 10^{4}$	$1.8\ 10^{3}$	$1.2\ 10^{3}$
$\lambda = 473\ \mu m$, (S,O)	$1.8\ 10^{5}$	$3.4\ 10^{4}$	$2.3\ 10^{6}$	$3.2\ 10^{4}$	$1.2\ 10^{3}$	910

Table 8: **Protein Requirement overview:** for 100% and 95% of the dendritic arbor. For the three classes of real morphologies analyzed. (C,S) stands for cytoplasmic diffusion and symmetrical radii; (C,S) stands for cytoplasmic diffusion and symmetrical radii; (C,O) stands for cytoplasmic diffusion and optimal radii; (S,S) stands for surface diffusion and symmetrical radii; (S,O) stands for surface diffusion and optimal radii.

Figure 25: **Pyramidal Neurons: Overview** In this figure I showed the distribution of somatic and diffusive proteins at the equilibrium in eight different scenarios. In A,B,C,D) I imposed symmetric branches, where $R_1 = R_2 = 0.74\,R_0$; In E,F,G,H) I imposed the optimal radii as described in Sec. 4.2; in A,C,E,G) I imposed a diffusion length $\lambda = 109\mu m$, as obtained from the median of the optimized diffusion length in Fig. 23-C, and in B,D,F,H) I imposed the diffusion length $\lambda = 473\mu m$ that I found for AMPA receptors, see Table 11. The errorbar is the scale of the neuron, and is $200\mu m$ long. The colorcode represents the density of proteins in each compartment ($\Delta x = 2\mu m$). The box on the side of each neuron shows the lower and the higher density of proteins in each compartment.

Figure 26: **Pyramidal Neurons: Protein Density and Protein Requirement** In this figure, I showed the average density of proteins at a distance x from the soma, left column, and the number of proteins required to have at least 1 protein per micrometer in a certain percentage of the dendritic arbor in the right column. I repeated the plot four times, two values of λ and two diffusion modes, surface, and cytoplasm. Each plot contains two subplots, namely the profiles obtained for symmetrical branches in red and the ones obtained for optimized branches in blue. The numbers on the right side of the right column are the number of proteins needed to bring at least one protein in each compartment in each scenario.

Figure 27: **Purkinje Neurons: Overview** In this figure I showed the distribution of somatic and diffusive proteins at the equilibrium in eight different scenarios. In A,B,E,F) I imposed symmetric branches, where $R_1 = R_2 = 0.74 \, R_0$; In C,D,G,H) I imposed the optimal radii as described in Sec. 4.2; in A,C,E,G) I imposed a diffusion length $\lambda = 109 \mu m$, as obtained from the median of the optimized diffusion length in Fig. 23-C, and in B,D,F,H) I imposed the diffusion length $\lambda = 473 \mu m$ that I found for AMPA receptors, see Table 11. The errorbar is the scale of the neuron, and is $100 \mu m$ long. The colorcode represents the density of proteins in each compartment ($\Delta x = 2 \mu m$). The box in the bar alongside each figure, shows the lower and the higher density of proteins in each compartment.
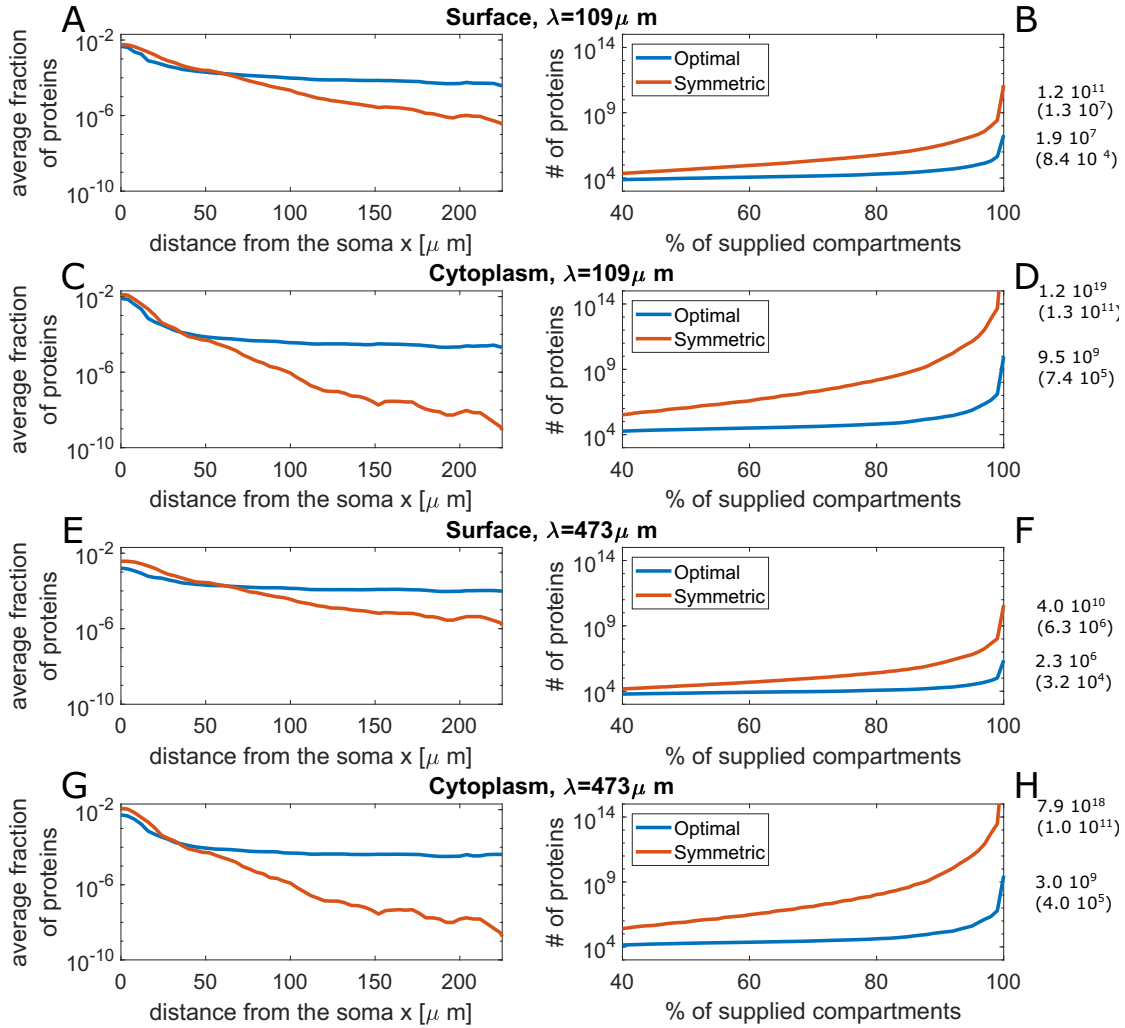
Figure 28: **Purkinje Neurons: Protein Density and Protein Requirement** In this figure, I showed the average density of proteins at a distance *x* from the soma, left column, and the number of proteins required to have at least 1 protein per micrometer in a certain percentage of the dendritic arbor in the right column. I repeated the plot four times: for two values of λ and two diffusion modes, surface, and cytoplasm. Each plot contains two subplots, namely the profiles obtained for symmetrical branches in red and the ones obtained for optimized branches in blue. The numbers on the right side of the right column are the number of proteins needed to bring at least one protein in each compartment in each scenario.
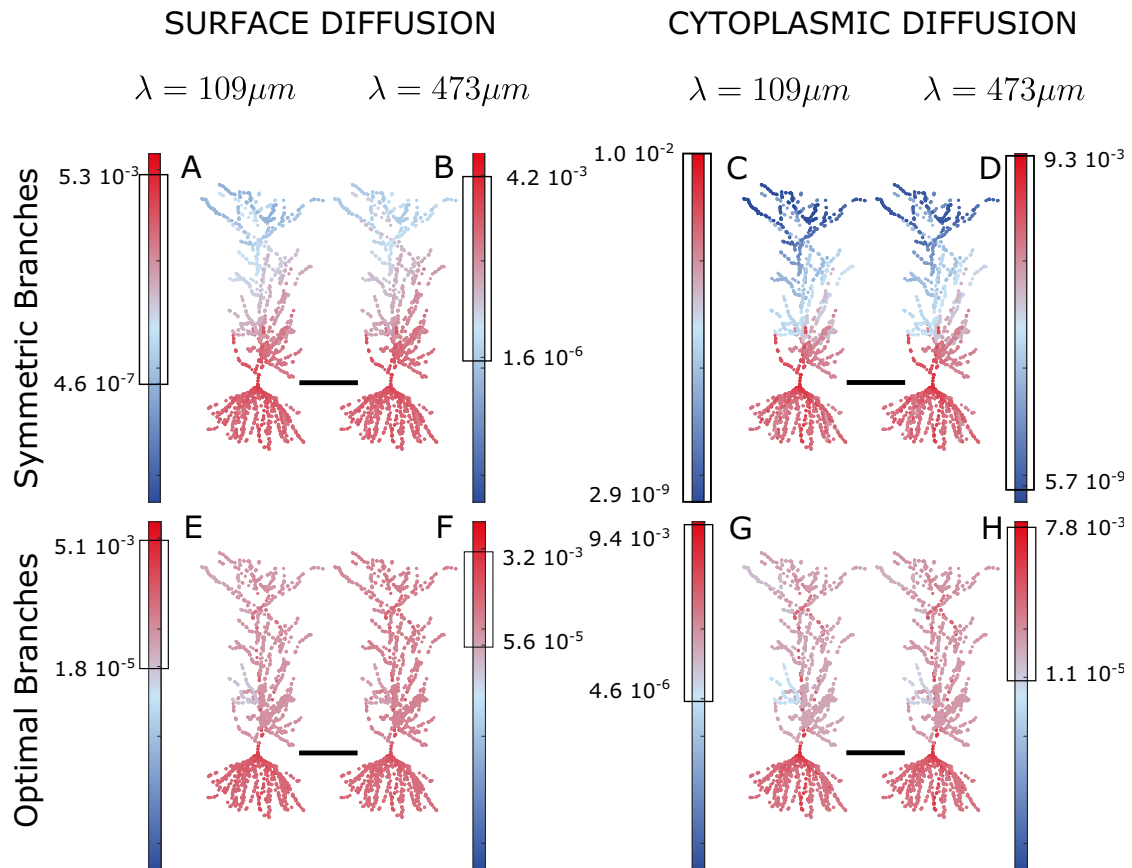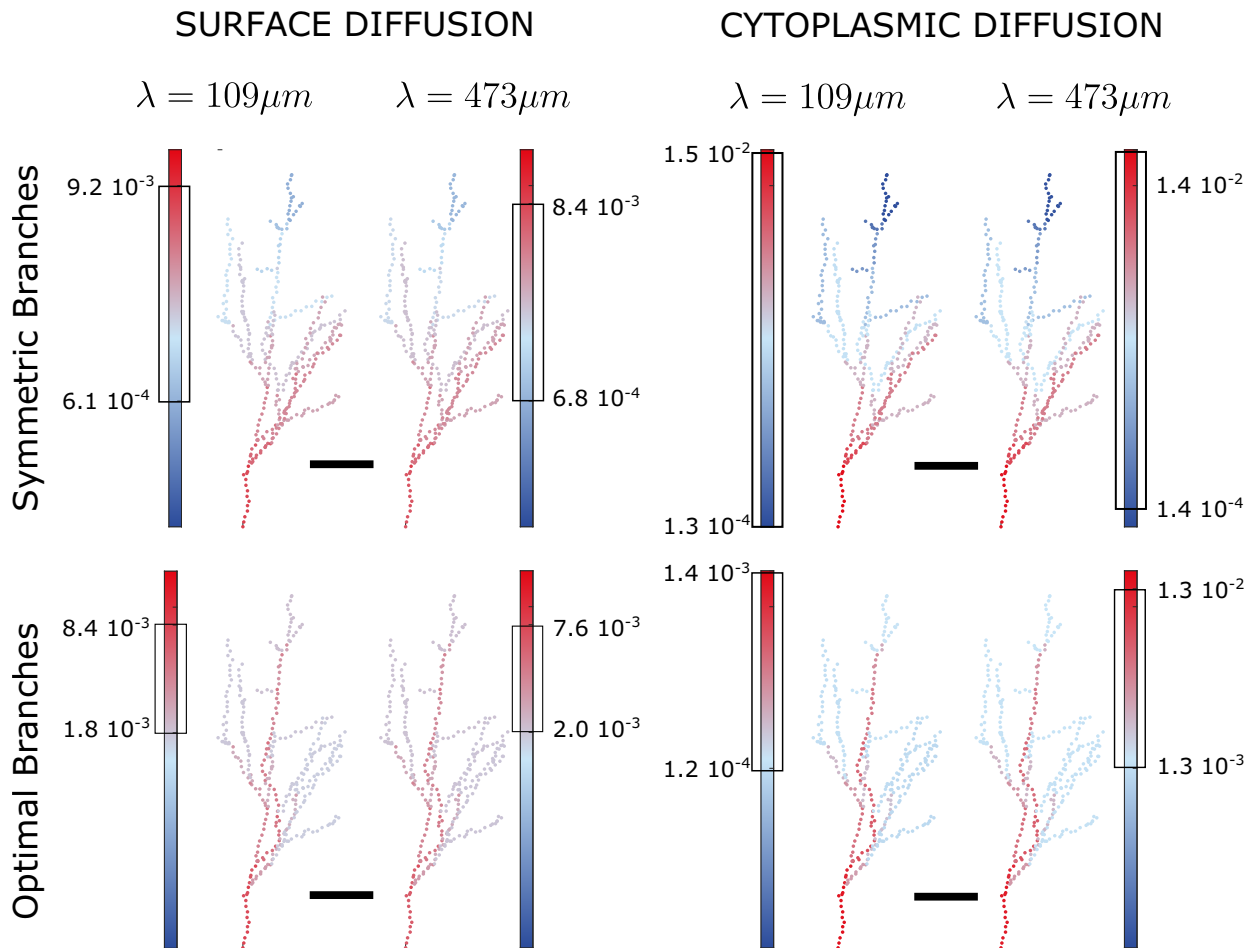
Figure 29: **Granule Neurons: Overview** In this figure I showed the distribution of somatic and diffusive proteins at the equilibrium in eight different scenarios. In A,B,C,D) I imposed symmetric branches, where $R_1 = R_2 = 0.74\,R_0$; In E,F,G,H) I imposed the optimal radii as described in Sec. 4.2; in A,C,E,G) I imposed a diffusion length $\lambda = 109\mu m$, as obtained from the median of the optimized diffusion length in Fig. 23-C, and in B,D,F,H) I imposed the diffusion length $\lambda = 473\mu m$ that I found for AMPA receptors, see Table 11. The errorbar is the scale of the neuron and is $20\mu m$ long. The color code represents the density of proteins in each compartment ($\Delta x = 2\mu m$). The box on the color bar alongside each neuron shows the lower and the higher density of proteins in each compartment.
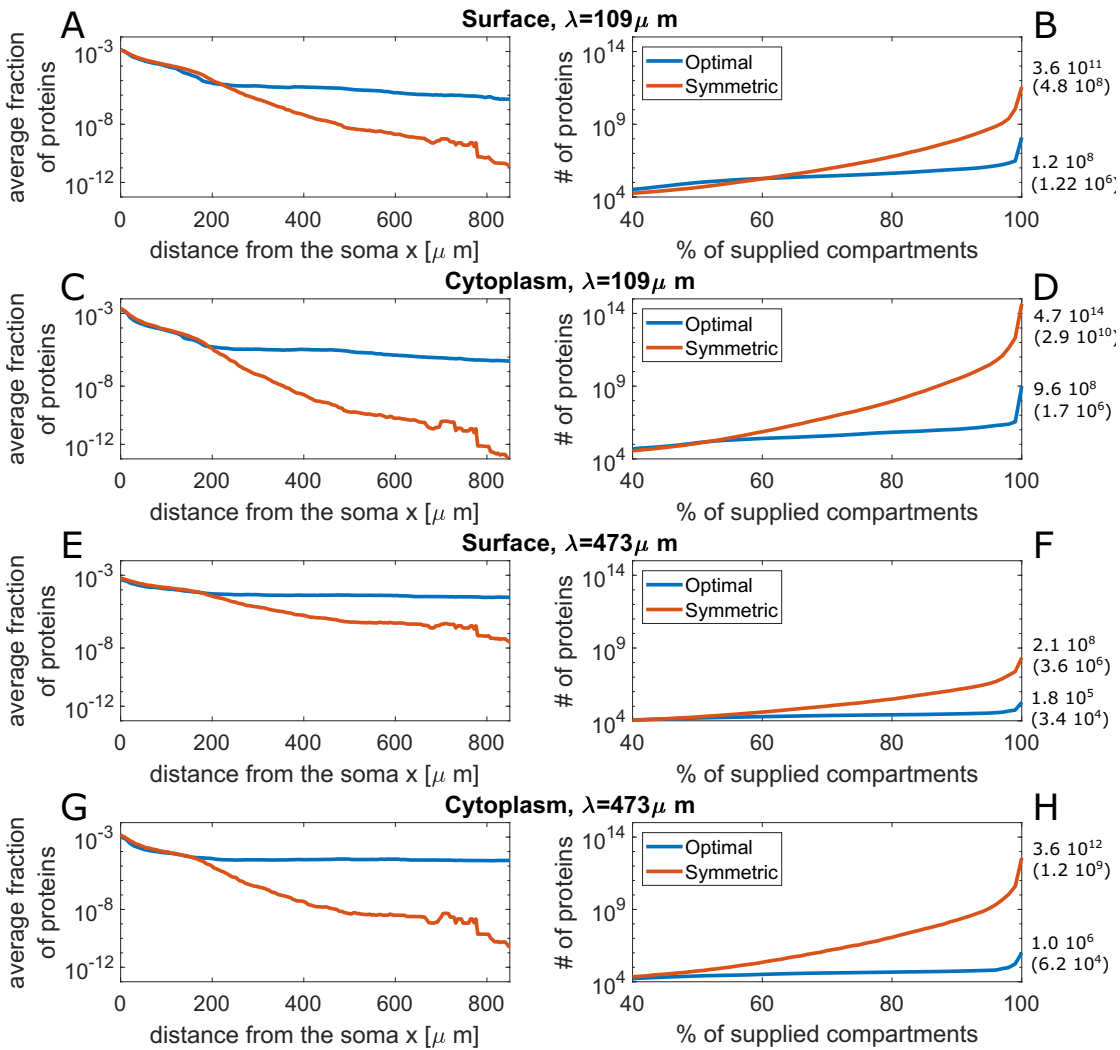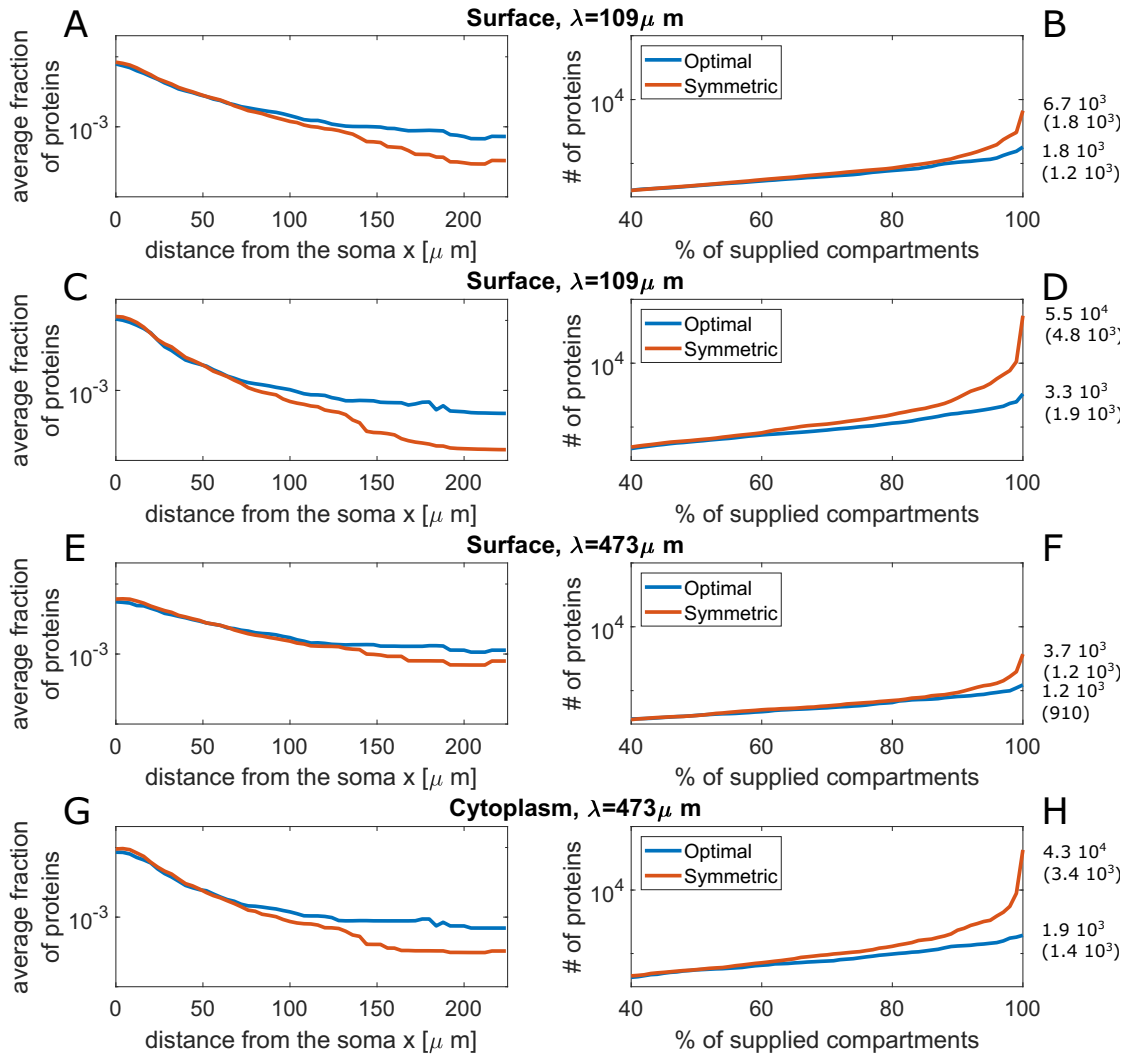
Figure 30: **Granule Neurons: Protein Density and Protein Requirement** In this figure, I showed the average density of proteins at a distance *x* from the soma, left column, and the number of proteins required to have at least 1 protein per micrometer in a certain percentage of the dendritic arbor in the right column. I repeated the plot four times, two values of λ and two diffusion modes, surface, and cytoplasm. Each plot contains two subplots, namely the profiles obtained for symmetrical branches in red and the ones obtained for optimized branches in blue. The numbers on the right side of the right column are the number of proteins needed to bring at least one protein in each compartment in each scenario.
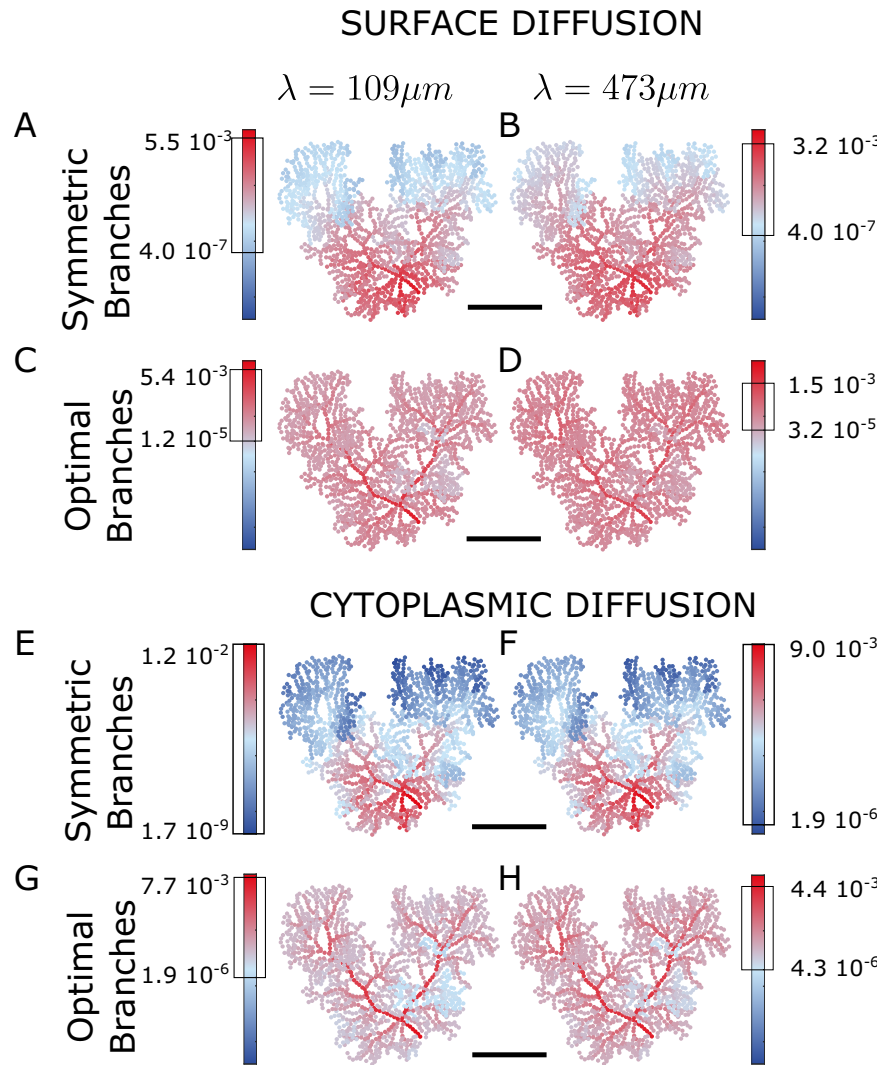
9   Conclusion

In this section, I summarized the main results obtained in this dissertation in Sec. 9.1, as well as the main limitations and the potential solutions to those issues in Sec. 9.2.

9.1   Main Results

Here, I summarized the main results I obtained in this work. Obtaining the protein profile for different transport mechanisms is the first step to understanding the number of proteins needed to populate the dendritic arbor. I defined the *protein number* as the average number of protein that a neuron needs to produce to have a minimal density of 1 protein/μm; Knowing the protein number for many different models, I showed that the optimal protein numbers happens when the mRNA translation happens throughout the whole dendritic arbor at a constant rate. That leads to a constant protein profile. I used that as a benchmark to understand how expensive the other models are for populating a linear dendrite.

Understanding the protein requirement for each morphology and for each transport mechanism is important to understand how the dendrite can populate reliably the dendritic arbor, but it is only a part of the story. In Sec. 2 I discussed how proteins can be translated in the dendrites, opening the problem of transporting mRNA in dendrites. I am currently working on a more general problem, where instead of considering the protein requirement of a model, it considers its whole energy requirement in terms of ATP.

The main contributions to the energy requirement are the protein translation, the mRNA transcription, which can be obtained also from the model explained in this thesis, and the cost for keeping the proteins and mRNA in the active state.

9.1.1   Branch Rule

The next level of complexity arises when diffusive proteins meet a branch. I showed that the probability of a protein diffusing in an afferent dendrite depends on the available space in that

dendrite:

$$P(\text{Branch} \rightarrow \text{Dendrite}_i) = \frac{R_i^\gamma}{R_0^\gamma + R_1^\gamma + R_2^\gamma}, \tag{97}$$

where $\gamma = 1$ in case of a protein diffusing on the surface, and $\gamma = 2$ in case of a protein diffusing in the cytoplasm. The protein distribution I've found in this section relies on the assumption that on long time-scale the dynamic of the diffusive proteins is diffusive; many example of anomalous diffusion in neurons have shown that the anomalous diffusion behavior happens on a relatively short time scale, a couple of seconds in [81].

9.1.2   Radii Statistics

To understand the consequence of the branch rule in different real neurons, I analyzed three distinct datasets of neurons, A published dataset of crab STG neurons, [2], and two previously unpublished ones, one for cultured hippocampal neurons and one of 3D-EM Prefrontal pyramidal neurons. For these three datasets, I obtained the radii distribution for the mother and both daughter dendrites, and using it, I calculated the distribution of the Rall exponent α. The Rall exponent is a helpful indicator for the behavior of each branch; for positive values of α, the higher is the Rall exponent, the bigger are the two daughter dendrites.

The median values of the Rall exponent and 50% confidence intervals I obtained for the three types of neurons are

1. $\mathbb{E}[\alpha] = 2.3$ (IQR: $1.8 - 3.3$) for pyramidal nuerons;

2. $\mathbb{E}[\alpha] = 2.0$ (IQR: $1.5 - 2.9$) for cultured neurons;

3. $\mathbb{E}[\alpha] = 1.0$ (IQR: $0.72 - 1.47$) and for STG neurons.

The value of the Rall Exponent of pyramidal neurons is compatible with the previously published one: $\alpha = 2.28 \pm 0.89$ for basal dendrites and $\alpha = 1.69 \pm 0.48$ for apical dendrites[72].

9.1.3   Probability Ratio and Surface Bias

It is possible to evaluate the impact of branches on the protein distribution if the radii are known. Because of the high variability in the normalized daughter radii that I showed in Sec. 5, the fraction of proteins moving into each daughter dendrite is not the same for each branch. To have an understanding of the behavior of surface and cytoplasmic proteins, I defined the *probability ratio* as:

$$Q_P = \frac{R_1^\gamma + R_2^\gamma}{R_0^\gamma}, \tag{98}$$

where γ is the dimensionality of the media where the proteins are diffusing. $\gamma = 1$ for surface proteins, $\gamma = 2$ for cytoplasmic proteins.

In Fig. 17 I showed the dependency of the probability ratio upon the radius of one of the two daughter dendrites for four values of α. I showed that as long as $\alpha > 0$ the probability ratio of surface proteins, in blue ($\gamma = 1$), is higher than the probability ratio of cytoplasmic proteins, in Red ($\gamma = 2$). Fig. 19, 20, 21-F show the distribution of the probability ratio of surface (blue) and cytoplasmic proteins (red), for cultured, STG and cortical pyramidal neurons respectively. For pyramidal and cultured neurons, most of the analyzed daughter dendrites have a smaller radius than the mother dendrite. Therefore the probability ratio of surface proteins is higher than the probability ratio of cytoplasmic ones. Therefore, surface proteins are more likely to move away from the soma when they encounter a branch than cytoplasmic proteins.

This behavior is characterized in Fig. 19, 20, 21-G using the *Surface Bias*:

$$Q_P^{S/C} = \frac{Q_P^S}{Q_P^C} - 1. \tag{99}$$

The surface bias represents the relative increase in the abundance of surface proteins over cytoplasmic protein after the branch.

9.1.4   Fluorescence Ratio

Once I knew the probability ratio of cultured neurons, that represents the average increase in the number of proteins after each branch, I analyzed the data provided us by one of our collaborators, A.S. Hafner. There I measured the increase in integrated fluorescence after each branch:

$$Q_F = \frac{F_1\left(m,\Delta\right) + F_2\left(m,\Delta\right)}{F_0\left(m,\Delta\right)}, \tag{100}$$

as shown in Fig. 22-E for several values of m and Δ. Averaging over m and Δ leads to a Fluorescence ratio for surface and cytoplasmic proteins as summarized in Table 9.

	Q_P^S	Q_P^C	$Q_P^{S/C}$
Cortical pyramidal neurons	$1.49\ (1.35-1.65)$	$1.14\ (0.95-1.37)$	$0.28\ (0.2-0.38)$
STG neurons	$1.23\ (0.94-1.68)$	$0.92\ (0.52-1.58)$	$0.34\ (0.10-0.67)$
Cultured neurons -Radii	$1.45\ (1.27-1.65)$	$1.12\ (0.84-1.38)$	$0.28\ (0.2-0.46)$
	Q_F^S	Q_F^C	$Q_F^{S/C}$
Cultured Neurons -Fluorescence	1.48 ± 0.15	1.23 ± 0.08	0.22 ± 0.03

Table 9: Overview of the median, and first-to-third interquartile of the probability ratio of surface proteins, probability ratio of cytoplasmic proteins, and surface bias, for cultured, cortical and STG neurons. For the fluorescence signal I reported the mean and standard error of the mean.

9.1.5   Optimality Rule

After analyzing every branch's behavior, I returned to the original problem of studying the impact of each branch on the protein requirement of diffusive proteins. Because the amount of protein diffusing toward each of the two daughter dendrites depends on their radius, I searched the radius that minimizes the protein requirement, calling it *optimal radius*. The optimal radius must follow the following relation:

$$\frac{\cosh\left(\frac{L_1}{\lambda}\right)}{\cosh\left(\frac{L_2}{\lambda}\right)} = \frac{R_1^\gamma}{R_2^\gamma}. \tag{101}$$

In [69], the authors explored the branch rule and the tapering that optimizes the transmission of electric signals from the dendrites to the soma, imposing a similar rule:

$$\frac{L_1^{3/2}}{L_2^{3/2}} = \frac{R_1}{R_2}. \tag{102}$$

9.1.6   Effective length

The previously discussed equation gives a method to find the optimal radii ratio only for terminal branches, where both L_1 and L_2 are known. However, if the dendritic morphology has multiple consecutive branches, that equation cannot be applied directly; in Sec. 4.2 I described the algorithm to optimize the radii of an arbitrary morphology. In brief, it assigns to each terminal branches an effective length, L_{eff} as defined in Eq. 71, and it replaces the mother and two daughter dendrites with a single dendrite of length L_{eff} and radius equal to the mother dendrite radius. I repeat this procedure until a single linear dendrite replaces the whole dendritic arbor.

9.1.7   Real Diffusion lengths and Optimized diffusion length

The equation described to obtain the optimal radii can be inverted and applied to real morphologies where both the lengths of the dendrites and their radii are known. In that scenario, I used it to infer the value of the diffusion length that each branch is optimizing for. In Fig. 23, I showed the distribution of the diffusion length obtained in that way in Blue for surface proteins and in Red for cytoplasmic proteins. In yellow, I overlayed the distribution of diffusion length of real protein obtained from the literature.

The median value of the optimized diffusion length of surface proteins, and the 50% confidence interval are $109\ (57 - 164)$, for cytoplasmic proteins are $65\ (32 - 132)$ and for the measured diffusion length are $329\ (104 - 986)$.

9.1.8   Cost for Non-Optimality

As shown in Fig. 23-C, the typical diffusion length of real proteins is higher than the diffusion length that the dendrites are optimizing for. In Fig. 23-E I showed that the percentage cost for non-optimality increases more slowly for protein with a higher diffusion length than for proteins with a lower one. Understanding the cost for non-optimality in different scenarios is important when one wants to compare two models. In [69], the authors explore the impact of radii and tapering upon current transfer from the dendrites to the soma. I am currently working in a collaboration to compare the two models, and the two predicted predicted optimal branching rules. To do so, a weight function that consider the cost for the deviation from the optimal radii must be introduced.

9.1.9   Protein Requirement for Real Morphologies

The final thing that I showed in this work is the average protein requirement for three classes of neurons: pyramidal, Purkinje, and granule neurons. I chose two diffusion length values, and I calculate the protein density and requirement for each neuron. Then, I repeated for both symmetric and optimized branch radii and both for surface and cytoplasmic proteins.

In the case of pyramidal neuron, I roughly estimated the total number of protein that it can contain to be $N_{tot} = 1.6 \ 10^{10}$, $N_{dend} = 6 \ 10^9$ of which are dendritic proteins. I then compared that with the protein requirement obtained in Fig. 26, right column. I showed that in case of symmetrical branches, diffusion requires a very high number of proteins to provide enough proteins to the 95% of the dendritic arbor. With the sole exception of diffusion at the surface and high diffusion length. While in case of optimized morphology the protein requirement is relatively small compared to the total pool of proteins available to the neuron, as summarized in Table 10:

This shows that diffusion, together with radii optimization, is sufficient to transport highly diffusive proteins, $\lambda > 400$, and it might be enough to transport protein with an average diffusion length $\lambda \sim 100$. Only protein with high diffusion lengths can populate distal dendrites with less than the 0.1% of the dendritic budget if the radii are symmetrical.

	PYR 95%	Percentage of the dendritic pool
$\lambda = 109$ Cyto, Symm	$2.9 \ 10^{10}$	480
$\lambda = 473$ Cyto, Symm	$1.2 \ 10^{9}$	20
$\lambda = 109$ Surf, Symm	$4.8 \ 10^{8}$	8
$\lambda = 473$ Surf, Symm	$3.6 \ 10^{6}$	0.06
$\lambda = 109$ Cyto, Opt	$1.7 \ 10^{6}$	0.03
$\lambda = 473$ Cyto, Opt	$6.2 \ 10^{4}$	0.001
$\lambda = 109$ Surf, Opt	$1.2 \ 10^{6}$	0.02
$\lambda = 473$ Surf, Opt	$3.4 \ 10^{4}$	0.0006

Table 10: **Pyramidal Neurons:** Protein requirement overview, Protein requirement for the 95% of the pyramidal dendritic arbor, and percentage of the total dendritic protein available.

In [82], the authors estimate an average of 140 GABA receptors per synapse. Assuming that all the receptors diffusing in the dendrite are available to the adjacent synapses, and a density of synapses of 1 synapse/μm, the the typical dendritic arbor needs to synthetize $N = 5 \times 140 \times N_{95} \sim 23 \ 10^6$ GABA receptors to populate the 95% of the pyramidal dendritic tree, where 5 is the number of subunits composing a GABA receptor.

9.2   Main Limitations

Here, I explored the main limitations of the models, both in terms of predictions of the model that are inconsistent with current experimental observations like in Sec. 9.2.1, and in terms of important components of dendritic transport that are not included in the model.

9.2.1   Active transport leads to accumulation at dendritic tips even for low velocities

In Sec. 2, I calculated the protein profile in case of active transport in a dendrite of length $L = 200 \mu m$. There I showed that even for effective velocities much smaller than the measured ones, there is an accumulation of proteins toward the end of the dendrite, see Fig. 6 A, B. A trapping mechanism that slows down the active transport could compensate and prevent this accumulation. There are indications that microtubules in distal dendrites have a more parallel orientation than

the ones in proximal dendrites, [29], tuning the number of dyneins attached to each cargo could regulate the velocity of the cargo itself.

Another mechanism that could play a role in preventing this accumulation is to expand the argument made in Sec. 2.2, to derive an effective velocity by introducing a long-tailed waiting time, as observed, and modeled, in [49] for mRNP. I am currently investigating the trapping effect due to synaptic intake.

9.2.2   Crowding problem

In Fig. 25, I showed the predicted protein profile in the case of purely diffusive proteins in pyramidal neurons. In a soluble protein with a low diffusion length, the difference in concentration is over seven orders of magnitude. That would lead to not having enough protein in distal dendrites or having an extremely high density of proteins close to the soma. This extreme gradient of proteins cannot be described using the methods I explained in this thesis because the underlying assumption of the diffusion equation is that the medium must be isotropic. However, this gradient in concentration could be modeled by considering the space occupied by each protein and the available space remaining for diffusion, resulting in an effective velocity of proteins toward distal dendrites.

9.2.3   Non-constant radii

The main assumption I made in this thesis is that the dendrites have to be cylindrical. Tapering plays an important role in maximizing the transmission of the signal received in dendrites toward the soma, [70, 71, 69]. Similarly, the cross-section of dendrites undergoes random fluctuations in its radius due to the presence of other external dendrites, axons, astrocytes, and blood vessels.

I am currently studying how to model the effect of a decreasing radius using an effective velocity toward the beginning of the dendrite. Doing so would allow comparing directly the optimality rule I derived in this thesis with the one derived in [69].

9.2.4 Distribution of diffusion coefficient

In experiments in which the diffusion coefficient is estimated using single-particle tracking, the authors often show the distribution of the diffusion coefficient of different proteins. The range of the measured diffusion coefficient often spans multiple orders of magnitude, [83]. Often, the two range of diffusion coefficients are referred to as mobilized and immobilized proteins. This is because proteins interact with their environment and can be anchored to other proteins. In the case of ion channels in synapses, one of these anchor proteins is called PSD-95, [84]. In this dissertation, I used the median of such distribution, but a more complex dynamic can be explored. For example, this immobilization could be used to explain the lack of accumulation of proteins at the dendritic tip in case of active transport, as discussed in 9.2.1.

9.2.5 Anomalous diffusion in dendrites: ER and active transport

In dendrites there are at least two sources of anomalous diffusion, the sub-diffusive behavior of membrane associated proteins diffusing in the ER, and the super-diffusive behavior of mRNP cargo moving on microtubules.

The endoplasmic reticulum, is a fractal-like structure inside the dendritic tree; because of that, it has been shown that the movement of proteins in it displays anomalous diffusion (sub-diffusion). The dimensionality of the space they are exploring is dictated by the fractal dimension $d_f = 1.6$ [59]. This sub-diffusive behavior is another candidate to compensate for the protein accumulations at the dendritic tip due to active transport.

In a recent paper, [49], the authors showed that mRNP displays a Lévy-walk type of sub-ballistic super-diffusion with a mean square displacement that scales as $t^{1.8}$, before being immobilized with a long-tailed waiting time. A Lèvy-walk allows mRNP to move quickly away from the soma before being immobilized and cannot be modeled using the diffusion equations I used in this thesis but requires more sophisticated tools, like the fractional Fokker-Planck, or continuous time random walk (CTRW).

9.2.6 Completely Reconstructed Morphologies

In the last chapter of this dissertation, I explore the protein requirement in reconstructed morphologies where the radii are obtained by assuming the Rall rule. This is due to the radius of the dendrite being often comparable, or smaller than the optical limit. Using 3D-EM reconstructed morphology, would solve this problem, but it is currently extremely challenging. The main technological limitations are the high amount of memory required to image the whole extent of the dendritic arbor of pyramidal neurons, on the order of $1mm \times 400\mu m \times 400\mu m$, while state-of-the-art datasets have a size of on the order of $100 \times 100 \times 60\mu m$ [85], and the complexity of the algorithms needed to reconstruct the neurons, for a discussion on these limitations, see [86].

Appendices

A General solution of the diffusion equation on an infinite line

In this section I summarized the general solution to the generalized diffusion equation. This is a known solution of the generalized diffusion equation:

$$\frac{\partial}{\partial t}\rho(x,t) = D\frac{\partial^2}{\partial x^2}\rho(x,t) - v\frac{\partial}{\partial x}\rho(x,t) - \phi\rho(x,t) + \varepsilon(x,t). \tag{103}$$

Here v represents a drift term, ϕ the degradation rate and $\varepsilon(x,t)$ the translation rate.

A.1 Reduction to a simpler problem

For simplicity I expressed Eq. 103 in a more compact way:

$$\rho_t = D\rho_{xx} - v\rho_x - \phi\rho + \varepsilon. \tag{104}$$

where the subscripts x and t represent the derivative in space or in time respectively. It is possible to express Eq. 104 in terms of $f(x)$:

$$f_t = Df_{xx} + f_x(2DA - v) + f\left(DA^2 - Av + B - \phi\right) + \frac{\varepsilon}{e^{Ax-Bt}}, \tag{105}$$

where

$$\rho(x,t) = f(x,t)e^{Ax-Bt}, \tag{106}$$

and A, and B are free parameters,

It is possible to choose A and B such that the coefficients of f_x and f are equal to zero. This is possible by setting

$$A = \frac{v}{2D} \tag{107}$$

and

$$B = +\frac{v^2}{4D} + \phi. \tag{108}$$

Eq. 104 can be therefore rewritten as

$$f_t = D f_{xx} + \eta \tag{109}$$

where $\eta = \frac{\varepsilon}{e^{Ax - Bt}}$.

A.2 General Solution for known initial conditions using Fourier Transform

To solve Eq. 109, with initial conditions $f(x,0) = \psi(x)$ and inhomogenous term $\eta(x,t)$ set to zero, one applies the Fourier transform:

$$\widehat{f_t} - D\widehat{f_{xx}} = \widehat{f_t} - D(ik)^2 \widehat{f} = 0; \tag{110}$$

with initial condition

$$f(k,0) = \widehat{f}(k). \tag{111}$$

Multiplying Eq.110 by $e^{Dk^2 t}$, it can be rewritten as

$$\frac{\partial}{\partial t}\left[\widehat{f} e^{Dk^2 t}\right] = 0; \tag{112}$$

and therefore $\widehat{f} e^{Dk^2 t}$ is independent of t.

That allowed me to identify $\psi(k)$ with $\widehat{f}(k,0)$, and $\widehat{f}(k,t) = \widehat{\psi} e^{-Dk^2 t}$. Knowing that $e^{-Dk^2 t}$ is the Fourier transform of

$$\mathcal{F}^{-1}\left[e^{-Dk^2 t}\right] = S(x,t) = \frac{1}{\sqrt{4\pi Dt}} e^{-x^2/4Dt}, \tag{113}$$

I used the convolution theorem, and the analytical expression of $f(x,t)$ is:

$$f(x,t) = \frac{1}{\sqrt{4\pi Dt}} \int_{-\infty}^{+\infty} e^{-(x-y)^2/4Dt} \psi(y)\, dy. \tag{114}$$

A more general solution, that includes the inhomogeneous term $\eta(x,t)$ dependent on time and space can be found in [87]:

$$f(x,t) = \int_{-\infty}^{\infty} S(x-y,t)\psi(y)\, dy + \int_0^t \int_{-\infty}^{\infty} S(x-y,t-s)\eta(y,s)\, dy\, ds, \tag{115}$$

where $\psi(x)$ are the initial conditions, and $\eta(x,y)$ contains both the constant degradation and the production terms

A.3   No active transport, no degradation, no translation

If one considers a system without a directional active transport, $v = 0\mu m/s$, without protein translation, $\varepsilon = 0$, without degradation $\phi = 0$ and where all the proteins are at $x = 0$ at time $t = 0$, $\psi(x) = \delta(x)$, Eq. 115 becomes:

$$\rho(x,t) = \frac{1}{\sqrt{4\pi Dt}} e^{-x^2/4Dt}. \tag{116}$$

A.4   No active transport, degradation, and translation only in the soma

A system without a directional active transport, $v = 0\mu m/s$, with protein translation only at the soma, $\varepsilon = \beta\delta(x)$, where all the proteins are at $x = 0$ at time $t = 0$, $\psi(x) = \delta(x)$, but with degradation constant in the dendritic arbor, can be reduced to the same problem of Eq. 109 by imposing:

$$A = 0, \; B = \phi; \tag{117}$$

and rescaling $\varepsilon = \beta\delta(x) \to \eta = \beta\delta(x)e^{-\phi t}$. Eq. 115 becomes:

$$f(x,t) = \frac{e^{-x^2/(4Dt)}}{\sqrt{2\pi Dt}} + \beta \int_0^t \frac{e^{-x^2/4D(t-s)}e^{-\phi s}}{\sqrt{4D\pi(t-s)}}ds, \tag{118}$$

which, in terms of ρ reads as:

$$\rho(x,t) = f(x,t)e^{-\phi t} = \left[\frac{e^{-x^2/(4Dt)}}{\sqrt{2\pi Dt}} + \beta \int_0^t \frac{e^{-x^2/4D(t-s)}e^{-\phi s}}{\sqrt{4D\pi(t-s)}}ds\right]e^{-\phi t}. \tag{119}$$

B   General solution for the stationary case

The majority of the results I obtained in this thesis are related with the distribution of proteins at the equilibrium, therefore it's useful to find the steady-state solution of Eq. 103. Applying the transformation in Eq. 106, I derived the solution of Eq. 109, as described in Eq. 115. The steady state solution can be obtained by taking the limit of $\lim_{t\to\inf}(\rho(x,t))$.

The first term of Eq. 115, that depends on the intial condition, goes to zero in the limit, simplifying it to:

$$f(x) = \lim_{t\to\infty}\int_{-\infty}^{\infty}dy \int_0^t S(x-y,t-s)\eta(y,s)ds. \tag{120}$$

by imposing the inhomogenous term to be constant, that ensures to have a well defined limit: $\eta(x,t) = \varepsilon(x)e^{-Ax}e^{Bt}$, Eq. 120 became

$$f(x) = \int_{-\infty}^{\infty}dy\,\varepsilon(y)e^{-Ay}\lim_{t\to\infty}\frac{1}{\sqrt{4\pi D}}\int_0^t \frac{e^{-(x-y)^2/4D(t-s)}e^{Bs}}{\sqrt{(t-s)}}ds. \tag{121}$$

I performed the following change of variables:

$$g = \frac{|x-y|}{\sqrt{4D(t-s)}}$$

I expressed the nested integral of Eq. 121 as:

$$\frac{1}{\sqrt{4\pi D}}\int_0^t \frac{e^{-(x-y)^2/4D(t-s)}e^{Bs}}{\sqrt{(t-s)}}ds = \frac{|x-y|e^{Bt}}{2D\sqrt{\pi}}\int_{g(0)}^{g(t)}\frac{e^{-g^2}e^{-K/g^2}}{g^2}dg \qquad (122)$$

where $K = \frac{B|x-y|^2}{4D} > 0$. The integral in Eq. 122 is solvable and it is equal to:

$$\int_{g(0)}^{g(t)}\frac{e^{-g^2}e^{K/g^2}}{g^2}dg = \left.\frac{e^{-2\sqrt{K}}\sqrt{\pi}\left(-2+\mathrm{Erfc}\left[\frac{\sqrt{k}}{g}-g\right]+e^{4\sqrt{k}}\mathrm{Erfc}\left[\frac{\sqrt{k}}{g}+g\right]\right)}{4\sqrt{K}}\right|_{g(0)}^{g(t)} = G(g)|_{g(0)}^{g(t)} \qquad (123)$$

At this point calculated the left side of 123 for $s = 0$:

$$G(g(0)) = \frac{e^{-\sqrt{\frac{B}{D}}|x-y|}\sqrt{\pi}\left(-2+\mathrm{Erfc}\left[\frac{2Dt\sqrt{\frac{B}{D}}-|x-y|}{2\sqrt{Dt}}\right]+\mathrm{Erfc}\left[\frac{2Dt\sqrt{\frac{B}{D}}+|x-y|}{2\sqrt{Dt}}\right]\right)}{2\sqrt{\frac{B}{D}}|x-y|} \qquad (124)$$

I could not evaluate 123 directly at $s = t$, because $s = t$ is a discontinuity point, I therefore looked at the limit for $s \to t$:

$$\lim_{s \to t}G(g(s)) = 0. \qquad (125)$$

Therefore, I evaluated the limit for $t \to \infty$ of Eq. 123:

$$\lim_{t \to \infty}G(g)|_{g(0)}^{g(t)} = -\frac{e^{-\sqrt{\frac{B}{D}}|x-y|}\sqrt{\pi}}{\sqrt{\frac{B}{D}}|x-y|} \qquad (126)$$

Finally, plugging Eq. 126 into Eq. 122, and Eq. 122 into 121, lead to:

$$f(x) = -e^{Bt}\int_{-\infty}^{\infty}dy\,\varepsilon(y)\,e^{-Ay}\frac{e^{-\sqrt{\frac{B}{D}}|x-y|}}{\sqrt{4DB}} \qquad (127)$$

Finally I used Eq. 106 to express Eq. 127 in terms of ρ:

$$\rho(x,t) = f(x,t)e^{Ax-Bt} \tag{128}$$

which lead me to:

$$\rho(x) = \frac{-e^{Ax}}{\sqrt{4DB}} \int_{-\infty}^{\infty} dy\,\varepsilon(y)e^{-Ay}e^{-\sqrt{\frac{B}{D}}|x-y|} \tag{129}$$

B.1   No active transport, constant degradation, and translation at the soma

I applied Eq. 129 to a simple system, without a directional active transport, $v = 0$, with degradation constant throughout the whole dendrite, $\phi = \frac{\log(2)}{T_{1/2}}$, and protein translation only at the soma, $\varepsilon(x) = \beta\delta(x)$. Which translates to $B = \phi$, $A = 0$, and Eq. 129 becomes:

$$\rho(x) = \frac{-1}{\sqrt{4D\phi}} \int_{-\infty}^{\infty} dy\,\beta\delta(y)e^{-\sqrt{\frac{\phi}{D}}|x-y|}. \tag{130}$$

Integrating over the y leads to:

$$\rho(x) = \frac{-\beta e^{-\sqrt{\frac{\phi}{D}}|x|}}{2\sqrt{D\phi}}. \tag{131}$$

C   Alternative approach for the stationary case

In this thesis I am mostly interested in the stationary solution; for this reason, instead of finding a solution to Eq. 103 and then take the limit for big t, it's often easier to take the limit directly of Eq. 103. This allows to simplify the problem from a partial differential equation (PDE) to an ordinary differential equation (ODE):

$$0 = D\frac{\partial^2}{\partial x^2}\rho(x) - v\frac{\partial}{\partial x}\rho(x) - \tilde{\phi}\rho(x) + \varepsilon(x). \tag{132}$$

Using standard methods, I derived the general solution of 132:

$$\rho(x) = c_1 e^{xK_m} + c_2 e^{xK_p} + \frac{e^{-xK_m} \int_1^x e^{-tK_m} dt - e^{xK_p} \int_1^x e^{-tK_p} dt}{\sqrt{v^2 + 4D\phi}} \tag{133}$$

where

$$K_p = \frac{v + \sqrt{v^2 + 4D\phi}}{2D}, \tag{134}$$

and

$$K_m = \frac{v - \sqrt{v^2 + 4D\phi}}{2D}. \tag{135}$$

C.1   No active transport, constant degradation, and translation at the soma

I now considered the same system of the previous paragraph: a system without an active directional transport, with degradation constant throughout the whole dendrite and protein translation only at the soma: $v = 0$, and $\phi = \frac{\log(2)}{T_{1/2}}$. Which translates to $A = 0$ and $\varepsilon(x) = \beta\delta(x)$. Eq. 133 becomes:

$$\rho(x) = \frac{e^{-\sqrt{\frac{\phi}{D}}x}}{\sqrt{4d\phi}} \left(2\sqrt{D\phi} \left(c_1 e^{2x\sqrt{\frac{\phi}{D}}} + c_2 \right) + \beta\Theta(x) \left(1 - e^{2x\sqrt{\frac{\phi}{D}}} \right) \right) \tag{136}$$

where $\Theta(x)$ is the Heaviside step function and c_1 and c_2 are free parameters determined by the boundary conditions:

$$\lim_{x \to \infty} \rho(x) = 0 \tag{137}$$

$$\lim_{x \to -\infty} \rho(x) = 0. \tag{138}$$

imposing those two boundary fixes the free parameters:

$$c_1 = -\frac{\beta}{2} \tag{139}$$

$$c_2 = 0 \tag{140}$$

and Eq. 133 becomes:

$$\rho(x) = -\frac{\beta e^{-|x|\sqrt{\frac{\phi}{D}}}}{\sqrt{4D\phi}},$$ (141)

which is the same results I obtained in the previous section.

D Equilibrium solution for the stationary case on a finite domain

The main advantage of working directly with the diffusion equation at the equilibrium is that it allows handling different problems and boundary conditions in an easier and more intuitive way.

For my purposes, I needed to consider the solution of the diffusion equation on a finite domain, $x \in (0, L)$, because the length of a dendrite is often of the same order of magnitude of the diffusion length approximating the dendrite to an infinite one would be incorrect. While working on a linear dendrite without branches, or on a terminal dendrite I imposed a no flux-boundary condition at $x = L$:

$$\Phi(L) = -D \left.\frac{d\rho(x)}{dx}\right|_{x=L} + v\rho(L) = 0.$$ (142)

and a flux at the beginning of the dendrite equal to the income of proteins from the soma:

$$\Phi(0) = \beta$$ (143)

D.1 No active transport, constant degradation, and translation at the soma

If the proteins are synthetized in the soma, $\varepsilon(x) = 0$, $\Phi(0) = \beta$, they are not actively transported, $v = 0$, and they are recylced with constant rate throughout the dendritic arbor, $\phi = \frac{\log(2)}{T_{1/2}}$, the problem is described by the following system of differential equations:

$$\begin{cases} D\frac{\partial^2 \rho(x)}{\partial x^2} - \phi\rho = 0 \\ \Phi(0) = \beta \\ \Phi(L) = 0. \end{cases}$$ (144)

This system can be solved using standard methods:

$$\rho(x) = \frac{\beta}{\phi\lambda} \frac{\cosh[(L-x)/\lambda]}{\sinh[(L)/\lambda]} \tag{145}$$

where β is the somatic production rate. The number of proteins at the equilibrium in this scenario is:

$$N = \frac{\beta}{\phi}. \tag{146}$$

D.2   No active transport, constant degradation, and translation in the dendrite

If the proteins are synthetized in the dendritic arbor with a constant translation rate: $\varepsilon(x) = \frac{\beta}{L}$, no directional active transport $v = 0$, and constant degradation rate proportional to the protein density, $\phi = \frac{\log(2)}{T_{1/2}}$, the problem is described by the following system of differential equations:

$$\begin{cases} D\frac{\partial^2\rho(x)}{\partial x^2} - \phi\rho + \frac{\beta}{L} = 0 \\ \Phi(0) = 0 \\ \Phi(L) = 0. \end{cases} \tag{147}$$

This problem can be solved intuitively by observing that there is no flux at both termination of the dendrite, and that there are no terms in it that depends on the position, therefore the protein density ρ must be constant:

$$\rho = \frac{\beta}{L\phi}. \tag{148}$$

where the number of proteins in the dendrite is given by $N = \beta/\phi$.

D.3 No active transport, constant degradation, and local and central translation

If a fraction of the proteins is synthetized in the soma, and the ramining in the dendritic arbor, $\Phi(0) = \beta_s$ and $\varepsilon(x) = \frac{\beta_d}{L}$, with no direactional active transport $v = 0$, and constant degradation rate proportional to the protein density, $\phi = \frac{\log(2)}{T_{1/2}}$, the problem is described by the following system of differential equations:

$$\begin{cases} D\frac{\partial^2 \rho(x)}{\partial x^2} - \phi\rho + \frac{\beta_d}{L} = 0 \\ \Phi(0) = \beta_s \\ \Phi(L) = 0 \end{cases} \tag{149}$$

where the total production rate is $\beta = \beta_d + \beta_s$.

The problem can be written as a linear combination of the two problem descibed in Sec. D.1 and Sec. D.2, also its solution is a linear combination of the two:

$$\rho(x) = \frac{\beta_d}{\phi} + \frac{\beta_s}{\phi\lambda}\frac{\cosh[(L-x)/\lambda]}{\sinh[(L)/\lambda]}. \tag{150}$$

by calling $f_d = \beta_d/\beta$ and $f_s = \beta_s/\beta$, I expressed its solution in terms of the total production rate:

$$\rho(x) = \frac{\beta}{\phi}\left(f_d + \frac{f_s}{\lambda}\frac{\cosh[(L-x)/\lambda]}{\sinh[(L)/\lambda]}.\right). \tag{151}$$

where, once again the total number of proteins in the dendrite is $N = \beta/\phi$.

If one imposes $\beta_d = 0$ they would be in the limit where all the proteins are synthetized in the soma, Eq. 151 became to 145, conversely when all the proteins are syntetized in the dendrite, $\beta_s = 0$ and Eq. 151 becomes Eq. 148.

D.4 Active transport, constant degradation, and translation in the soma

If the proteins are synthetized in the soma, $\Phi(0) = \beta$, $\varepsilon(x) = 0$, if they are recycled with a constant degradation rate $\phi = \frac{\log(2)}{T_{1/2}}$, and they are actively transported resulting in an effective velocity v, the problem is described by the following system of differential equations:

$$\begin{cases} D\frac{\partial^2 \rho(x)}{\partial x^2} - v\frac{\partial \rho(x)}{\partial x} - \phi\rho = 0 \\ \Phi(0) = \beta \\ \Phi(L) = 0. \end{cases} \tag{152}$$

This system can be solved using standard methods, and lead to:

$$\rho(x) = \frac{\beta}{\phi} \frac{e^{-\frac{x(v+\Delta)}{2D}} \left(2D\phi\left(e^{\frac{L\Delta}{D}} + e^{\frac{x\Delta}{D}}\right) + ve^{\frac{L\Delta}{D}}(v+\Delta)\right)}{D\left(e^{L\Delta/D} - 1\right)(v+\Delta)}, \tag{153}$$

where $\Delta = \sqrt{v^2 + 4D\phi}$, and the total number of proteins in the dendrite is: $N = \frac{\beta}{\phi}$.

D.5 Active transport, constant degradation, and constant local translation

If the proteins are synthetized in the dendritic tree with a constant translation rate, $\Phi(0) =, \varepsilon(x) = \beta$, if they are recylced with constant degradation rate, $\phi = \frac{\log(2)}{T_{1/2}}$, and they are actively transported with in an effective velocity v, the problem is described by the following system of differential equations:

$$\begin{cases} D\frac{\partial^2 \rho(x)}{\partial x^2} - v\frac{\partial \rho(x)}{\partial x} - \phi\rho + \frac{\beta}{L} = 0 \\ \Phi(0) = 0 \\ \Phi(L) = 0. \end{cases} \tag{154}$$

This system can be solved using standard methods, and the protein distribution is:

$$\rho(x) = \frac{e^{-\frac{(v+\Delta)(L+x)}{2D}}}{\phi L(v+\Delta)}(A+B+C), \tag{155}$$

where

$$A = -2\beta v e^{\frac{Lv + \Delta x}{2D}} \tag{156}$$

$$B = +\beta e^{\frac{(v + \Delta)(L + x)}{2D}} (v + \Delta), \tag{157}$$

$$C = -\frac{2\beta e^{\frac{L(v + \Delta) + \Delta x}{2D}}}{\Delta - v} \left(e^{\frac{Lv - L\Delta}{2D}} - 1 \right) v \cosh\left[\frac{L\Delta}{2D}\right] \left(\Delta \cosh\left[\frac{\Delta(L - x)}{2D}\right] + v \sinh\left[\frac{\Delta(L - x)}{2D}\right] \right) \tag{158}$$

and $\Delta = \sqrt{v^2 + 4D\phi}$.

D.6   mRNA Translation

In the previous sections, I assumed that the mRNA translation happened only at the soma by imposing

$$\begin{cases} \varepsilon(x) = 0 \\ \Phi(0) = \beta \end{cases} . \tag{159}$$

or only in the dendritic arbor with constant translation rate by imposing

$$\begin{cases} \varepsilon(x) = \frac{\beta}{L} \\ \Phi(0) = 0 \end{cases} . \tag{160}$$

The first assumption follows the idea that all the mRNA are localized in the soma, and the second that they have a constant distribution in the dendrite. Here I studied a more general problem where the mRNA are actively transported in dendrites and the protein translation happens in the dendrites with a rate proportional to the mRNA density. This problem is descibed by the following set of differential equations:

$$
\begin{cases}
D_p \frac{\partial^2 \rho_p(x)}{\partial x^2} - \phi_p \rho_p(x) + \beta_p \rho_m(x) = 0 \\[2mm]
\Phi(\rho_p(0)) = 0 \\[2mm]
\Phi(\rho_p(L)) = 0 \\[2mm]
D_m \frac{\partial^2 \rho_m(x)}{\partial x^2} - v_m \frac{\partial \rho_m(x)}{\partial x} - \phi_m \rho_m(x) = 0 \\[2mm]
\Phi(\rho_m(0)) = \beta_m \\[2mm]
\Phi(\rho_m(L)) = 0
\end{cases}
. \tag{161}
$$

where the subscript p is the label for protein and m for mRNA. I solved first the differential equation for the mNRA, as I did in Eq. 153, and then I plugged it into the differential equation for the protein distribution. The total number of mRNA in the dendrite is $N_m = \frac{\beta_m}{\phi_m}$, while the number of protein is $N_p = \frac{N_m \beta_p}{\phi_p}$

The set of Eqs. 161 is analytically solvable, but its solution is not easily readable:

$$
\frac{e^{-\frac{x}{\lambda_p} - \frac{(L+x)(\Delta_m + v_m)}{2D_m}}}{2\phi_m \left(e^{\frac{L\Delta_m}{D_m}} - 1\right)\left((D_p\phi_m - D_m\phi_p)^2 - D_p\phi_p v_m^2\right)} A \tag{162}
$$

where:

$$
A = \frac{B_1 + B_2}{2\left(e^{\frac{L\Delta_m}{D_m}} - 1\right)} + \beta_m k e^{\frac{L\Delta_m}{2D_m}}\left(C_1 + C_2 + C_3\right), \tag{163}
$$

$$
\Delta_m = \sqrt{v_m^2 + 4D_m\phi_m}, \tag{164}
$$

$$
B_1 = D\left(e^{\frac{L\Delta_m}{D_m}} - 1\right)\left(2D_p\phi_m^2 - \phi_p\left(2D_m\phi_m + v_m^2\right)\right), \tag{165}
$$

$$
B_2 = D\left(2\phi_p v_m \Delta_m e^{\frac{L\left(2D_m\frac{1}{\lambda_p} + \Delta_m - v_m\right)}{2D_m}} - \phi_p v_m \Delta_m e^{\frac{L\Delta_m}{D_m}} - \phi_p v_m \Delta_m\right), \tag{166}
$$

$$
C_1 = -2v_m\sqrt{D_p\phi_p\left(4D_m\phi_m + v_m^2\right)}e^{\frac{(L+x)\Delta_m + v_m x}{2D_m} + L\frac{1}{\lambda_p}}, \tag{167}
$$

$$
C_2 = -D_p\phi_m\left((\Delta_m - v_m)e^{\frac{L\Delta_m}{D_m}} + (\Delta_m + v_m)e^{\frac{x\Delta_m}{D_m}}\right)e^{\frac{Lv_m}{2D_m} + x\frac{1}{\lambda_p}}, \tag{168}
$$

$$C_3 = D_m \phi_p \left((\Delta_m + v_m) e^{\frac{L\Delta_m}{D_m}} + (\Delta_m - v_m) e^{\frac{x\Delta_m}{D_m}} \right) e^{\frac{Lv_m}{2D_m} + x\frac{1}{\lambda_p}}, \tag{169}$$

and

$$D = \beta_m k \lambda_p \left(e^{\frac{2L}{\lambda_p}} + e^{\frac{2x}{\lambda_p}} \right) \left(\coth \left(\frac{L}{\lambda_p} \right) - 1 \right) \left(e^{\frac{L(3\Delta_m + v_m) + x(\Delta_m + v_m)}{2D_m}} - e^{\frac{(L+x)(\Delta_m + v_m)}{2D_m}} \right). \tag{170}$$

D.7   Single branch

In this section I showed the explicit solution for the diffusion equation of a branched dendrites, with a single branch. In Sec. 2.5 I derived the six boundary conditions for a branching dendrite:

$$\begin{cases} \Phi\left[\rho_0\left(0\right)\right] = \beta, \\[2mm] \Phi\left[\rho_1\left(L_1\right)\right] = 0, \\[2mm] \Phi\left[\rho_2\left(L_2\right)\right] = 0, \\[2mm] \Phi\left[\rho_0\left(L_0\right)\right] = \Phi\left[\rho_1\left(0\right)\right] + \Phi\left[\rho_2\left(0\right)\right], \\[2mm] \rho_1\left(0\right) = \frac{f_1}{f_0}\rho_0\left(0\right), \\[2mm] \rho_2\left(0\right) = \frac{f_2}{f_0}\rho_0\left(0\right), \end{cases} \tag{171}$$

where $f_i = \frac{R_i^\gamma}{R_0^\gamma + R_1^\gamma + R_2^\gamma}$, and $\gamma = 1$ for surface diffusion, and $\gamma = 2$ for cytoplasmic diffusion.

Assuming that the proteins don't have any net effective velocity, $\Phi\left[\rho_i\left(x\right)\right] = -D\frac{\partial\rho(x)}{\partial x}$, and the solution for the three dendrites are:

$$\rho_0\left(x\right) = N\frac{f_0 \cosh\left[\frac{L_0 - x}{\lambda}\right]}{\lambda\left(f_0 \sinh\left[\frac{L_0}{\lambda}\right] + f_1 \tanh\left[\frac{L_1}{\lambda}\right] + f_2 \tanh\left[\frac{L_2}{\lambda}\right]\right)},$$

$$\rho_1\left(x\right) = N\frac{f_1 \cosh\left[\frac{L_1 - x}{\lambda}\right]}{\lambda\left(f_1 \sinh\left[\frac{L_1}{\lambda}\right] + \cosh\left[\frac{L_1}{\lambda}\right]\left(f_0 \sinh\left[\frac{L_0}{\lambda}\right] + f_2 \tanh\left[\frac{L_2}{\lambda}\right]\right)\right)},$$

$$\rho_2\left(x\right) = N\frac{f_2 \cosh\left[\frac{L_2 - x}{\lambda}\right]}{\lambda\left(f_2 \sinh\left[\frac{L_2}{\lambda}\right] + \cosh\left[\frac{L_2}{\lambda}\right]\left(f_0 \sinh\left[\frac{L_0}{\lambda}\right] + f_1 \tanh\left[\frac{L_1}{\lambda}\right]\right)\right)}. \tag{172}$$

E Full Neuron Simulation: swc Selection

To select the 64 pyramidal neurons I used in these simulations, I used the following protocol:

1. I selected all the rat hippocampal pyramidal neurons with reconstructed dendrites, 5813 morphologies,

2. I selected only morphologies where the distal dendrites were densely reconstructed, by imposing to have at least 75 branches after $d = 900 \, \mu m$.

3. For a similar reason, I imposed that the total length of the pyramidal neurons was at least 1500 μm,

4. At least 10% of the total length of the dendrite is located in the final 10% of the dendrite.

Following these requirements, I reduced the total number of pyramidal morphologies from more than 5813 to 64.

Selecting the morphologies for Purkinje and granule neurons was easier; due to their more limited spatial extension, having completely reconstructed neurons is more common, and I directly selected the morphologies I used.

F Cultured Hippocampal Neurons

In this section, I explained the methods used by our collaborator A.S. Hafner to image the fluorescence of GFP and GFP::Nlg-1 in cultured hippocampal neurons. Then I explained the protocol I used to analyze the fluorescence in the surrounding of a dendritic branch.

F.1 Cultured Neurons: Preparation

The detailed description of the methods used to prepare the hippocampal cultures, see [88, 89]. Here I shortly summarized it.

Our collaborator first dissected the hippocampus from both male and female rat pups of 0 to 1 days old. The neurons were dissociated using papain (Sigma) and placed on a plate with a density of 30 to 40 $\times 10^3$cells/cm^2, on Petri-dishes whose bottom-glass was coated with poly-d-lysine. The neurons in the dishes were kept in a humidified atmosphere at 37°C, and 5% CO_2 for 8 days. The neuron was kept in the growth medium Neurobasal-A, with two common neuronal cell supplements: B27 and GlutaMAX-I. After seven days of this in vitro preparation, half of the hippocampal neurons were transfected, using the Effectene (QIAGEN) guidelines, with plasmids coding for GFP (Green Fluorescent Protein), and the other half with plasmids coding for GFP::Nlg-1 (Neuroligin-1, a surface protein that mediates the creation and maintenance of neuronal synapses).

After 13 hours, the cells were fixated in vitro using paraformaldehyde. Additionally, to ease the imaging, the nuclei were stained for 1 minute in PBS with DAPI. The fixated cells have been kept at 4 C in PBS for less than four days after fixation before being imaged.

F.2   Selection of Hippocampal Branches

The images provided to us by our collaborator are structured as overlayed layers, *stacks*. The number of stacks varies from neuron to neuron, from 27 to 34. These images were analyzed using the image processing package Fiji.

I summed the fluorescence across the stacks to get its projection on the (horizontal) X-Y plane, see Fig. 31-A. Then, from the projection of the fluorescence, I extracted the two categories of information that I needed, the radii of the dendrites and the fluorescence in the proximity of each branch.

F.3   Branching Fluorescence and Fluorescence Ratio

For each branch, I identified ordered triplets of mother and two daughter dendrites, and among them, I identified 31 *clean* branches for GFP-expressing neurons and 39 for the GFP::Nlg-1 ones.

Clean branches, see Fig. 31-B, are branches that don't fall in the following categories:

- Have excessive background noise, see Fig. 31-C

- Have synaptic buttons too close to the dendrite, see Fig. 31-D, but not Fig. 31-B, in B the spine is far enough from the dendrite.

- Have more than 2 daughter dendrites, see Fig. 31-E

- Have overlapping dendrites or axons, see Fig. 31-F.

I isolated a narrow area around the dendrite for each clean branch, which I referred to as ROIs. Measuring the ROIs allowed me to quantified the spatial dependency of the fluorescence for each branch. All the ROIs have been selected with the same orientation for consistency, pointing away from the soma.

The measure for each of the three ROIs is the spatial fluorescence $f(x)$, where $x \in (0, L_i)$. For obvious reasons, the maximum value of L_i varies from dendrite to dendrite, and to compare the fluorescence signal, I limited my analysis to the smaller of the three, which I referred to as L.

Because of the tapering that happens immediately after the branch, one might be interested in limiting the analysis to the dendrites distant m from the center of the branch, and due to the dendritic tapering that it occurs at long distances, one might want to limit the analysis to dendrtitic compartment that are close to the center of the branch. I called the distance from the center of the dendrite $m + \Delta$. Analyzing these results for different choices of these two parameters allows checking the robustness of the analysis.

I therefore measured the integrated fluorescence between m and $m + \Delta$:

$$F_i(m, \Delta) = \int_m^{m+\Delta} f_i(x)\, dx. \tag{173}$$

In Eq. 93, I defined the fluorescent ratio as the ratio of the integrated fluorescence as defined in Eq. 173. In Fig. 32 I showed the distribution of Q_F for multiple choices of m and Δ. In Fig. 22-E I showed the mean and s.e.m. of both Q_F^S and Q_F^C for multiple choices of m and Δ.

F.4 Branching Radii

To extract the radius of each mother and daughter dendrite, I started from the Z-stacked image, like the one in 31-A, and for each of the three dendrites, I measured the diameter four times at regular intervals, orthogonally to the dendrite, and defined the radius as the half of the mean of those four measurements.

G Table: Protein Diffusion length

In this section, I discussed the listed diffusion length for different proteins of interest, and we discuss the main techniques used to determine their diffusion coefficient and half-life. A review of the strengths and weaknesses of the different techniques can be found here [90].

G.1 Stokes-Einstein Relationship: SER

The first method in the list used to determine the diffusion coefficient is to extrapolate it accordingly to the Stokes-Einstein Relationship, [91]. The SER sets the following relations for the diffusion coefficient:

$$D = \frac{k_B T}{C \pi \eta \sigma},$$
(174)

where k_B is the Boltzman constant, η is the shear viscosity of the medium, and σ is the diameter of the diffusing particle. The main limitation of this equation is that it is defined for non-interacting and perfectly spherical particles, while proteins often interact with each other, and they are not spherical. For this reason, other techniques are to be preferred to measure the diffusion coefficient. The most common are single-particle tracking, fluorescence correlation, and fluorescence recovery after photobleaching.

G.2   Single Particle Tracing: SPT

Single-particle tracing is the most direct way to determine the diffusion coefficient of a protein. First, one needs to make that protein visible and traceable, for example, using quantum dots, and record its position over time. Then, analyzing its trajectory, one can determine the mean square displacement, and if it scales linearly with time, it can be used to determine the diffusion coefficient of the protein of interest. For more details about the quantum dots technique used to trace single proteins in dendrites, see [92, 83].

G.3   Fluorescence Correlation: FCS

Fluorescence Correlation Spectroscopy, FCS, is a technique introduced in the first half of the 1970s in [93, 94]. The underlying idea is to record with a high temporal resolution the fluorescence signal of a mobile population of proteins over a time of tens of seconds. The autocorrelation of the fluorescence is used to determine the rate of protein to move out, and in the recording area and therefore the diffusion coefficient:

$$D_{eff} = \sqrt{\frac{\omega_0^2}{4\tau_D}}. \tag{175}$$

where ω_0 represents the radius of the laser used to excite the fluorophores, and τ_D the decay time of the autocorrelation function.

G.4   Fluorescence Recovery After Photobleaching: FRAP

Confocal fluorescence recovery after photobleaching is an easy method to estimate the mobility of diffusive proteins as described in [95] and first introduced in [96]. In synthesis during the FRAP procedure, a segment of the cell, or in this case of the dendrite, is photobleached, and the evolution of the out-of-equilibrium fluorescence profile is analyzed in time. The profile is then fitted against the 1, or 2-dimensional diffusion equation with initial condition depending on the

intensity profile of the laser used to photobleach the fluorophores to obtain the best estimation of the diffusion coefficient.
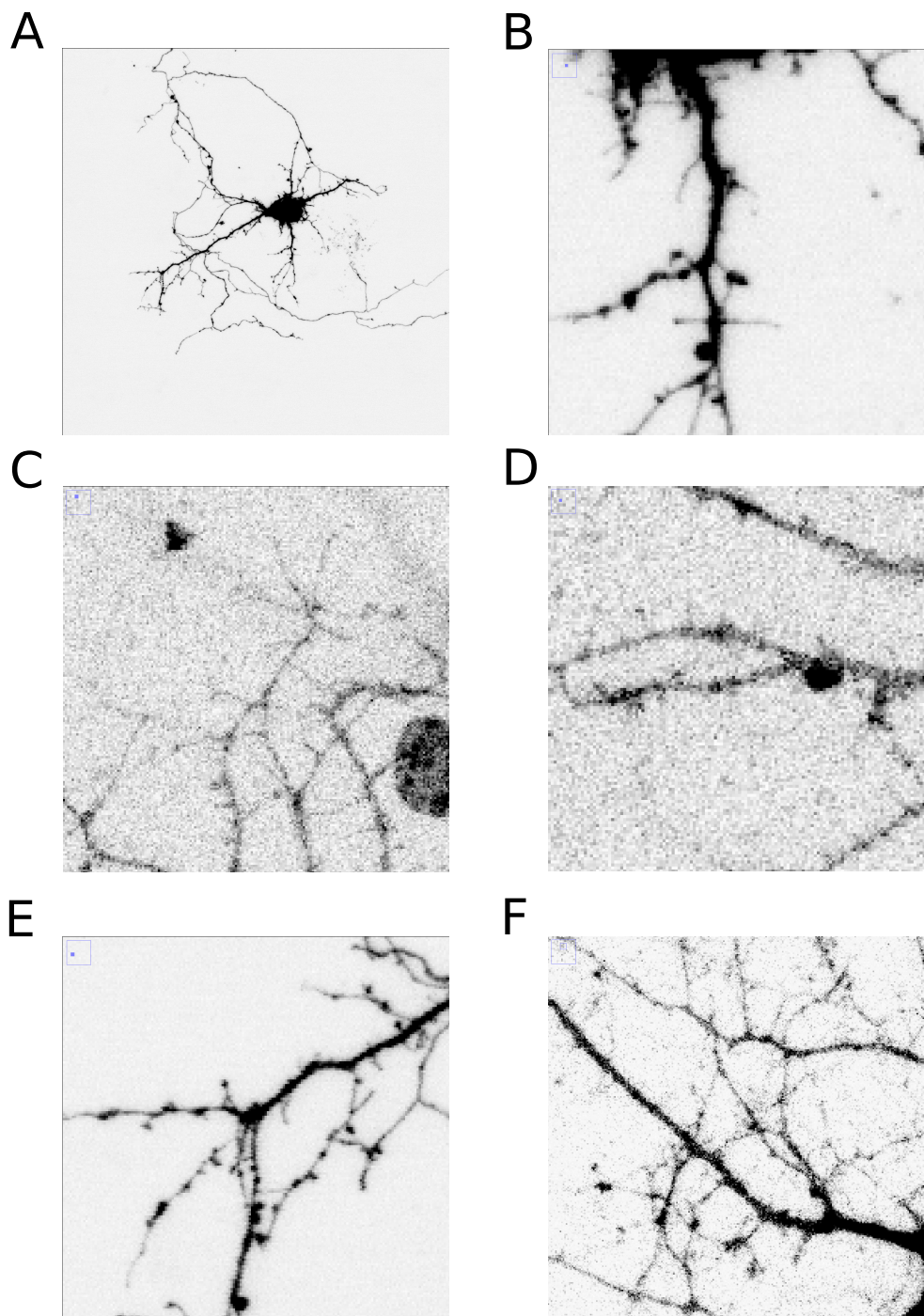
Figure 31: **Examples of clean and not clean Branches** In this figure I showed an example of a clean branch and of several not-clean branches. A) Overview of a cultured neuron, with clean and not-clean branches. B) Clean Branch, despite the synaptic button attached to the mother dendrite, its distance from it is enough to allow me to select only the mother dendrite. C) Not-Clean branch because the background noise is too high. D) Not-Clean branch, the synaptic button is too close to the mother dendrite to be isolated. F) Not-Clean branch: the branch splits into more than two daughter dendrites. F) Not-Clean branch: there is an overlap of neuronal processes, and it is not possible to isolate one of them from the other.

Figure 32: **Cultured Neurons: overview of the protein ratio distribution** In this figure I showed the distribution of the protein ratio for multiple choices of $m = 0, 1, 2, 3, 4\mu m$ and $\Delta = 1, 2, 3, 4\mu m$. In the title of each subplot there is the value of m and Δ is specified and also the number of GFP and NlG branches that are long enough to be considered is specified.

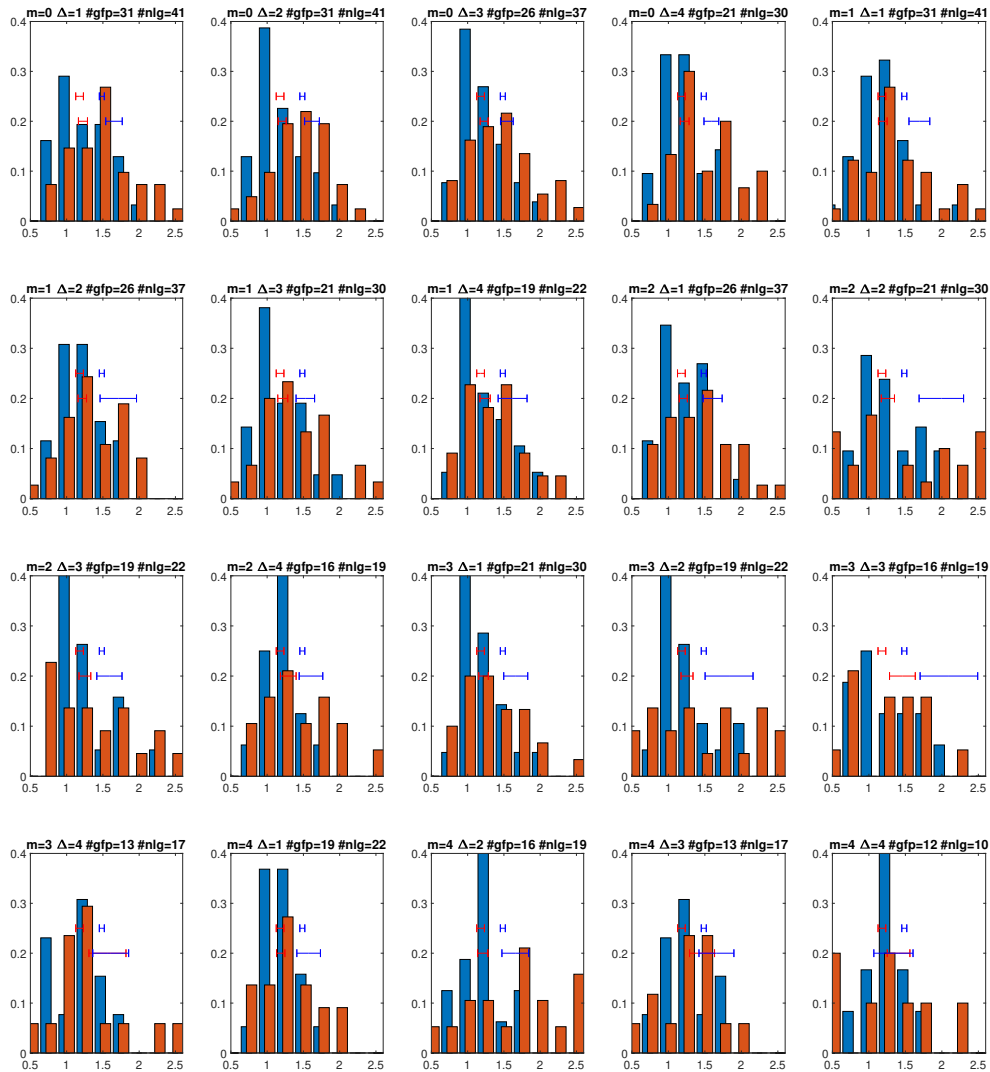| $\lambda[\mu m^2]$	**Protein Name**	$\tau_{1/2}$	Half-Life Link	$D[\mu^2/s]$	Diffusion Link	Technique
687	Peroxiredoxin (half-life -3, diffusion -4)	7.3	[8]	0.52	[97]	SER
451	Plexin-A	6.5	[8]	0.25	[98]	FCS
97	Grm5 (Metabotropic glutamate receptor 5)	3.0	[8]	0.025	[99]	SPT
314	CamKII	7.2	[8]	0.111	[100]	SPT
76	Synaptophysin	9.2	[8]	0.005	[36]	FCS
313	L1CAM (Neural cell adhesion molecule L1)	7.1	[8]	0.11	[101]	SPT
104	Clathrin-L (b for half-life, c for Diffusion coeff.)	9.1	[8]	0.0096	[36]	FCS
111.6	GluA1-AMPAR	2.0	[102]	0.005	[103]	SPT
473	GABAAR subunit alpha 2	5.0	[8]	0.36	[103]	SPT
78	potassium channel Kv1.3	0.2	[104]	0.31	[103]	SPT
891	Syt7 (Synaptotagmin 7)	7.0	[8]	0.91	[105]	SPT
73	Neurexin	3.6	[8]	0.012	[106]	SPT
168	AChE (acetylcholinesterase)	2.8	[107]	0.08	[108]	FRAP
345	VAMP2–pHluorin	6.8	[8]	0.14	[109]	SPT
3361	Calbindin	4.5	[8]	20	[110]	FRAP
2138	GAP43(S41A) (Neuromodulin)	17.5	[8]	2.09	[111]	FCS
6163	Microtubule-Associated Protein Tau	101.6	[8]	3	[112]	FRAP
987	Phosphatidylserine	22.0	[113]	0.355	[114]	FRAP and SPT
204	Actin	8.4	[8]	0.04	[115]	FRAP
4256	Rho-associated protein kinase 2	5.6	[8]	26	[116]	FCS
103	GABA-A subunit α1	3.9	[8]	0.022	[117]	SPT
302	GABA-A subunit α5	7.6	[8]	0.097	[118]	SPT
15	GluN2B	3.4	[8]	0.00053	[119]	SPT
2111	Phosphoinositide phospholipase C	8.5	[8]	4.2	[120]	FCS
3710	Glutamine synthetase	3.5	[8]	32	[121]	FCS
583	Vesicle-associated membrane protein 2	6.8	[8]	0.4	[122]	SPT

Table 11: Protein diffusion length: The first column contains the diffusion length, the second the name of the protein, the third and fourth contain the half-life and relative reference. In the fifth and sixth columns, the diffusion coefficient and relative reference. The last column is the technique used to measure the diffusion coefficient: Stokes-Einstein Relationship (SER), Fluorescence Correlation Spectroscopy (FCS), or Single Particle Tracking (SPT)

Bibliography

[1] P. C. Bressloff and J. M. Newby, "Stochastic models of intracellular transport," *Reviews of Modern Physics*, vol. 85, no. 1, p. 135, 2013.

[2] A. G. Otopalik, M. L. Goeritz, A. C. Sutton, T. Brookings, C. Guerini, and E. Marder, "Sloppy morphological tuning in identified neurons of the crustacean stomatogastric ganglion," *Elife*, vol. 6, p. e22352, 2017.

[3] G. A. Ascoli, D. E. Donohue, and M. Halavi, "Neuromorpho. org: a central resource for neuronal morphologies," *Journal of Neuroscience*, vol. 27, no. 35, pp. 9247–9251, 2007.

[4] E. Agliari, D. Cassi, L. Cattivelli, and F. Sartori, "Two-particle problem in comblike structures," *Physical Review E*, vol. 93, no. 5, p. 052111, 2016.

[5] M. Weigand, F. Sartori, and H. Cuntz, "Universal transition from unstructured to structured neural maps," *Proceedings of the National Academy of Sciences*, vol. 114, no. 20, pp. E4057–E4064, 2017.

[6] Y. Fonkeu, N. Kraynyukova, A.-S. Hafner, L. Kochen, F. Sartori, E. M. Schuman, and T. Tchumatchenko, "How mrna localization and protein synthesis sites influence dendritic protein distribution and dynamics," *Neuron*, vol. 103, no. 6, pp. 1109–1122, 2019.

[7] F. Sartori, A.-S. Hafner, A. Karimi, A. Nold, Y. Fonkeu, E. M. Schuman, and T. Tchumatchenko, "Statistical laws of protein motion in neuronal dendritic trees," *Cell reports*, vol. 33, no. 7, p. 108391, 2020.

[8] A. R. Dörrbaum, L. Kochen, J. D. Langer, and E. M. Schuman, "Local and global influences on protein turnover in neurons and glia," *Elife*, vol. 7, p. e34202, 2018.

[9] E. R. Kandel, J. H. Schwartz, T. M. Jessell, S. Siegelbaum, A. J. Hudspeth, and S. Mack, *Principles of neural science*, vol. 4. McGraw-hill New York, 2000.

[10] A. Nold, D. Batulin, K. Birkner, S. Bittner, and T. Tchumatchenko, "A model of neuron-glia crosstalk explains stages of neural tissue resilience," *bioRxiv*, p. 828053, 2019.

[11] H. Kang and E. M. Schuman, "A requirement for local protein synthesis in neurotrophin-induced hippocampal synaptic plasticity," *Science*, vol. 273, no. 5280, pp. 1402–1406, 1996.

[12] T. Tyrrell and D. Willshaw, "Cerebellar cortex: its simulation and the relevance of marr's theory," *Philosophical Transactions of the Royal Society of London. Series B: Biological Sciences*, vol. 336, no. 1277, pp. 239–257, 1992.

[13] P. Valverde, "Apical dendritic spines of the visual cortex and light deprivation in the mouse," *Experimental brain research*, vol. 3, no. 4, pp. 337–352, 1967.

[14] G. Stuart, N. Spruston, and M. Häusser, *Dendrites*. Oxford University Press, 2016.

[15] H. Cuntz, F. Forstner, A. Borst, and M. Hausser, "One rule to grow them all: a general theory of neuronal branching and its practical application," *PLoS Comput Biol*, vol. 6, no. 8, p. e1000877, 2010.

[16] C. M. Goss, "Gray's anatomy of the human body," *Academic Medicine*, vol. 35, no. 1, p. 90, 1960.

[17] A. Perez-Alvarez, S. Yin, C. Schulze, J. A. Hammer, W. Wagner, and T. G. Oertner, "Endoplasmic reticulum visits highly active spines and prevents runaway potentiation of synapses," *Nature communications*, vol. 11, no. 1, pp. 1–10, 2020.

[18] J. Spacek and K. M. Harris, "Three-dimensional organization of cell adhesion junctions at synapses and dendritic spines in area ca1 of the rat hippocampus," *Journal of Comparative Neurology*, vol. 393, no. 1, pp. 58–68, 1998.

[19] O. A. Ramírez, S. Härtel, and A. Couve, "Location matters: the endoplasmic reticulum and protein trafficking in dendrites," *Biological research*, vol. 44, no. 1, pp. 17–23, 2011.

[20] Y. D. Kulik, D. J. Watson, G. Cao, M. Kuwajima, and K. M. Harris, "Structural plasticity of dendritic secretory compartments during ltp-induced synaptogenesis," *Elife*, vol. 8, p. e46356, 2019.

[21] J. Spacek and K. M. Harris, "Three-dimensional organization of smooth endoplasmic reticulum in hippocampal ca1 dendrites and dendritic spines of the immature and mature rat," *Journal of Neuroscience*, vol. 17, no. 1, pp. 190–203, 1997.

[22] T. Mitchison and M. Kirschner, "Dynamic instability of microtubule growth," *nature*, vol. 312, no. 5991, pp. 237–242, 1984.

[23] A. Desai and T. J. Mitchison, "Microtubule polymerization dynamics," *Annual review of cell and developmental biology*, vol. 13, no. 1, pp. 83–117, 1997.

[24] M. Dogterom and B. Yurke, "Measurement of the force-velocity relation for growing microtubules," *Science*, vol. 278, no. 5339, pp. 856–860, 1997.

[25] F. Gittes, B. Mickey, J. Nettleton, and J. Howard, "Flexural rigidity of microtubules and actin filaments measured from thermal fluctuations in shape.," *The Journal of cell biology*, vol. 120, no. 4, pp. 923–934, 1993.

[26] M. Mirigian, K. Mukherjee, S. L. Bane, and D. L. Sackett, "Measurement of in vitro microtubule polymerization by turbidity and fluorescence," *Methods in cell biology*, vol. 115, pp. 215–229, 2013.

[27] J. Löwe, H. Li, K. Downing, and E. Nogales, "Refined structure of α β-tubulin at 3.5 å resolution," *Journal of molecular biology*, vol. 313, no. 5, pp. 1045–1057, 2001.

[28] M. Burute and L. C. Kapitein, "Cellular logistics: unraveling the interplay between microtubule organization and intracellular transport," *Annual review of cell and developmental biology*, vol. 35, pp. 29–54, 2019.

[29] L. C. Kapitein, M. A. Schlager, M. Kuijpers, P. S. Wulf, M. van Spronsen, F. C. MacKintosh, and C. C. Hoogenraad, "Mixed microtubules steer dynein-driven cargo transport into dendrites," *Current biology*, vol. 20, no. 4, pp. 290–299, 2010.

[30] B. Wickstead and K. Gull, "Dyneins across eukaryotes: a comparative genomic analysis," *Traffic*, vol. 8, no. 12, pp. 1708–1721, 2007.

[31] R. Milo, "What is the total number of protein molecules per cell volume? a call to rethink some published values," *BioEssays*, vol. 35, no. 12, pp. 1050–1055, 2013.

[32] V. Braitenberg and A. Schüz, *Cortex: statistics and geometry of neuronal connectivity.* Springer Science & Business Media, 2013.

[33] J. L. Twiss and M. Fainzilber, "Ribosomes in axons–scrounging from the neighbors?," *Trends in cell biology*, vol. 19, no. 5, pp. 236–243, 2009.

[34] A. Fick, "Ueber diffusion," *Annalen der Physik*, vol. 170, no. 1, pp. 59–86, 1855.

[35] C. W. Mullineaux, A. Nenninger, N. Ray, and C. Robinson, "Diffusion of green fluorescent protein in three cell environments in escherichia coli," *Journal of bacteriology*, vol. 188, no. 10, p. 3442, 2006.

[36] I. Pelassa, C. Zhao, M. Pasche, B. Odermatt, and L. Lagnado, "Synaptic vesicles are "primed" for fast clathrin-mediated endocytosis at the ribbon synapse," *Frontiers in molecular neuroscience*, vol. 7, p. 91, 2014.

[37] X. Chen, J. M. Levy, A. Hou, C. Winters, R. Azzam, A. A. Sousa, R. D. Leapman, R. A. Nicoll, and T. S. Reese, "Psd-95 family maguks are essential for anchoring ampa and nmda

receptor complexes at the postsynaptic density," *Proceedings of the National Academy of Sciences*, vol. 112, no. 50, pp. E6983–E6992, 2015.

[38] L. Matt, K. Kim, A. C. Hergarden, T. Patriarchi, Z. A. Malik, D. K. Park, D. Chowdhury, O. R. Buonarati, P. B. Henderson, Ç. G. Saraç, *et al.*, "α-actinin anchors psd-95 at postsynaptic sites," *Neuron*, vol. 97, no. 5, pp. 1094–1109, 2018.

[39] W. Han, Y.-K. Ng, D. Axelrod, and E. S. Levitan, "Neuropeptide release by efficient recruitment of diffusing cytoplasmic secretory vesicles," *Proceedings of the National Academy of Sciences*, vol. 96, no. 25, pp. 14577–14582, 1999.

[40] M. D. Ehlers, M. Heine, L. Groc, M.-C. Lee, and D. Choquet, "Diffusional trapping of glur1 ampa receptors by input-specific synaptic activity," *Neuron*, vol. 54, no. 3, pp. 447–460, 2007.

[41] J. Triesch and A.-S. Hafner, "Competition for a limited supply of synaptic building blocks predicts multiplicative synaptic normalization and heterosynaptic plasticity," *bioRxiv*, p. 166819, 2017.

[42] D. Choquet and A. Triller, "The dynamic synapse," *Neuron*, vol. 80, no. 3, pp. 691–703, 2013.

[43] M. A. Jakobs, A. Dimitracopoulos, and K. Franze, "Kymobutler, a deep learning software for automated kymograph analysis," *Elife*, vol. 8, p. e42288, 2019.

[44] M. A. Welte, S. P. Gross, M. Postner, S. M. Block, and E. F. Wieschaus, "Developmental regulation of vesicle transport in drosophila embryos: forces and kinetics," *Cell*, vol. 92, no. 4, pp. 547–557, 1998.

[45] T. Duke and S. Leibler, "Motor protein mechanics: a stochastic model with minimal mechanochemical coupling," *Biophysical journal*, vol. 71, no. 3, pp. 1235–1247, 1996.

[46] F. Jülicher, A. Ajdari, and J. Prost, "Modeling molecular motors," *Reviews of Modern Physics*, vol. 69, no. 4, p. 1269, 1997.

[47] M. J. Schnitzer, K. Visscher, and S. M. Block, "Force production by single kinesin motors," *Nature cell biology*, vol. 2, no. 10, pp. 718–723, 2000.

[48] M. J. Schnitzer and S. M. Block, "Kinesin hydrolyses one atp per 8-nm step," *Nature*, vol. 388, no. 6640, pp. 386–390, 1997.

[49] M. S. Song, H. C. Moon, J.-H. Jeon, and H. Y. Park, "Neuronal messenger ribonucleoprotein transport follows an aging lévy walk," *Nature communications*, vol. 9, no. 1, pp. 1–8, 2018.

[50] J. Eberwine, K. Miyashiro, J. E. Kacharmina, and C. Job, "Local translation of classes of mrnas that are targeted to neuronal dendrites," *Proceedings of the National Academy of Sciences*, vol. 98, no. 13, pp. 7080–7085, 2001.

[51] S. J. Tang and E. M. Schuman, "Protein synthesis in the dendrite," *Philosophical Transactions of the Royal Society of London. Series B: Biological Sciences*, vol. 357, no. 1420, pp. 521–529, 2002.

[52] C. R. Bramham and D. G. Wells, "Dendritic mrna: transport, translation and function," *Nature Reviews Neuroscience*, vol. 8, no. 10, pp. 776–789, 2007.

[53] J. L. Dynes and O. Steward, "Dynamics of bidirectional transport of arc mrna in neuronal dendrites," *Journal of Comparative Neurology*, vol. 500, no. 3, pp. 433–447, 2007.

[54] O. Steward, C. S. Wallace, G. L. Lyford, and P. F. Worley, "Synaptic activation causes the mrna for the ieg arc to localize selectively near activated postsynaptic sites on dendrites," *Neuron*, vol. 21, no. 4, pp. 741–751, 1998.

[55] A.-B. Shyu, J. G. Belasco, and M. E. Greenberg, "Two distinct destabilizing elements in the c-fos message trigger deadenylation as a first step in rapid mrna decay.," *Genes & development*, vol. 5, no. 2, pp. 221–231, 1991.

[56] S. Camper, R. Albers, J. Coward, and F. Rottman, "Effect of undermethylation on mrna cytoplasmic appearance and half-life.," *Molecular and cellular biology*, vol. 4, no. 3, p. 538, 1984.

[57] K. S. Kosik, "Life at low copy number: how dendrites manage with so few mrnas," *Neuron*, vol. 92, no. 6, pp. 1168–1180, 2016.

[58] D. Ben-Avraham and S. Havlin, *Diffusion and reactions in fractals and disordered systems*. Cambridge university press, 2000.

[59] K. Speckner, L. Stadler, and M. Weiss, "Anomalous dynamics of the endoplasmic reticulum network," *Physical Review E*, vol. 98, no. 1, p. 012406, 2018.

[60] T. Sandev, R. Metzler, and Ž. Tomovski, "Fractional diffusion equation with a generalized riemann–liouville time fractional derivative," *Journal of physics A: mathematical and theoretical*, vol. 44, no. 25, p. 255203, 2011.

[61] A. Telcs, "Random walks on graphs, electric networks and fractals," *Probability theory and related fields*, vol. 82, no. 3, pp. 435–449, 1989.

[62] X. Y. Zhou, "Resistance dimension, random walk dimension and fractal dimension," *Journal of Theoretical Probability*, vol. 6, no. 4, pp. 635–652, 1993.

[63] E. Barkai, "Fractional fokker-planck equation, solution, and application," *Physical Review E*, vol. 63, no. 4, p. 046118, 2001.

[64] J. Stoer and R. Bulirsch, *Introduction to numerical analysis*, vol. 12. Springer Science & Business Media, 2013.

[65] S. Linge and H. P. Langtangen, "Diffusion equations," in *Finite Difference Computing with PDEs*, pp. 207–322, Springer, 2017.

[66] M. A. Smith, G. C. Ellis-Davies, and J. C. Magee, "Mechanism of the distance-dependent scaling of schaffer collateral synapses in rat ca1 pyramidal neurons," *The Journal of physiology*, vol. 548, no. 1, pp. 245–258, 2003.

[67] J.-i. Tanaka, M. Matsuzaki, E. Tarusawa, A. Momiyama, E. Molnar, H. Kasai, and R. Shigemoto, "Number and density of ampa receptors in single synapses in immature cerebellum," *Journal of Neuroscience*, vol. 25, no. 4, pp. 799–807, 2005.

[68] M. Matsuzaki, G. C. Ellis-Davies, T. Nemoto, Y. Miyashita, M. Iino, and H. Kasai, "Dendritic spine geometry is critical for ampa receptor expression in hippocampal ca1 pyramidal neurons," *Nature neuroscience*, vol. 4, no. 11, pp. 1086–1092, 2001.

[69] A. D. Bird and H. Cuntz, "Optimal current transfer in dendrites," *PLoS computational biology*, vol. 12, no. 5, p. e1004897, 2016.

[70] W. Rall, "Membrane time constant of motoneurons," *Science*, vol. 126, no. 3271, pp. 454–454, 1957.

[71] W. Rall, "Branching dendritic trees and motoneuron membrane resistivity," *Experimental neurology*, vol. 1, no. 5, pp. 491–527, 1959.

[72] G. A. Ascoli and J. L. Krichmar, "L-neuron: a modeling tool for the efficient generation and parsimonious description of dendritic morphology," *Neurocomputing*, vol. 32, pp. 1003–1011, 2000.

[73] A. Karimi, J. Odenthal, F. Drawitsch, K. M. Boergens, and M. Helmstaedter, "Cell-type specific innervation of cortical pyramidal cells at their apical dendrites," *Elife*, vol. 9, p. e46876, 2020.

[74] J. C. Dalrymple-Alford, B. Harland, E. A. Loukavenko, B. Perry, S. Mercer, D. A. Collings, K. Ulrich, W. C. Abraham, N. McNaughton, and M. Wolff, "Anterior thalamic nuclei lesions and recovery of function: Relevance to cognitive thalamus," *Neuroscience & Biobehavioral Reviews*, vol. 54, pp. 145–160, 2015.

[75] H. Anwar, C. J. Roome, H. Nedelescu, W. Chen, B. Kuhn, and E. De Schutter, "Dendritic diameters affect the spatial variability of intracellular calcium dynamics in computer models," *Frontiers in cellular neuroscience*, vol. 8, p. 168, 2014.

[76] H. Bao, B. Asrican, W. Li, B. Gu, Z. Wen, S.-A. Lim, I. Haniff, C. Ramakrishnan, K. Deisseroth, B. Philpot, *et al.*, "Long-range gabaergic inputs regulate neural stem cell quiescence and control adult hippocampal neurogenesis," *Cell stem cell*, vol. 21, no. 5, pp. 604–617, 2017.

[77] X. R. Chen, N. Heck, A. M. Lohof, C. Rochefort, M.-P. Morel, R. Wehrlé, M. Doulazmi, S. Marty, V. Cannaya, H. X. Avci, *et al.*, "Mature purkinje cells require the retinoic acid-related orphan receptor-α (rorα) to maintain climbing fiber mono-innervation and other adult characteristics," *Journal of Neuroscience*, vol. 33, no. 22, pp. 9546–9562, 2013.

[78] G. L. Collingridge, J. T. Isaac, and Y. T. Wang, "Receptor trafficking and synaptic plasticity," *Nature Reviews Neuroscience*, vol. 5, no. 12, pp. 952–962, 2004.

[79] G. Voglis and N. Tavernarakis, "The role of synaptic ion channels in synaptic plasticity," *EMBO reports*, vol. 7, no. 11, pp. 1104–1110, 2006.

[80] G. M. Shepherd, *The synaptic organization of the brain*. Oxford university press, 2004.

[81] F. Santamaria, S. Wils, E. De Schutter, and G. J. Augustine, "Anomalous diffusion in purkinje cell dendrites caused by spines," *Neuron*, vol. 52, no. 4, pp. 635–648, 2006.

[82] Z. Nusser, S. Cull-Candy, and M. Farrant, "Differences in synaptic gabaa receptor number underlie variation in gaba mini amplitude," *Neuron*, vol. 19, no. 3, pp. 697–709, 1997.

[83] D. C. Dieterich, J. J. Hodas, G. Gouzer, I. Y. Shadrin, J. T. Ngo, A. Triller, D. A. Tirrell, and E. M. Schuman, "In situ visualization and dynamics of newly synthesized proteins in rat hippocampal neurons," *Nature neuroscience*, vol. 13, no. 7, p. 897, 2010.

[84] M. Sheng, "The postsynaptic nmda-receptor—psd-95 signaling complex in excitatory synapses of the brain," *Journal of cell science*, vol. 114, no. 7, p. 1251, 2001.

[85] A. Motta, M. Berning, K. M. Boergens, B. Staffler, M. Beining, S. Loomba, P. Hennig, H. Wissler, and M. Helmstaedter, "Dense connectomic reconstruction in layer 4 of the somatosensory cortex," *Science*, vol. 366, no. 6469, 2019.

[86] J. W. Lichtman, H. Pfister, and N. Shavit, "The big data challenges of connectomics," *Nature neuroscience*, vol. 17, no. 11, pp. 1448–1454, 2014.

[87] W. A. Strauss, *Partial differential equations: An introduction*. John Wiley & Sons, 2007.

[88] G. Aakalu, W. B. Smith, N. Nguyen, C. Jiang, and E. M. Schuman, "Dynamic visualization of local protein synthesis in hippocampal neurons," *Neuron*, vol. 30, no. 2, pp. 489–502, 2001.

[89] G. Banker, K. Goslin, *et al.*, *Culturing nerve cells*. MIT press, 1998.

[90] S. A. Kim, H. Sanabria, M. A. Digman, E. Gratton, P. Schwille, W. R. Zipfel, and M. N. Waxham, "Quantifying translational mobility in neurons: comparison between current optical techniques," *Journal of Neuroscience*, vol. 30, no. 49, pp. 16409–16416, 2010.

[91] A. Einstein, " "U about the motion of particles suspended in liquids at rest, required by the molecular kinetic theory of heat," *annals of physics*, vol. 4, 1905.

[92] D. Alcor, G. Gouzer, and A. Triller, "Single-particle tracking methods for the study of membrane receptors dynamics," *European Journal of Neuroscience*, vol. 30, no. 6, pp. 987–997, 2009.

[93] D. Magde, E. Elson, and W. W. Webb, "Thermodynamic fluctuations in a reacting system—measurement by fluorescence correlation spectroscopy," *Physical review letters*, vol. 29, no. 11, p. 705, 1972.

[94] M. Ehrenberg and R. Rigler, "Rotational brownian motion and fluorescence intensify fluctuations," *Chemical Physics*, vol. 4, no. 3, pp. 390–401, 1974.

[95] M. Kang, C. A. Day, A. K. Kenworthy, and E. DiBenedetto, "Simplified equation to extract diffusion coefficients from confocal frap data," *Traffic*, vol. 13, no. 12, pp. 1589–1600, 2012.

[96] D. Axelrod, D. Koppel, J. Schlessinger, E. Elson, and W. W. Webb, "Mobility measurement by analysis of fluorescence photobleaching recovery kinetics," *Biophysical journal*, vol. 16, no. 9, pp. 1055–1069, 1976.

[97] R. D. Travasso, F. S. Dos Aidos, A. Bayani, P. Abranches, and A. Salvador, "Localized redox relays as a privileged mode of cytoplasmic hydrogen peroxide signaling," *Redox biology*, vol. 12, pp. 233–245, 2017.

[98] M. Marita, Y. Wang, M. J. Kaliszewski, K. C. Skinner, W. D. Comar, X. Shi, P. Dasari, X. Zhang, and A. W. Smith, "Class a plexins are organized as preformed inactive dimers on the cell surface," *Biophysical Journal*, vol. 109, no. 9, pp. 1937–1945, 2015.

[99] A. Sergé, L. Fourgeaud, A. Hémar, and D. Choquet, "Receptor activation and homer differentially control the lateral mobility of metabotropic glutamate receptor 5 in the neuronal membrane," *Journal of Neuroscience*, vol. 22, no. 10, pp. 3910–3920, 2002.

[100] H. E. Lu, H. D. MacGillavry, N. A. Frost, and T. A. Blanpied, "Multiple spatial and kinetic subpopulations of camkii in spines and dendrites as resolved by single-molecule tracking palm," *Journal of Neuroscience*, vol. 34, no. 22, pp. 7600–7610, 2014.

[101] O. D. Gil, T. Sakurai, A. E. Bradley, M. Y. Fink, M. R. Cassella, J. A. Kuo, and D. P. Felsenfeld, "Ankyrin binding mediates l1cam interactions with static components of the cytoskeleton and inhibits retrograde movement of l1cam on the cell surface," *The Journal of cell biology*, vol. 162, no. 4, pp. 719–730, 2003.

[102] K. Archibald, M. J. Perry, E. Molnár, and J. M. Henley, "Surface expression and metabolic half-life of ampa receptors in cultured rat cerebellar granule cells," *Neuropharmacology*, vol. 37, no. 10-11, pp. 1345–1353, 1998.

[103] L. Mikasova, P. De Rossi, D. Bouchet, F. Georges, V. Rogemond, A. Didelot, C. Meissirel, J. Honnorat, and L. Groc, "Disrupted surface cross-talk between nmda and ephrin-b2 receptors in anti-nmda encephalitis," *Brain*, vol. 135, no. 5, pp. 1606–1621, 2012.

[104] B. S. Colley, K. Biju, A. Visegrady, S. Campbell, and D. A. Fadool, "Neurotrophin b receptor kinase increases kv subfamily member 1.3 (kv1. 3) ion channel half-life and surface expression," *Neuroscience*, vol. 144, no. 2, pp. 531–546, 2007.

[105] J. K. Vasquez, K. Chantranuvatana, D. T. Giardina, M. D. Coffman, and J. D. Knight, "Lateral diffusion of proteins on supported lipid bilayers: Additive friction of synaptotagmin 7 c2a–c2b tandem domains," *Biochemistry*, vol. 53, no. 50, pp. 7904–7913, 2014.

[106] C. Neupert, R. Schneider, O. Klatt, C. Reissner, D. Repetto, B. Biermann, K. Niesmann, M. Missler, and M. Heine, "Regulated dynamic trafficking of neurexins inside and outside of synaptic terminals," *Journal of Neuroscience*, vol. 35, no. 40, pp. 13629–13647, 2015.

[107] R. Wenthold, H. Mahler, and W. Moore, "The half-life of acetylcholinesterase in mature rat brain," *Journal of neurochemistry*, vol. 22, no. 6, pp. 941–943, 1974.

[108] H. B. Peng, D.-Y. Zhao, M.-Z. Xie, Z. Shen, and K. Jacobson, "The role of lateral migration in the formation of acetylcholine receptor clusters induced by basic polypeptide-coated latex beads," *Developmental biology*, vol. 131, no. 1, pp. 197–206, 1989.

[109] M. Joensuu, P. Padmanabhan, N. Durisic, A. T. Bademosi, E. Cooper-Williams, I. C. Morrow, C. B. Harper, W. Jung, R. G. Parton, G. J. Goodhill, *et al.*, "Subdiffractional tracking of internalized molecules reveals heterogeneous motion states of synaptic vesicles," *Journal of Cell Biology*, vol. 215, no. 2, pp. 277–292, 2016.

[110] H. Schmidt, B. Schwaller, and J. Eilers, "Calbindin d28k targets myo-inositol monophosphatase in spines and dendrites of cerebellar purkinje neurons," *Proceedings of the National Academy of Sciences*, vol. 102, no. 16, pp. 5850–5855, 2005.

[111] A. Gauthier-Kemper, M. Igaev, F. Sündermann, D. Janning, J. Brühmann, K. Moschner, H.-J. Reyher, W. Junge, K. Glebov, J. Walter, *et al.*, "Interplay between phosphorylation and palmitoylation mediates plasma membrane targeting and sorting of gap43," *Molecular biology of the cell*, vol. 25, no. 21, pp. 3284–3299, 2014.

[112] S. Konzack, E. Thies, A. Marx, E.-M. Mandelkow, and E. Mandelkow, "Swimming against the tide: mobility of the microtubule-associated protein tau in neurons," *Journal of Neuroscience*, vol. 27, no. 37, pp. 9916–9927, 2007.

[113] L. W. Hayes and F. B. Jungalwala, "Synthesis and turnover of cerebrosides and phosphatidylserine of myelin and microsomal fractions of adult and developing rat brain," *Biochemical Journal*, vol. 160, no. 2, pp. 195–204, 1976.

[114] J. G. Kay, M. Koivusalo, X. Ma, T. Wohland, and S. Grinstein, "Phosphatidylserine dynamics in cellular membranes," *Molecular biology of the cell*, vol. 23, no. 11, pp. 2198–2212, 2012.

[115] E. Hannezo, B. Dong, P. Recho, J.-F. Joanny, and S. Hayashi, "Cortical instability drives periodic supracellular actin pattern formation in epithelial tubes," *Proceedings of the National Academy of Sciences*, vol. 112, no. 28, pp. 8620–8625, 2015.

[116] L. Truebestein, D. J. Elsner, E. Fuchs, and T. A. Leonard, "A molecular ruler regulates cytoskeletal remodelling by the rho kinases," *Nature communications*, vol. 6, no. 1, pp. 1–13, 2015.

[117] J. Muir and J. T. Kittler, "Plasticity of gabaa receptor diffusion dynamics at the axon initial segment," *Frontiers in cellular neuroscience*, vol. 8, p. 151, 2014.

[118] T. J. Hausrat, M. Muhia, K. Gerrow, P. Thomas, W. Hirdes, S. Tsukita, F. F. Heisler, L. Herich, S. Dubroqua, P. Breiden, *et al.*, "Radixin regulates synaptic gaba a receptor density and is essential for reversal learning and short-term memory," *Nature communications*, vol. 6, no. 1, pp. 1–17, 2015.

[119] T. Papouin, L. Ladépêche, J. Ruel, S. Sacchi, M. Labasque, M. Hanini, L. Groc, L. Pollegioni, J.-P. Mothet, and S. H. Oliet, "Synaptic and extrasynaptic nmda receptors are gated by different endogenous coagonists," *Cell*, vol. 150, no. 3, pp. 633–646, 2012.

[120] A. Qifti, L. Jackson, A. Singla, O. Garwain, and S. Scarlata, "Stimulation of gαq promotes stress granule formation," *BioRxiv*, p. 521369, 2019.

[121] I. Boksha, H.-J. Schönfeld, H. Langen, F. Müller, E. Tereshkina, and G. S. Burbaeva, "Glutamine synthetase isolated from human brain: octameric structure and homology of partial primary structure with human liver glutamine synthetase," *Biochemistry (Moscow)*, vol. 67, no. 9, pp. 1012–1020, 2002.

[122] A.-h. Song, D. Wang, G. Chen, Y. Li, J. Luo, S. Duan, and M.-m. Poo, "A selective filter for cytoplasmic transport at the axon initial segment," *Cell*, vol. 136, no. 6, pp. 1148–1160, 2009.

Curriculum Vitae

Personal information

Name:	Fabio Sartori
Date of birth:	02 September 1988
Place of birth:	Parma, Italy
Citizenship:	Italian
E-mail:	sartori.fabio88@gmail.com

Education

2002-2007	Classical Studies, at G.D. Romagnosi, Parma, Italy
2008-2012	Bachelor in Physics, Università degli Studi di Parma, Parma, Italy (106/110).
2012-2014	Master in Physics, Università degli Studi di Parma, (108/110), Frankfurt, Germany.
2015-today	Doctoral studies, Max Planck Institute for Brain Research, Frankfurt, Germany.
2015-today	International Max Planck Research School for Neural Circuits, Max Planck Institute for Brain Research, Frankfurt, Germany.

Scientific contributions

List of Publications

- **Sartori F**, Hafner AS, Karimi A, Nold A, Fonkeu Y, Schuman EM, Tchumatchenko T. Statistical Laws of Protein Motion in Neuronal Dendritic Trees. Cell reports. 2020 Nov 17; 33(7): 108391.

- Fonkeu Y, Kraynyukova N, Hafner AS, Kochen L, **Sartori F**, Schuman EM, Tchumatchenko T. How mRNA localization and protein synthesis sites influence dendritic protein distribution and dynamics. Neuron. 2019 Sep 25; 103(6): 1109-22.

- Weigand M, **Sartori F**, Cuntz H. Universal transition from unstructured to structured neural maps. Proceedings of the National Academy of Sciences. 2017 May 16; 114(20): E4057-64.

- Agliari E, Cassi D, Cattivelli L, **Sartori F**. Two-particle problem in comblike structures. Physical Review E. 2016 May 5; 93(5): 052111.

- Cattivelli, L., Agliari, E., **Sartori, F.**, Cassi, D. (2015). Lévy flights with power-law absorption. Physical Review E, 92(4), 042156.

- Agliari, E., **Sartori, F.**, Cattivelli, L., Cassi, D. Hitting and trapping times on branched structures. Physical Review E, 91(5), 052132, 2015

- Bonfà, P., **F. Sartori**, and R. De Renzi. Efficient and reliable strategy for identifying muon sites based on the double adiabatic approximation. The Journal of Physical Chemistry C 119.8 (2015): 4278-4285.

List of Talks

- **The Impact of neuronal morphology on protein distribution in neuronal processes**, 2018 Bordeaux

- **The Journey of a Protein, Neuroscience meets datascience**, 2020, Frankfurt

- **Statistical laws of protein motion in neuronal processes**, Neuromatch 2.0, 2020, Online

List of Poster

- **Random Walks on Combs: Covering and Hitting Times**, XIX National Conference on Statistical Physics and Complex System 2014, Parma

- **Separating Spike Trains Using Information Theory**, Bernstain Conference 2016, Berlin

- **The Impact of neuronal morphology on protein distribution in neuronal processes**, Dendrites 2018 , Heraklion

- **The Impact of neuronal morphology on protein distribution in neuronal processes**, Bernstein 2018 , Berlin

Conferences and Schools

- XIX National Conference on Statistical Physics and Complex System, Parma

- XX National Conference on Statistical Physics and Complex System, Parma

- ESISync 2016, Frankfurt

- ESISync 2017, Frankfurt

- Dendrites2018, Heraklion

- Bernstein Conference 2016, Berlin

- Bernstein Conference 2017, Berlin

- Bernstein Conference 2018, Berlin

- Bernstein Conference 2019, Berlin

- Neuromatch 2.0, online

Teaching and Organization

- 2012-2013 Tutor at the department of Physics, Parma

- Lecture: **Physic in Modern Cuisine: the Soft Matter**, Formia 2014,

- Lectures: **Science in the kitchen, the adventure of molecular gastronomy** 2, and 23 march 2015,

- 2017-2021: member of the CRC1080 committee,

- Bernstein Conference 2021: Workshop **The inner life of dendrites- mechanisms behind synaptic input integration**